Scuola Normale Superiore

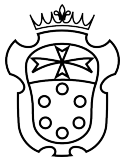

Ph.D. Thesis

Engineered environments for biomedical applications: anisotropic nanotopographies and microfluidic devices

Sandro Meucci

Advisor
Marco Cecchini

2014

Cover: M.C. Escher,
Drawing hands (1948, Lithography)

Chapter figures: M.C. Escher,
Metamorphosis II (1940, Woodcut)
Metamorphosis I (1937, Woodcut)

My work is a game,
a very serious game.

— M. C. Escher

Dedicated to my family,
because any path is safer
if your initial steps are firm.

ABSTRACT

During the last two decades micro- and nano-fabrication techniques originally developed for electronic engineering have directed their attention towards life sciences. The increase of analytical power of diagnostic devices and the creation of more biomimetic scaffolds have been strongly desired by these fields, in order to have a better insight into the complexity of physiological systems, while improving the ability to model them *in vitro*. Technological innovations worked to fill such a gap, but the integration of these fields of science is not progressing fast enough to satisfy the expectations. In this thesis I present novel devices which exploit the unique features of the micro- and nanoscale and, at the same time, match the requirements for successful application in biomedical research. Such biochips were used for optical detection of water-dispersed nanoparticles in microchannels, for highly controlled cell-patterning in closed microreactors, and for topography-mediated regulation of cell morphology and migration. Moreover, pilot experiments on the pre-clinical translation of micropatterned scaffolds in a rat model of peripheral nerve transaction were initiated and are ongoing. Given these results, the devices presented here have the potential to achieve clinical translation in a short/medium time, contributing to the improvement of biomedical technologies.

CONTENTS

1 INTRODUCTION 1
- 1.1 Microfluidic devices 2
- 1.2 Mechanotransduction and nanotopography 3

2 MICROFLUIDIC DEVICES FOR BIOLOGICAL APPLICATIONS 7
- 2.1 Introduction to microfluidics 7
  - 2.1.1 Governing equations in microfluidics 7
  - 2.1.2 Poiseuille flow and hydraulic resistance 9
  - 2.1.3 Diffusion at the microscale 11
- 2.2 Lab-on-a-Chip & Chip-in-a-Lab 13
  - 2.2.1 High-throughput biochemical analysis 13
  - 2.2.2 Synthesis of nanomaterials for tissue engineering 14
  - 2.2.3 Microfluidics and cell-biology 15
- 2.3 Optofluidic devices 16
  - 2.3.1 Terahetz probe of objects in water environment 17
  - 2.3.2 Water-dispersible LC-nanoresonators 24
  - 2.3.3 Microstructured phantoms for photoacuostic imaging 28
- 2.4 Tailoring co-cultures in closed microchamber 31
  - 2.4.1 Chip Architecture 32
  - 2.4.2 Fluid dynamics 33
  - 2.4.3 Automated cell-loading 37
  - 2.4.4 Tailoring co-cultures by serial asymmetric loading 40
  - 2.4.5 Continuous perfusion in chemically-anisotropic environment 41
  - 2.4.6 Conclusions 44

3 BREAKING TOPOGRAPHICAL ISOTROPY 45
- 3.1 Introduction to mechanotransduction 45
  - 3.1.1 Biological actors in mechanotransduction 45
  - 3.1.2 Structural anisotropy in bio-matrices 47
  - 3.1.3 Artificial extracellular matrices: a state-of-art 48
- 3.2 Nanogratings: design & fabrication 51
- 3.3 Cell shaping and polarization 55
  - 3.3.1 Nanostructured materials in orthopedics 55
  - 3.3.2 Mesenchimal stromal cell interaction with PET gratings 56
  - 3.3.3 Cell morphology analysis 57
  - 3.3.4 Conclusions 60
- 3.4 Surface topography and focal adhesion-molecular turnover 60

3.4.1 Endothelium and cell polarization 60
3.4.2 Contact guidance on single endothelial cells 61
3.4.3 Polarization of endothelial cell monolayers 62
3.4.4 Focal adhesion stability in migrating cells 63
3.4.5 Conclusion 65
4 DIRECTIONALITY MODULATION BY TOPOGRAPHICAL NOISE 67
4.1 Introduction 67
4.2 Noisy nanogratings: design and fabrication 68
4.2.1 Design 68
4.2.2 Substrate directionality quantification 70
4.2.3 Fabrication 73
4.2.4 Conclusions 73
4.3 Neuronal pathfinding on noisy nanostructures 74
4.3.1 Cell viability 74
4.3.2 Neurite alignment 75
4.3.3 Focal adhesions and nano-modifications 76
4.3.4 Pharmacological tuning of contact guidance 78
4.3.5 Conclusions 81
4.4 Stem cell mechanotrasduction on noisy nanotopographies 82
4.4.1 Cell viability 83
4.4.2 Single cell morphological analysis 83
4.4.3 Focal adhesion morphology 85
4.4.4 Single cell migration 88
4.4.5 Dependence on δ 90
4.4.6 Conclusions 90
5 TOWARDS PRE-CLINICAL TRANSLATION 93
5.1 Introduction 93
5.2 Schwann cell directional migration along PDMS micrograting 95
5.2.1 PDMS-membrane fabrication 95
5.2.2 In vitro Schwann cell migration 96
5.3 In vivo experiments and biodegradable films 99
5.3.1 Implantable PDMS membranes 99
5.3.2 Biodegradable, micropatterned scaffolds 101
5.4 Conclusions 102
6 CONCLUSIONS 103
A FABRICATION PROTOCOLS 105
A.1 Microfluidic devices 105
A.2 Molds for PDMS soft lithography 106
A.3 Gold nanorods fabrication 109

A.4 Molds for hot embossing 109
A.5 Hot embossing 111
A.6 PDMS scaffold fabrication 111
B PROTOCOLS AND METHODS 113
B.1 Terahertz setup 113
B.2 STICS measurements 113
B.3 Shear-stress calculation in MC 114
B.4 Directionality calculation 115
B.5 Microchamber filling and automated cell loading 115
B.6 Cell culturing protocols 116
B.7 Cell viability assessment 120
B.8 EGFP-paxillin transfection 120
B.9 Microscopy 120
B.10 Morphometrical analysis 122
B.11 Focal adhesion analysis 123
B.12 Migration analysis 124
LIST OF PUBLICATIONS 125
ACKNOWLEDGEMENTS 127
BIBLIOGRAPHY 128
INDEX 149

LIST OF FIGURES

Figure 2.1 Velocity distribution in Poiseuille flow 9
Figure 2.2 Microfluidic-plasmonic probe 17
Figure 2.3 Architecture of the microfluidic chip 19
Figure 2.4 Detection of subwavelength particles 20
Figure 2.5 Simultaneous detection of particles with different diameter 22
Figure 2.6 Design of the LC-nanoresonators 25
Figure 2.7 Microfluidic device for detection of LC-nanoresonators 26
Figure 2.8 On-chip optical detection of LC-nanoresonators 27
Figure 2.9 Gold nanorods in photoacoustic imaging 28
Figure 2.10 PDMS microfluidic phantom 30
Figure 2.11 Microfluidic chip architecture 32
Figure 2.12 Chip fluid-dynamics characterization 35
Figure 2.13 Speed measurement in active-pressurization-mode 36
Figure 2.14 Automated cell-loading in closed microchamber 38
Figure 2.15 HeLa cells growth-curve during standard perfusion 39
Figure 2.16 Asymmetric cell loading and co-culture 40
Figure 2.17 CT–Dex-induced cell-death 43
Figure 3.1 Structure and functional scheme of a focal adhesion 46
Figure 3.2 Topography dimensionality 49
Figure 3.3 Structure of a nanograting 50
Figure 3.4 Thermal nanoimprinting 53
Figure 3.5 Mold fabrication protocols 54
Figure 3.6 SEM imaging of silicon molds 55
Figure 3.7 PET-NGs and hMSC morphological parameters 57
Figure 3.8 hMSC morphology on NGs 58
Figure 3.9 Chytoskeletal organization of hMSC on NGs 59
Figure 3.10 Nuclear morphology on NGs 60
Figure 3.11 hUVEC morphology on patterned surfaces 61
Figure 3.12 Cytoskeletal organization of hUVEC monolayers 63
Figure 3.13 Focal adhesion dynamics on migrating hUVECs 64
Figure 3.14 Focal adhesion life time 65
Figure 4.1 Nanomodifications on nanogratings 69
Figure 4.2 Directionality quantification 71
Figure 4.3 Quantification of substrate directionality 72

Figure 4.4 Set of noisy nanogratings 73
Figure 4.5 PC12 neurite alignment 76
Figure 4.6 Focal adhesion alignment on noisy nanogratings 77
Figure 4.7 Focal adhesion maturation on noisy nanogratings 79
Figure 4.8 Pharmacological modulation of noise tolerance 80
Figure 4.9 Focal adhesion development in presence of nocodazole 81
Figure 4.10 WJ-hMSC morphology 84
Figure 4.11 Actin cytoskeleton polarization 85
Figure 4.12 Focal adhesion morphology 86
Figure 4.13 Focal adhesion alignment to nanogratings 87
Figure 4.14 Analysis of cell migration 89
Figure 5.1 Microgratings on PDMS membranes 96
Figure 5.2 SC migration on microgratings 98
Figure 5.3 Nerve regeneration *in vivo* 100
Figure 5.4 Nanogratings on PCL/PLA membranes 101

LIST OF TABLES

Table 2.1 Mechanical properties of soft tissues 29
Table 2.2 Channel geometrical characteristics and hydraulic resistance 33
Table 2.3 Standard operating modes 34
Table 3.1 Nanogratings with constant depth 51
Table 3.2 Nanogratings with constant aspect-ratio 52
Table 4.1 Focal adhesion size 78
Table 5.1 Microratings for nerve conduits 95
Table 5.2 PCL/PLA microgratings 102

ACRONYMS

AR Aspect Ratio

AT Appearance Time

2D 2-Dimensional

CA Contrast Agent

CT Catechin

DEX Dextran

DI-H_2O De Ionized water

DMEM Dulbecco's Modified Eagle's Medium

DMSO Di Methyl Sulf Oxide

DNA Deoxyribo Nucleic Acid

DPCR digital Polymerase Chain Reaction

EBL Electron Beam Lithography

ECM Extra Cellular Matrix

EGFP Enhanced Green Fluorescent Protein

FA Focal Adhesion

FBS Fetal Bovine Serum

FDA Food and Drug Administration

FFT Fast Fourier Transform

FT Fourier Transform

FTIR Fourier Trasform Infra Red (spectrometer)

FWHM Full Width Half Maximum

GEF Guanine-nucleotide Exchange Factor

GFP Green Fluorescent Protein

HS Horse Serum

ICP Inductively Coupled Plasma

IR Infra Red

LOC Lab-on-a-Chip

LR Liquid Reservoir

LT Life Time

MC Micro Chamber

NA Numerical Aperture

NG Nano Grating

NGF Nerve Growth Factor

NM$^-$ Nano Modification (Negative)

PAI Photo Acoustic Imaging

PBS Phosphate Buffered Saline

PC Perfusion Channel

PI Propidium Iodide

NM$^+$ Nano Modification (Positive)

POCT Point of Care Testing

PSF Point Spread Function

QCL Quantum Cascade Laser

RIE Reactive Ion Etching

SCCM Standard Cubic Centi Meter

STICS Spatio-Temporal Image Correlation Spectroscopy

STP Standard Temperature and Pressure

THZ Tera Hertz

TIRF Total Internal Reflection Fluorescence

3D 3-Dimensional

UV Ultra Violet

WLC Waste/Loading Channel

MATERIALS

APTES (3-Amino Propyl)Triethoxy Silane

COC Cyclic Olefin Copolymer

PCL Poly (CaproLactone)

PDMS Poly (Dimethyl Siloxane)

PEG Poly (Ethylene Glicol)

PET Poly (Ethylene Terephtalate)

PLA Poly (Lactic Acid)

PMMA Poly (Methil Methacrylate)

PS Poly (Styrene)

TCPS Tissue Culture Poly (Styrene)

CELL-TYPES

EC Endothelial Cell

HMSC Human Mesenchimal Stromal Cell

HUVEC Human Umbilical-Vein Endothelial Cell

IPSC Induced Pluripotent Stem Cell

PC12 rat Pheochromocytoma Cell line

REF Rat Embryonic Fibroblasts

SC Schwann Cell

WJ-HMSC Wharton's Jelly human Mesenchymal Stem Cells

1 INTRODUCTION

Medicine and life sciences are nowadays deeply linked to technology. Indeed, both the abilities of analysing and interacting with biological systems relies on the capability to observe, describe and manipulate them. In the last two decades microscopy has extended our perception so much that now not only single cell, but also single molecule imaging is possible. Moreover, the realization of devices able to work synergically with living organisms looks closer to our reach day after day, owing to the translation of micro- and nanofabrication techniques to life sciences. With this chapter I introduce the role of two technologies that have had an important role in biological research during the last ten years and that show the potential to be complementary approaches to move towards a new generation of artificial devices: microfluidics *and* surface nanostructuring.

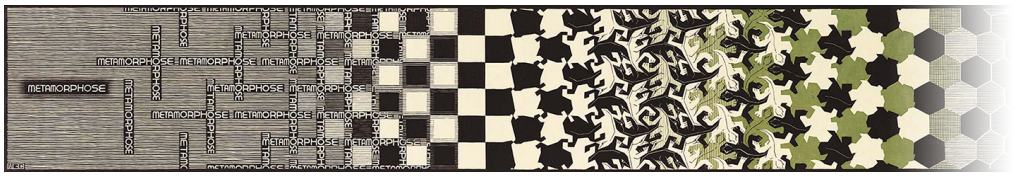

Living organisms have complex and dynamic structures. The tissues that form their bodies are composed of a three-dimensional (3D) matrix in which cells are able to migrate, guided by chemical and mechanical cues[1]. Liquids flow in intricate networks of vessels regulating nutrient supply, waste product wash-out, and endocrine signalling, allowing for the homeostasis of the whole system. Investigating this complex entity without impairing its integrity is not trivial, and finding the anomalies that cause pathologies can be like looking for a needle in a haystack.

A way to overcome this issue is to develop models, where specific aspects of complex systems are recreated to be studied. This approach relies on the trade-off between reducing the original complexity and not altering the features that must be observed. For this reason, a great interest arises from technological advances, which are asked to improve our ability to *detect* small variations in the tissues, *reproduce* traits of the physiological microstructures *in vitro*, and *translate* them to devices that can be implanted in living organisms.

1.1 MICROFLUIDIC DEVICES

Microfluidics, a field of science born in the 1980s by the converging needs of different disciplines, is a good candidate for recreating *in vitro* the chemical and physical complexity of *in vivo* environments[2]. The miniaturization of the fluidic elements, initially made by using capillaries and later micron-sized channels, seemed to meet all the mentioned requirements. Indeed, analytical chemistry exploited the physical confinement of analytes to yield a better definition of the investigation area compared with traditional, bulky systems, obtaining improvement not only in sensitivity, but also in the control over chemical reactions[3]. The possibility to increase the density of fluidic elements, performing several analyses in parallel on the same device, was greatly appreciated also in molecular biology, where new applications like high-throughput analysis were beginning to emerge[3]. Lastly, scaling down laboratory equipment and integrating it on a single portable device was of great interest for healthcare—biodefence first and point-of-care testing (PoCT) later.

The widespread use of microfluidics in research laboratories arrived at the end of the 1990s owing largely to the use of poly (dimethylsiloxane) (PDMS)[4], an optically transparent, soft elastomer that made the design and fabrication of microdevices much easier than the previous standards—i. e. glass or poly (methyl methacrylate) (PMMA). PDMS could be used in combination with fabrication techniques widely used in microelectronic engineering and it could be easily sealed to glass making it compatible with standard microscopy techniques. Moreover the elastomeric nature of PDMS was exploited to integrate monolithic soft valves[5] in the devices, allowing the routing of liquids in intricate, reconfigurable networks of channels[6]. Microfluidic devices are highly qualified for the dynamic control of chemical gradients[2] owing to the predictable fluid dynamics characteristic of the microscale—i. e. laminar flow. Moreover, the use of fluidic elements with sizes comparable with those of cells allows for applications such as single-cell isolation, proliferation[7], gene amplification and analysis[8].

Despite its proven qualities, microfluidics has not yet satisfied the initial expectations, and its widespread use in medicine is still yet to come. In a recent review[9] Sackmann et al. analyzed this phenomenon, suggesting that one of the reasons may be found in the lack of integration between the designers (physicists and engineers) and the final users (biologists and clinicians). A clear example can be found in the evolution of the devices for visual chemotaxis assays—the study of cell migration in chemical gradients. Owing to the precise control over chemical concentration offered by the laminar flow[10], chemotaxis assays seemed to be the killer application for bio-oriented microfluidics. However, the new technology is usually constrained to close proximity of ancillary equipment specific to physics laboratories, i. e. pumping

systems and control units, which are difficult to integrate with the consolidated experience of biological protocols. This characteristic made it difficult for microfluidic devices to impose over the traditional assays represented by the Boyden chamber (developed in 1962) and its evolutions—i. e. the Zigmond, Dunn and Insall chambers[11]. These devices rely on the gradient formed by pure diffusion in a porous membrane or narrow channels dividing reservoirs loaded with media at different chemoattractant concentration. The ease of use and the compatibility with the standard equipment found in a biological laboratory is such that traditional chemotaxis assays are still preferred over their commercial microfluidic counterparts.

These topics will be examined in CHAPTER 2. I will introduce the governing equations of microfluidics and then report my results in the designing and testing microfluidic chips. First I will present devices for *optofluidics*—i. e. the use of microenvironments to perform optical measurements on a few picoliters of liquids—investigating the detection limits of water-dispersed nanoparticles designed for biological uses. Then, I will introduce a device designed to exploit the peculiarities of flow dynamics at the microscale—i. e. continuous perfusion, stable chemical gradient formation—without the need for external pumping systems or fixed tubings.

1.2 MECHANOTRANSDUCTION AND NANOTOPOGRAPHY

While microfluidics can create chemical gradients and flow-generated shear stress similar to those found in biological environments, alternative techniques are needed to mimic the mechanical stimuli provided by physiological matrices. It is known that cells can read mechanical information in the environment by using specific molecular complexes present on their membranes[12,13]. These complexes—FAs—are composed of several subunits growing in a highly dynamic way, gathering the adhesion proteins, linking them to the contractile elements of the cytoskeleton, and providing feedback on the traction experienced by the adhesion plaque. Through this signalling, FAs are able to influence the regulation of essentially every aspect of the cytoskeleton—e. g. the GTPases Rho and Rac—and have a large impact on cell morphology and motility. This signal transduction mechanism, which involves mechanical sensing, cell contractility and structural organization is known as *mechanotransduction*.

Even though the above described mechanism is widely accepted, the complete list of molecular actors involved in it is still not completely known. Ingber developed an elegant model of cellular tensegrity[14,15] suggesting that the final target in this traction chain may not be the cytoskeleton but the nucleus itself. For example, a network of intermediate filaments[16] closely associated with interphase chromosomes place

it in a central position of this wide structure, like a spider at the center of its web[17]. This direct line connecting the extracellular matrix to the chromosomes might be the key to explaining a kind of signal transduction parallel to the traditional one, which links the intracellular mechanical equilibrium to the one of the environment.

Predicting the behaviour of cells growing on substrates with different mechanical properties is extremely important for a plethora of applications in tissue engineering. Indeed, when designing a scaffold it is useful to know how strong cell-adhesion will be, if migration will be random or directional, and even if differentiation will direct to a specific lineage. This information could allow guided and enhanced regeneration after an injury. Some approaches to achieve these results using micro- and nanostructured substrates will be introduced in the first part of CHAPTER 3, then I will focus on the results I obtained using a directional topography named nanograting (NG). Structures of this kind, composed by parallel lines with width varying from 500 nm to 2 μm, were realized on biocompatible thermoplastic materials—i. e. cyclic olefin copolymer (COC) and poly (ethylene terephthalate) (PET)—and used to induce cell-body elongation, cytoskeleton polarization and directional migration for different cell-types.

Once the efficacy of this devices is proven, I will discuss a novel method to modulate the directional signal by adding *nanotopographical noise* to the NGs. This geometrical alteration mimics the progressive deposition of matrix and biological debris on it, masking the nanostructure. This phenomenon will also be more severe if the scaffolds are biodegradable. This study, describing the cellular capability to read partially-hidden topographies, is a step towards a better understanding of the performances of nanostructured scaffolds after *in vivo* implantation. In CHAPTER 4 I will describe these new structures, propose a Fourier transform-based algorithm to quantitatively define the directional stimulus and discuss the effect of substrate-directionality reduction first on FA-organization and migration patterns in human mesenchimal stromal cells (hMSCs) and second on neurite pathfinding using the PC12 cell-line. In this last case, the ability of neurites—projections extending from the soma of neuronal cells—to read hidden directional stimula and align to it was investigated in the presence of drugs that affect cell-contractility.

Finally, in CHAPTER 5 I will show my efforts in translating the above described devices *in vivo*, for the improvement of healing after peripheral nerve injury. The gold standard for this procedure consists in the autologous transplantation, i. e. a nerve is removed from the patient and used to stitch the stumps of the severed nerve. This approach has obvious drawbacks, since a healthy part of the body is sacrificed. Artificial alternatives are also known[18] and usually concentrate on replacing the autologous material with biocompatible polymers. This procedure only relies on the physical confinement of the regrowing ends of a severed nerve. Here, I propose an approach that exploits the proven abilities of micro- and nanogratings to

polarize cell-migration and axon guidance to guide the regeneration in the direction of the nerve. Migration of primary Schwann cells (SCs) on PDMS membranes was studied *in vitro* and preliminary studies of *in vivo* translation for sciatic nerve regeneration were conduced. Finally, I will show preliminary data on the nanopatterning of poly (caprolactone)/poly (lactic acid) (PCL/PLA), a biocompatible and biodrgradable polymer blend used for tissue-engineering applications.

Chapter 6 contains my conclusions. Here, I will summarize the results obtained in this thesis and discuss possible future developments.

2 MICROFLUIDIC DEVICES FOR BIOLOGICAL APPLICATIONS

Microfluidics is a technology specialized in handling small amounts of liquids in extremely controlled environments. The increasing request of large scale integration made by industry and the interest of biomedical research in developing devices that can handle biology in artificial environment, gave a strong burst to this field. In this chapter I will introduce the governing equations of fluid dynamics in the microfluidic regime, review the evolution of microfluidics for life sciences and present my results in this field. First, I will concentrate on optofluidics, *introducing three devices designed to allow physical measurements—i.e. optical detection of contrast agents—in microstructured environments. Then I will present a biochip for culturing cells in a closed microchamber, yielding automatic cell loading, long term perfusion and dynamic control over chemical gradients while maintaining full compatibility with the standard equipment and skills that are found in standard tissue culture facilities.*

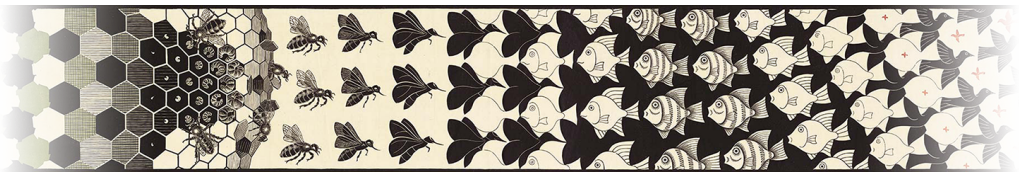

2.1 INTRODUCTION

2.1.1 Governing equations in microfluidics

As previously stated, one of the advantages of microfluidics compared with macro-scaled systems, is the exquisite control over fluid dynamics. This can be explained by analyzing the equation that rules hydrodynamics—known as the Navier-Stokes equation—and considering the simplifications that can be done by taking into account the size of the fluidic elements and the liquid speeds typically found in microfluidics.

The general form of the Navier-Stokes equation is derived from the continuity equations of mass and momentum[10]. The velocity distribution $\boldsymbol{v}(\boldsymbol{r}, t)$—in the following presented as $\boldsymbol{v}$—can be calculated under the hypothesis of incompressible Newtonian fluid, acceptable for the water-like fluids and low velocity fields used

in microfluidics. This means that the density ρ and the dynamic viscosity η can be considered as constants, leading to the expression

$$\rho\left[\partial_t \boldsymbol{v} + \left(\boldsymbol{v}\cdot\boldsymbol{\nabla}\right)\boldsymbol{v}\right] = -\boldsymbol{\nabla} p + \eta\nabla^2\boldsymbol{v}. \tag{2.1}$$

The left-hand side of equation contains the inertial terms while the right-hand side contains the forces acting on the fluid, i. e. the pressure p and the viscous friction. The number of solutions allowed by EQUATION (2.1) is incredibly great owing to the mathematical richness generated by the non-linear term $\rho\left(\boldsymbol{v}\cdot\boldsymbol{\nabla}\right)\boldsymbol{v}$. Unfortunately this also makes the analytical treatment so difficult and complex that the solutions of the equation have never been fully characterized. A convenient way to proceed is by changing to dimensionless coordinates. This can be done expressing the physical variables in units of the characteristic scales (e. g. $\boldsymbol{r} = L_0\tilde{\boldsymbol{r}}$ and $\boldsymbol{v} = V_0\tilde{\boldsymbol{v}}$) for length and velocity, respectively, and defining a dimensionless number called the Reynolds number

$$Re \equiv \frac{\rho V_0 L_0}{\eta}. \tag{2.2}$$

The pivotal role of Re is evident after the substitution. Indeed, EQUATION (2.1) becomes

$$Re\left[\partial_{\tilde{t}}\tilde{\boldsymbol{v}} + \left(\tilde{\boldsymbol{v}}\cdot\tilde{\boldsymbol{\nabla}}\right)\tilde{\boldsymbol{v}}\right] = -\tilde{\boldsymbol{\nabla}}\tilde{p} + \tilde{\nabla}^2\tilde{\boldsymbol{v}} \tag{2.3}$$

showing that the Reynolds number represents the weight of the inertial term in determining the velocity field. When the Reynolds number is lower than a critical value ($Re_{cr} \approx 2\cdot 10^3$ [19]) fluid flows in parallel layers—or streamlines. Perturbations in the regular flow can only be transient and do not alter the global regularity of the flow. This fluidic regime is called *laminar flow* and can be exploited to achieve a reliable control over the dynamics of small particles dispersed in the liquid (e. g. suspended cells or fluorescent markers) and carried by the viscous drag.

When $Re \ll 1$ the inertial term can be neglected and EQUATION (2.3) can be simplified to the linear equation

$$0 = -\tilde{\boldsymbol{\nabla}}\tilde{p} + \tilde{\nabla}^2\tilde{\boldsymbol{v}}. \tag{2.4}$$

This approximation is highly relevant in microfluidic systems, where the small channel sizes and the moderate liquid speeds makes the viscous forces dominant. This regime is called Stokes flow, or creeping flow, and allows for analytic solutions to a number of flow problems usually found when dealing with pressure-driven flows in microfluidic devices.

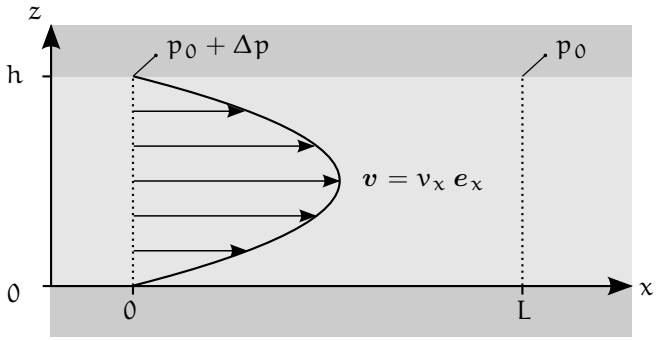

Figure 2.1: Velocity distribution in Poiseuille flow. The scheme refers to a xz section of a channel extending indefinitely in the y direction.

2.1.2 Poiseuille flow and hydraulic resistance

An important case in which the Stokes equation allows for an analytic solution is represented by the Poiseuille flow. If we consider a liquid at the steady state, flowing inside a channel extending indefinitely in the x direction, symmetry imposes that the only non-zero component of the velocity vector is x and it does not depend on x, so $\boldsymbol{v}(\boldsymbol{r}) = v_x(y,z)e_x$. Since the $v_{y,z} = 0$, it follows that $\partial_{y,z}p = 0$, and consequently that the pressure field only depends on x, so $p(\boldsymbol{r}) = p(x)$. Now, substituting in EQUATION (2.4) we have

$$\eta\left[\partial_y^2 + \partial_z^2\right]v_x = \partial_x p, \tag{2.5}$$

since the two sides of the equation are functions of different variables, the only possible solution is that both sides are equal to the same constant, so pressure must vary linearly in x.

$$\left[\partial_y^2 + \partial_z^2\right]v_x = -\frac{\Delta p}{\eta L}. \tag{2.6}$$

An analytic solution can be found for infinitely wide channels, where the velocity field can be considered as constant in the y direction, so $v_x(y,z) = v_x(z)$. In this case, EQUATION (2.6) becomes

$$\partial_z^2 v_x = -\frac{\Delta p}{\eta L}, \tag{2.7}$$

where Δp is the pressure difference between points placed at L distance in x. As a boundary condition we assume that no relative motion can happen between the liquid and the walls (no slip condition) and the solution of EQUATION (2.7) result in a parabolic profile

$$v_x = \frac{\Delta p}{2\eta L}(h - z)z. \tag{2.8}$$

The symmetry of the velocity field also allows for a simple calculation of the shear stress exerted on the walls of the channel. Indeed, the stress tensor σ for incompressible fluids is

$$\sigma_{ij} = \eta\Big(\partial_j v_i + \partial_i v_j\Big), \tag{2.9}$$

and, for the laminar regime expressed by EQUATION (2.8), can be simplified to obtain

$$\sigma_{xz} = \eta\partial_z \tilde{v}_x = \frac{\Delta p}{\eta L}\Big(\frac{h}{2} - z\Big). \tag{2.10}$$

Hydraulic resistance

The fabrication processes used to produce microfluidic devices (i. e. UV lithography and soft lithography) usually produce rectangular cross-section channels. Unfortunately, no analytical solution exists for such a geometry. As a first approximation, EQUATION (2.8) can be used to model a rectangular microchannel with a small aspect ratio. The approximated flow rate Q can be found by integration over channel cross-section

$$Q = \int_0^w dy \int_0^h dz\, \frac{\Delta p}{2\eta L}(h - z)z = \frac{h^3 w}{12\eta L}\Delta p, \tag{2.11}$$

but the error committed is quite high[10] (7% for an aspect ratio of one tenth, $h = w/10$). A better approximation of Q can be obtained from EQUATION (2.6) by expanding the velocity field as a Fourier series along the short vertical z direction,

$$v_x = \frac{4h^2\Delta p}{\pi^3\eta L}\sum_{n,\text{odd}}^{\infty}\frac{1}{n^3}\left[1 - \frac{\cosh\big(n\pi\frac{y}{h}\big)}{\cosh\big(n\pi\frac{y}{2h}\big)}\right]\sin\Big(n\pi\frac{z}{h}\Big), \tag{2.12}$$

resulting in

$$Q = \frac{h^3 w \Delta p}{12\eta L}\left[1 - \sum_{n,\text{odd}}^{\infty} \frac{1}{n^5}\frac{192}{\pi^5}\frac{h}{w}\tanh\left(n\pi\frac{w}{2h}\right)\right]. \tag{2.13}$$

EQUATION (2.13) can be conveniently approximated in case of very wide channels, since when $h/w \to 0$, $\frac{h}{w}\tanh(n\pi\frac{w}{2h}) \to \frac{h}{w}\tanh(\infty) = \frac{h}{w}$, and Q becomes

$$Q \approx \frac{h^3 w}{12\eta L}\left[1 - 0.630\frac{h}{w}\right]\Delta p. \tag{2.14}$$

This approximation is surprisingly good. For the worst case of a squared channel ($h = w$), the error is just 13% and for an aspect ratio of a half ($h = w/2$) the error is already down to 0.2%[10]. Finally, using EQUATION (2.14) it is easy to calculate the hydraulic resistance R_{hyd} for the Poiseuille flow in rectangular microchannels,

$$R_{hyd} \equiv \frac{\Delta p}{Q} = \frac{12\eta L}{1 - 0.63(h/w)}\frac{1}{h^3 w}. \tag{2.15}$$

2.1.3 Diffusion at the microscale

Diffusion is the process that leads to the flow of a substance in a solvent, caused by a spatial difference in concentration. Diffusion is a well-known method used in many physical and chemical applications, e. g. the enhancement of steel hardness by diffusing carbon in it or the separation of solutes with different diffusion times. Moreover, diffusion is responsible for a plethora of key processes in biology, since chemical gradients are one of the main mechanisms used by cells to communicate[1,20]. Through the combination of the highly predictable fluid dynamics of laminar flow to diffusion, microfluidics represents a powerful tool to control chemical gradients.

The interplay between diffusion and convection of an incompressible fluid can be described by the mass conservation equation. The concentration $c(\boldsymbol{r}, t)$ of a given specie will be

$$\partial_t c + \boldsymbol{\nabla}\cdot\boldsymbol{J} = 0, \tag{2.16}$$

and $\boldsymbol{J}$ is the current density of a given solute. $\boldsymbol{J}$ must be written in terms of a convection current density $\boldsymbol{J}^{\text{conv}}$, due to the global velocity field $\boldsymbol{v}$ of the solution, and a diffusion current density $\boldsymbol{J}^{\text{diff}}$, due to the random motion of the solute relative to the solution. The first can be written as $\boldsymbol{J}^{\text{conv}} = c\,\boldsymbol{v}$, while the second is

defined by the first Fick's law $\boldsymbol{J}^{\text{diff}} = -D\,\boldsymbol{\nabla} c$. Substituting the total current density in EQUATION (2.16) we have the so called convection-diffusion equation

$$\partial_t c + \boldsymbol{v}\cdot\boldsymbol{\nabla} c = D\,\nabla^2 c. \tag{2.17}$$

Notice that the left-hand side of this equation holds the convective term and the right-hand side describes the diffusive one. The second Fick's law of diffusion can be derived from EQUATION (2.17) if no velocity field is present and the system is governed by free diffusion

$$\partial_t c = D\,\nabla^2 c. \tag{2.18}$$

The diffusion coefficient D is the parameter that links the spatial and temporal components of the diffusion. Simple dimensional analysis of this equation can already reveal some important physics. If T_0 and L_0 are the characteristic time and length scale over which the concentration $c(\boldsymbol{r}, t)$ varies, then we have

$$L_0 = \sqrt{D\,T_0} \qquad \text{or} \qquad T_0 = \frac{L_0^2}{D}$$

The diffusion coefficient D thus determines how fast a concentration diffuses over a certain distance. In the more general case of EQUATION (2.17), the concentration profiles will depend by the relative weight of the convective and diffusive terms. As previously stated, the low Reynolds numbers found in microfluidics lead to laminar flow and the geometry of microchannels determine Poiseuille velocity profiles. Assuming that L_0, a and b are the characteristic lengths of a rectangular microchannel (i. e. length, width and height, respectively) there are 6 time scales involved, one for each axis for both convection and diffusion. If we consider that in microfluidics channel-networks usually have a planar architecture, mixing between converging channels is almost always in the lateral direction y, so we can consider the characteristic time equal to the lateral convection time $T_0 = \tau_a^{\text{conv}} = a/V_0$. Changing to dimensionless coordinates as we did for EQUATION (2.1), the convection-diffusion equation becomes

$$\frac{V_0}{a}\partial_{\tilde{t}} c + \frac{V_0}{L_0} v_{\tilde{x}}\,\partial_{\tilde{x}} c = \Big[\frac{D}{L_0^2}\,\partial_{\tilde{x}}^2 c + \frac{D}{a^2}\,\partial_{\tilde{y}}^2 c + \frac{D}{b^2}\,\partial_{\tilde{z}}^2\Big] c. \tag{2.19}$$

Introducing the mass diffusion Péclet number Pé, defined as

$$\text{Pé} \equiv \frac{\text{diffusion time}}{\text{convection time}} = \frac{a^2/D}{a/V_0} = \frac{a\,V_0}{D}, \tag{2.20}$$

the convection-diffusion equation can be written as

$$\mathrm{Pé}\left[\partial_{\tilde{t}} + \frac{a}{L_0}\boldsymbol{v}_{\tilde{x}}\,\partial_{\tilde{x}}\right]c = \left[\frac{a^2}{L_0^2}\,\partial^2_{\tilde{x}} + \partial^2_{\tilde{y}} + \frac{a^2}{b^2}\,\partial^2_{\tilde{z}}\right]c. \tag{2.21}$$

For high Péclet numbers convection happens much faster than diffusion, so the solutes tend to move in blocks without distributing in the fluid. Conversely, for low Péclet numbers we observe a dynamics close to the free diffusion. Equation (2.21) also points out that diffusive time scales on the three axes are different and weighted by the coefficients a^2/L_0^2 and a^2/b^2. In particular, since in microfluidics channel-height is usually much smaller than channel-width ($a^2/b^2 \gg 1$), diffusion in the z direction reaches equilibrium faster than the axial and lateral directions, making it possible to treat microfluidic channels as bidimensional networks.

2.2 LAB-ON-A-CHIP & CHIP-IN-A-LAB

The small dimensions of the fluidic elements used in microfluidics allow great integration of components, making it possible to perform on-chip protocols that traditionally required bench-top laboratory equipment[9]. This category of devices is known as lab-on-a-chips (LoCs) and involves an important area of research and an increasing number of industries[21].

However, even though miniaturization has reduced chip sizes, making them small enough to be *theoretically* portable, their portability is still hindered by the need for complex and large ancillary apparatuses (e. g. pumping systems and pressure lines for liquid and valve actuation, microscopes for experiment readout or incubators to control temperature and humidity etc.). This issue had the consequence of splitting the evolution of LoCs: one branch focused on the development of low-cost, portable devices for point-of-care testing[22] and the other focused on exploiting the chips as the high-precision part of a bigger laboratory machine. As a consequence, these devices are also addressed as chip-in-a-lab[23].

In the remaining part of this section I will briefly review some recent studies and discuss the impact of microfluidic devices in biomedical research.

2.2.1 High-throughput biochemical analysis

The most straightforward way to exploit miniaturized fluidic elements is by integrating a great number of them into a single device, in order to achieve parallel analysis and high throughput. A remarkable example is represented by the stud-

ies of Quake et al., who integrated an extremely large number of femtoliter-sized microchambers with almost 1 million pneumatic soft-valves per cm^2 [23,24]. This extremely high density of fluidic elements is currently addressed as microfluidic very large scale integration (mVLSI). Valve-based-microfluidics has the exclusive feature of creating reconfigurable networks, particularly useful when several steps must be performed in parallel and in a precise order—e. g. for parallel single-cell genome amplification[8]. Femtoliter microreactors were also used to scale-down biochemical analyses. An example is represented by digital polymerase chain reaction (dPCR), which consists of dividing a single reaction into thousands of smaller replicas run in parallel, with benefits of increased sensitivity—smaller volumes can be better controlled—and accuracy[25]. A microfluidic dPCR was implemented by Men et al.[26], who developed a chip containing 82 000 micro-wells (on a total area of $2 \times 2\,mm^2$) carved on a PDMS membrane. The chambers are loaded in parallel with 4 μL of sample solution, sealed by pneumatically pressing the membrane on the PDMS floor of the chip, and processed at once. In both the above presented cases and in the great majority of devices of this category[23], the readout is collected by optical microscopes, proving the compatibility between widespread instrumentation and new microfluidic technologies.

2.2.2 Synthesis of nanomaterials for tissue engineering

Microfluidic technologies have recently shown significant potential as novel tools for chemical synthesis. Down-scaling of reaction volumes, achieved using microchannels as reactors, yields for much more controlled chemical environments and therefore more efficient and reproducible synthesis[27]. Throughput can be also scaled-up thanks to the compatibility of microfluidics with parallel and continuous-flow syntheses[28].

The typical size of the microfluidic channels is suitable for the direct production of nano-fibrous polymeric materials[29,30], with promising applications in the field of tissue engineering. Indeed, artificial fibrous scaffolds have attracted attention for their ability to mimic physio-chemical features of biological extracellular matrix (ECM)[31]. Such scaffolds—usually fabricated by electrospinning[32]—can be realized with different biocompatible polymers, and can gradually release drugs[33], yielding for optimal culture conditions also for delicate cell-types[34].

Microfluidic spinning is a valid alternative to the classical and traditional techniques for the fabrication of fibrous scaffolds. Indeed, exploiting phase separation in microchannels, extremely high control over polymerization can be achieved, obtaining micro- and nanofibers with different shape (e. g. solid, tubular, grooved, etc.), size or porosity[30]. The whole fabrication process can be performed in an aqueous

environment, with minimal stress for the fibers. Microfluidic spinning is also compatible with cell-encapsulation within the fibers[35,36]. This is extremely interesting for regenerative medicine, since a careful choice of the cell-type immobilized inside the fiber has the potential for the creation of a plethora of different applications, from scaffolds able to secrete trophic factors helping regeneration[32] to prototypes of artificial organs, like the *artificial pancreas* developed by Jun et al.[37].

2.2.3 Microfluidics and cell-biology

Standard *in vitro* environments to culture cells are represented by Petri dishes and multi-well plates. Even though these devices are cheap, easy to use and suitable for many standard applications, they lack the complete richness found in living organisms and do not allow for precise handling of few- or single-cells. Microfluidic devices can improve the quality of *in vitro* protocols by the production of tools based on the unique properties of fluid dynamics at the microscale.

An important parameter that can be finely controlled by microfluidic devices is the shear-stress. This mechanical stimulation affects almost all cells, with an intensity depending on their physiological role. In living organisms, a whole spectrum of conditions can be found, passing from the high-stresses experienced by endothelial cells in arteries[38] to almost-no-stress required by neurons in the brain[39]. Owing to the velocity profiles characteristic of laminar flow (see SECTION 2.1.2), microfluidics provides efficient tools for the administration of well-defined mechanical stimulations[40]. Moreover, increasing experimental throughput of microfluidic flow-chambers is straightforward, since several flow conditions can be tested on a single device by realizing arrays of channels with different width[41].

Laminar shear-stress and sub-cell-sized filters allowed for the development of label-free methods to sort cells depending on their mechanical properties[42]. Singh et al.[43] developed a very simple flow chamber for highly-efficient collection of human induced pluripotent stem cells (iPSCs), named µSHEAR. The device exploits shear-stress to distinguish between cells with different adhesive strength, yielding for user- and lable-free cell sorting. This difference is related to the change in cell-phenotype consequent to the induction of pluripotence: from the spread morphology distinctive of fibroblasts (the cell-type commonly used for this process[43]) to cells which form tight colonies of round-shaped cells. This morphological change is reflected in a loss of adhesiveness, constituting a sort of *adhesive signature* of the two cell types involved. µSHEAR exposes reprogramming cells to a threshold shear-stress, detaching the poorly adherent ones without influencing the rest of the culture[43]. Detached cells can be easily collected off-chip and expanded to form iPSC

cultures with an extremely high level of purity (up to 97%), higher than the levels achieved by visual identification and isolation in standard culture systems.

Finally, the low Reynolds and Péclet numbers characterizing microfluidics allow for the achievement of an accurate control over chemical gradients in channels and chambers. Chemical gradients are indeed the main actors in mid- and long-distance cell-communication and play a fundamental role in the correct development of tissues[44] and in the response to external stimuli[45]. Chemical gradients cannot be controlled by standard culture devices which only allow for changes in the total volume of the culture medium. On the contrary, the long mixing times characteristic of low Re (see SECTION 2.1.3) are suitable for creating both stable and transient chemical gradients[2,46], making microfluidics a powerful tool to study dynamic behaviors of cells. Given the importance of this topic, many microfluidic gradient generators have been developed in the last decade. It is important to mention the most relevant ones, starting with the *Premixer*[47] and *Universal*[48] *gradient generators*. These devices can create arbitrary-shaped gradients exploiting diffusive mixing in dedicated channels placed before the actual perfusion chamber. A different approach was implemented with the *Microjets device*[49]. This device uses two sets of $1.5 \times 1.5\ \mu m^2$ channels (μJets) to pump small amounts of fluids inside a 200 μm-wide open chamber, pinning the concentration at the exit of the μJets to the concentration of the injected solution and creating a diffusive gradient in the open chamber. Importantly, since the injected volume is neglectable with respect to the volume of the culture chamber, the gradient is formed in the absence of convection and the mechanical stress on the cells adhering in the chamber is minimal. For this reason μJets can be used in combination with particularly delicate cell-types such as neurons[50]. The evolution of gradient generators led to more sophisticated devices able of controlling the shape of the chemical gradients in 2D and found countermeasures to prevent shear-stress-induced cell-damage[51]; however, as discussed in CHAPTER 1, what is still missing is a technology capable of merging the capabilities of microfluidics with the ease-of-use of traditional assays[2,9], overcoming the limits that has thus far hindered its widespread use.

2.3 OPTOFLUIDIC DEVICES

The microscope is one of the most powerful research tool in biology and it is a fundamental companion of microfluidic devices in the laboratory setting, acting as the principal chip-to-world mediator. Microfluidic platforms possess a handful of attributes that enhance the compatibility of microscopes as well, since the arrayed chambers integrated into microfluidic chips make automated image collection

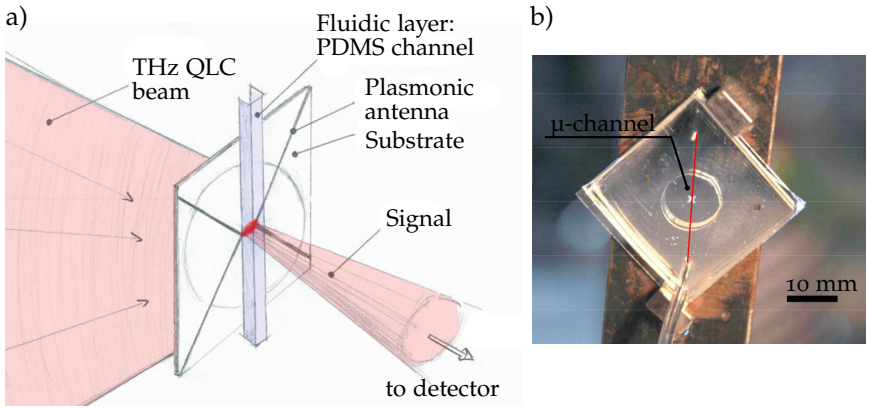

Figure 2.2: Microfluidic-plasmonic probe. (a) Sketch of the on-chip plasmonic antenna coupled with the microfluidic channel. THz radiation is focused on the back of the device and is coupled down to a small volume below the corresponding free-space wavelength. (b) Picture of the assembled PDMS chip. The microchannel is highlined in red.

a straightforward task and machine-vision-based control allows for an efficient fluidic routing in complex channel-networks [23].

In this section I will present the results obtained with three devices developed for optical analysis. The devices described in SECTION 2.3.1 and 2.3.2 focus on the terahertz detection of subwavelength objects and waver-dispersible nano-resonators, while the device discussed in SECTION 2.3.3 provides an application of microfluidic devices as phantoms for photoacoustic imaging.

2.3.1 Terahertz probe of individual subwavelength objects in a water environment

The development of on-chip technologies for terahertz (THz) spectroscopy has attracted considerable attention in the last few years, mainly for its potential impact on biological and biomedical fields. THz radiation can indeed be effectively used to monitor molecular processes and DNA hybridization, or even to influence certain aspects of cellular activity [52].

In order to be of biological or physiological significance, all these measurements require techniques that can be applied to samples in aqueous environments. Water is notoriously highly absorptive in the THz region, however, and this limits the interaction length to few tens of micrometers at most. The fabrication of a practical THz microfluidic system is indeed a major technological and scientific challenge. Indeed, merging THz and microfluidics in a LoC device requires solving three main issues:

1. use of fully biocompatible materials that are transparent in the THz range (and possibly in the visible range, to simplify alignment and monitoring of the chip operation) ready to be integrated with all standard microfluidic on-chip technologies;
2. implement a compact, potentially low-cost, stable, high-power THz source that ensures high signal-to-noise ratios, fast response times, and continuous operation over a long period of time;
3. ensure high sensitivity within highly THz-absorbing material like water over volumes down to the picoliter or the typical living-cell characteristic size of a few micrometers, despite a radiation wavelength that in air is at least on the order of 100 μm.

Here, I present a new portable microfluidic platform for on-chip THz transmission analyses that effectively meets all the above requirements. The system was realized by using conventional microfluidic materials and exploiting a compact THz quantum cascade laser (QCL) as a source[53]. Deep-subwavelength resolution was obtained by integrating a metallic plasmonic antenna on-chip, according to the concept sketched in FIGURE 2.2a.

The antenna consists of a metallic pattern with the form of an elongated X-shaped aperture[54,55]. Its geometry was chosen in order to concentrate the electric field of the impinging radiation into a specific region of space, at least for a given wavelength and polarization of the incident light[56,57]. In our case this region is orthogonal to the central slot of the X. The slot was aligned and in close contact with a microfluidic channel whose width varies from 15 μm to 40 μm, ensuring that most of the transmitted THz light was tunneled through the channel. This microfluidic platform was then used to demonstrate the fast detection and characterization of subwavelength ($< \lambda/10$) objects flowing in a water suspension, and to show the ability to perform a chemical analysis over volumes of the order of a picoliter.

Design

The two functional parts of the chip (i. e. the antenna and the microfluidic platforms) were realized with different materials, according to the requirements of mechanical stability and transparency in the THz region.

The fluidic layer consists of two PDMS parts assembled by oxygen-plasma bonding[5] (see APPENDIX A for additional details). A single microchannel (FIGURE 2.3) was localized in the 500 μm-thick bottom stratum, surmounted by a 4 mm-thick piece of PDMS. This second layer provided the mechanical stability for the connections with the external tubing and has a 10 mm radius hole in the central region, necessary to reduce radiation absorption in correspondence to the optical path.

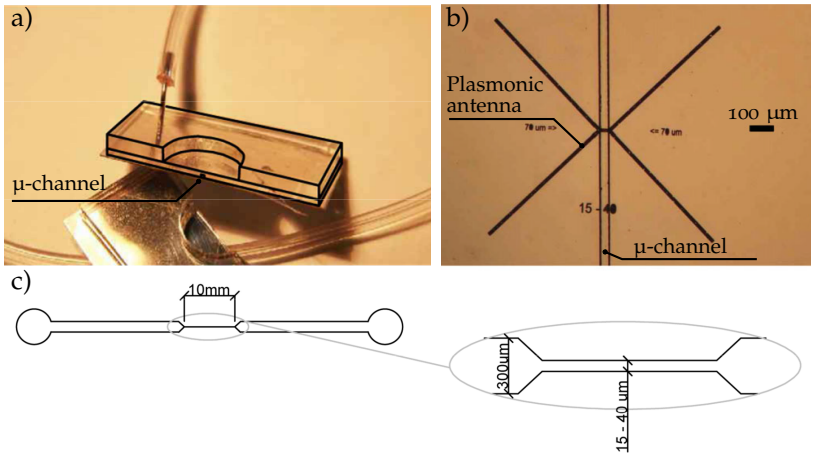

Figure 2.3: Architecture of the microfluidic chip. (a) Cross-section of the device showing the antenna-layer (bottom) and the two PDMS layers (edges were underlined for a more clear visualization). (b) Microscope image of a microfluidic channel aligned over the plasmonic antenna. (c) Design of the fluidic layer of the chip.

For the antenna we used a 300 μm thick cyclic olefin copolymer (COC) substrate, located in close contact with the microchannel, providing a seal for the microfluidic layer. COC meets transparency demands with acceptable THz loss[58] ($\alpha < 1\,\mathrm{cm}^{-1}$ at 3 THz) and is strong enough to withstand sufficient liquid pressure even when thin layers are used. The antenna was patterned on the evaporated metal surface by standard ultraviolet (UV) lithography followed by dry etching using an inductively coupled plasma reactive ion etching machine (ICP-RIE), as detailed in reference[57].

Subwavelength object detection

The main objective of this device was to demonstrate on-chip dynamic THz detection and assay of individual subwavelength objects flowing in the water channel. In order to prove this capability, we used poly (styrene) (PS) microparticles; these are commercially available in water suspension (FLUKA Sigma-Aldrich), offer a highly monodisperse diameter distribution (standard deviation in diameter < 0.3 μm), and possess very low THz absorption with respect to water[59]. These particles are often used to mimic cells for fluid-dynamics experiments in microfluidic chips[60]. In particular, we used particles of two different diameters, 10 μm and 20 μm, corresponding roughly to $\lambda/11$ and $\lambda/6$, respectively, for the 2.6 THz radiation used here.

To establish a suitable flow rate we first observed and recorded particle transits by means of a CCD camera. The purpose was to verify that, on average, no more

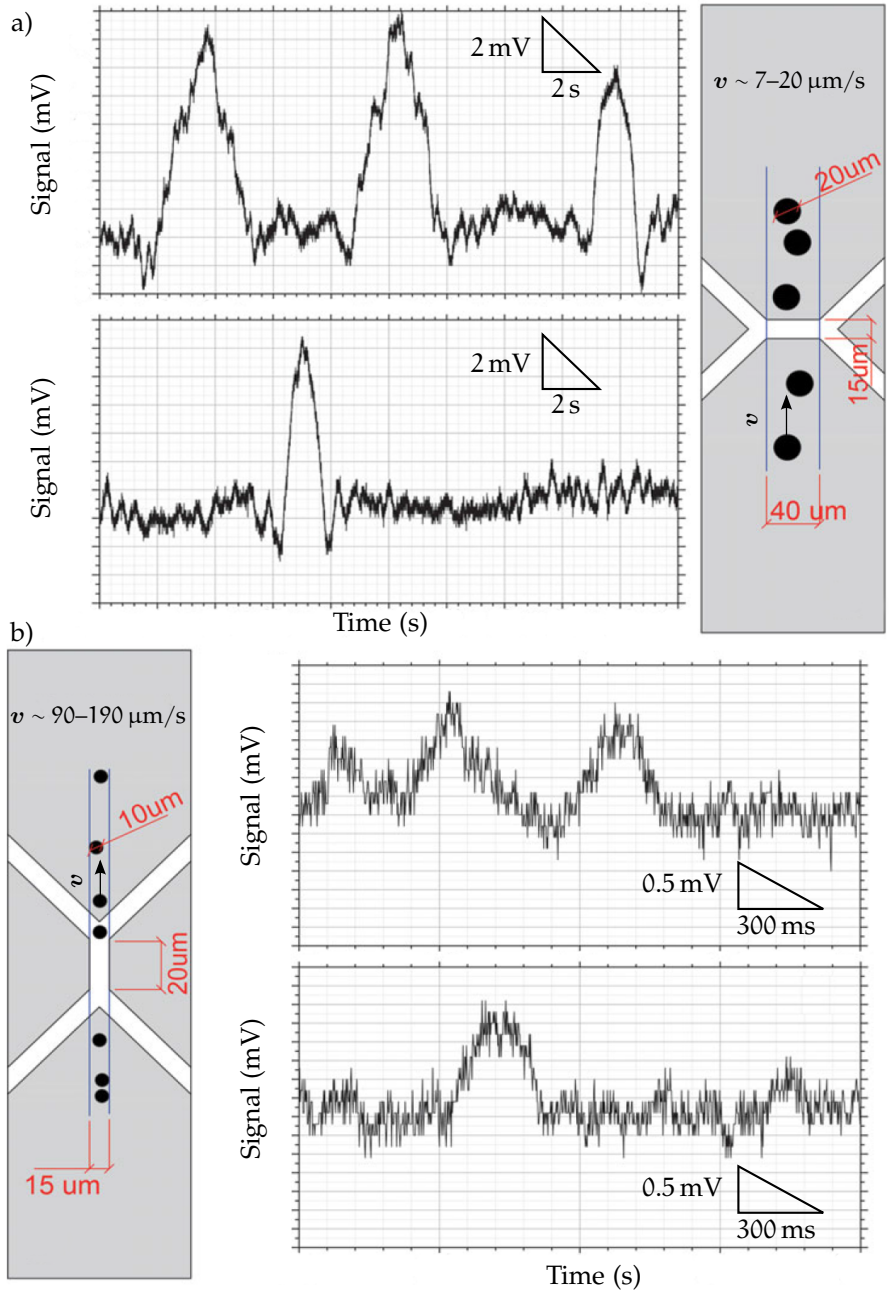

Figure 2.4: Detection of subwavelength particles. Signal detected when (a) 20 µm and (b) 10 µm diameter PS beads were transiting over the antenna. The respective chip configuration is schematized in the gray boxes.

than one particle was present at the same time in the portion of the chip probed by the THz beam, and also that the flow speed was compatible with the lock-in acquisition time. The typical rate employed was of the order of 1 particle per second. We then moved the sample from the CCD inspection area to the THz beam line using an automated-motorized XYZ system. The THz set-up is described in detail in APPENDIX B.1.

FIGURE 2.4 and 2.5 display the transmitted THz signal recorded in such experiments for 3 different microfluidic chips. FIGURE 2.4 reports individual measurements of particles passing through chips having different channel widths, depicted by the insets. The measurements reported in FIGURE 2.4a were performed using a chip with a 40 μm wide channel and particles of 20 μm diameter, while those of FIGURE 2.4b exploited a 15 μm wide channel and particles of 10 μm diameter. This latter chip was specifically designed with the microfluidic channel placed parallel to the slot of the metallic antenna: this configuration is very useful for small particles because it increases particle *fly time* in the sensing area, with consequent increase of the signal-to-noise ratio. In both cases THz transmission peaks were clearly detected as a function of time, in coincidence with each passing particle, since the absorption in the beam path is reduced by the presence of the almost transparent object replacing a corresponding volume of absorbing water. By dividing the distance traveled over the aperture by the particle *fly time* deduced from the graphics, we obtained its velocity. The velocity calculated for the peaks of FIGURE 2.4 varied between 7 and 20 μm/s for the 20 μm diameter particles and between 90 and 190 μm/s for the smaller ones. These values are consistent with those observed with the CCD camera. We could not directly and precisely correlate the peak amplitudes observed in FIGURE 2.4a with those of FIGURE 2.4b in terms of particle diameter. The reason is the different chip geometry and focalization efficiency of the plasmonic structures. Nevertheless, the peak height in the detector signal was of the order of 1 mV for the 10 μm diameter particles and of the order of 10 mV for the bigger ones, reasonably in line with what was expected from the particle volume.

FIGURE 2.5 reports data for the 1:1 mixture of 20 μm and 10 μm diameter particles passing in the same 40 μm microfluidic channel. Two families of peaks with different intensities clearly appeared, each relative to one of the particle species (FIGURE 2.5b). The graphs also shows a third family of high-frequency sharp peaks uncorrelated with passing particles. These peaks are indeed noise arising from pressure oscillations in the channel created by the pressurization lines. The analysis of the peak events is reported in FIGURE 2.5b as a function of their amplitude; they are clearly grouped into two different families of transiting objects. The ratio between the average peak amplitude of each group is 4 ± 1, to be compared to the value of 7 ± 1 expected from the difference in particle volume calculated taking into account the nominal uncertainty of 2–3% in diameter size provided by the producer. The ex-

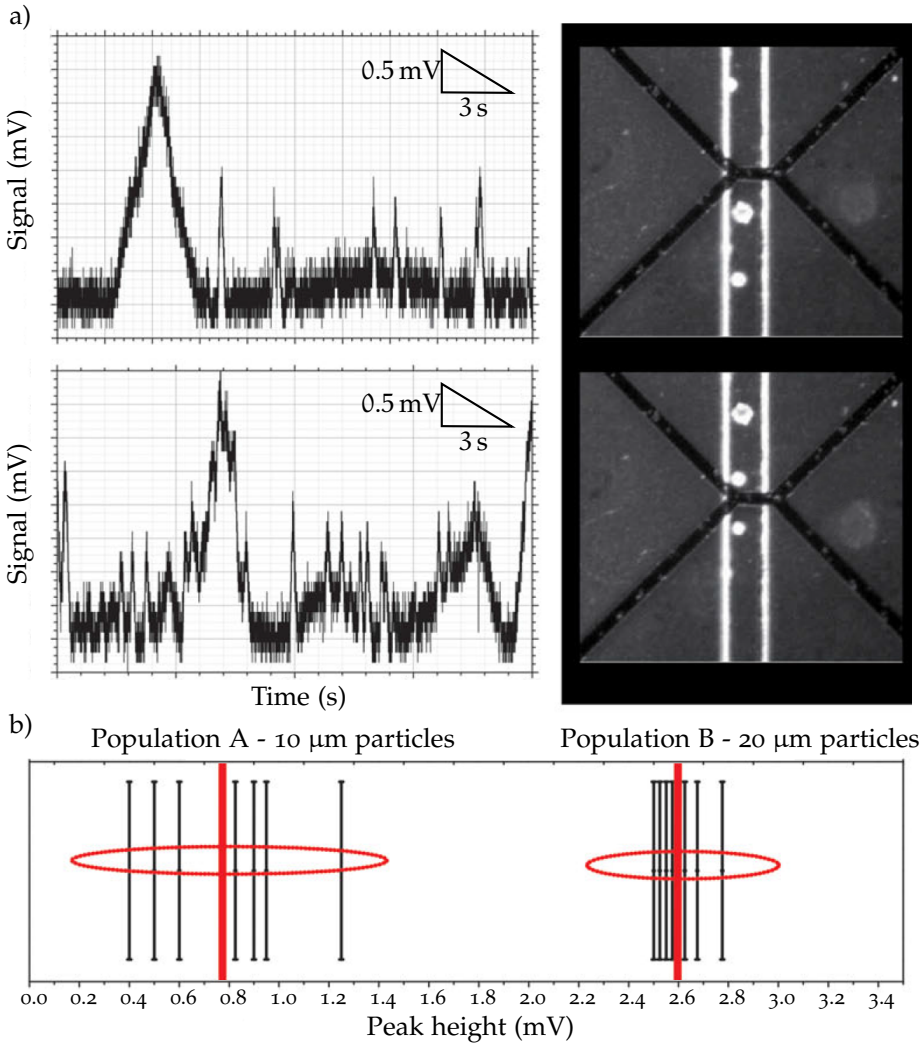

Figure 2.5: Simultaneous detection of particles with different diameter. (a) Transmitted signal in time showing the transit on a 1:1 mixture of 10 μm and 20 μm-diameter particles. The images on the right represent typical particle-crossing events. (b) Analysis of peak-height. The plot shows the intensity associated to each particle-crossing event. Red bars represent the average peak-height calculated for the two populations reported in the graph.

pected ratio is not 8, as that of the sphere volumes, because the 20 μm particles are larger than the slot in the metal, and thereby are not fully illuminated by the THz radiation. Possible reasons for this discrepancy can be ascribed to:

- Microfabrication uncertainties: the actual aperture size of the antenna in the experiment can be up to 20% smaller, which would impact only the 20 μm particles signal producing a theoretical ratio of 7 ± 2 that would be compatible with the results;
- The energy distribution of the THz field inside the open area is not homogeneous but more intense in the center, thereby producing larger signals for the small particles;
- The presence of the surfactant in the solution and surface hydration of the polystyrene spheres can produce an additional absorption change proportional to the sphere surface (not to its volume). A detailed investigation of this effect was not possible in our set-up and it is beyond the scope of the present thesis. We can argue, however, that such a hydration shell involves just a few water molecular layers surrounding the sphere surface[61]. Considering that the expected relative absorption change with respect to bulk water is limited to a few percent, it should be a negligible contribution to the observed THz particle signal.

Conclusions

The peaks appearing in the THz-transmission time traces are the microparticles THz fingerprints. Since in our proof-of-concept experiment particle constituents were identical and weakly absorbing in the THz, the capability of distinguishing 2 species was actually just based on their respective size, leading to a weaker or stronger transmission. Clearly, potential bio-applications would rather target in the future quantitative differences in the spectroscopic THz response, for instance arising from differences in composition, molecular resonances, etc. From an experimental standpoint, the measurement is anyway equivalent, since it is exclusively based on the analysis of the THz-signal peak intensity. Of course, in the case of sharp resonances, more detailed information could be obtained resorting to a tunable source and investigating the spectral dependence of the signal. Note that the developed technology already employs broadband optical elements and is therefore directly suitable for spectroscopic applications. Our results unequivocally showed that a LoC for deeply subwavelength THz analyses in a microfluidic environment is a reality. Our system was based on a QCL source and successfully merged plasmonic-focusing structures with standard microfluidic technologies adapted to ensure compatibility with THz

spectroscopy. Furthermore, these experiments showed the crucial capability to operate in water, in real-time speed, and on single objects as small as 10 μm ($< \lambda/10$), the typical size of a biological cell. Finally, our data proved the applicability of our approach to recognition and sensing even in the dynamic fast-transit configuration that is required for instance by sorting and/or large statistics applications. We believe this technology can contribute to the development of THz-based spectroscopy of biomolecules at the cell level, with exciting perspectives for label-free applications.

2.3.2 Water-dispersible three-dimensional LC-nanoresonators

In SECTION 2.3.1 I introduced a microfluidic device exploiting a plasmonic antenna to focalize the electromagnetic field in a subwavelength region. In this section I report the use of plasmonic nanoparticles as sensors compatible with aqueous environments.

Nanoparticles can be produced by different approaches. Chemical synthesis is an established methods to obtain metal nanoparticles, whose surfaces can be functionalized to obtain stable dispersions in liquids, and to selectively detect molecular interactions. This bottom-up approach, however, presents some limitations. First, the optical properties of these nanoparticles are determined by the intrinsic characteristics of the material they are made of, and can be tuned within a very limited range of resonance frequencies. Moreover, the repertoire of structures that can be synthesized is limited, thus limiting the possibility to tailor and fine-tune their properties by playing with shape and size.

Alternatively, a top-down nanofabrication approach can be used to realize arrays of nanoantennas and nanoresonators with controlled optical properties and sensing capabilities. These metamaterials can be designed to have an optical resonant response in widely different regions of the optical spectrum, from the visible[62] and near infrared (IR)[63,64] down to the THz[65,66]. Moreover, modern nanolithography techniques allow as to obtain composite nanodevices with complex shapes and accurately controllable properties. The main drawback of these fabrication protocols is that the produced devices are anchored on a support substrate, so a strategy for the detachment is needed if the devices are meant to be used in liquids.

LC nanoresonators

In this study I tested LC nanoresonators developed by Clericò et al.[67]. These resonators have a rectangular geometry (230 nm × 115 nm lateral sizes) and a 3D, wafer structure, consisting of one layers of aluminium (50 nm, bottom layer), one of aluminium oxide (40 nm, middle layer) and one of gold (50 nm, top layer). This device

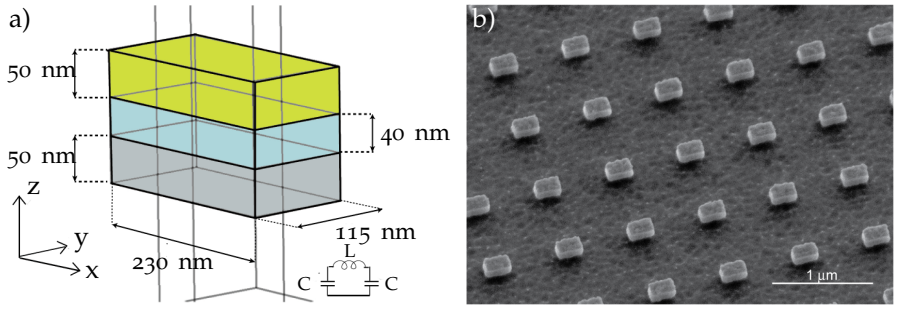

Figure 2.6: Design of the LC-nanoresonators. (a) Schematics of a single resonator and equivalent electrical circuit. (b) SEM image of an array of resonators.

can be described as a nanoscopic circuit (FIGURE 2.6), when a harmonic magnetic field with a component normal to the plane (x, z) excites it. In this case two antiparallel currents in the metals are generated and this loop current determines an inductive regime, while the accumulation of opposite charges in the extremities of the upper and lower metal slabs creates a capacitive coupling in those areas. The resulting LC resonance, beyond the dependence on sizes and shape, is strongly influenced by the dielectric constant and magnetic permittivity of the external environment, and can be used as a way to probe the local environment, and chemical binding at the surface of the nanodevice.

Resonance measures in liquid

In order to demonstrate the use of these devices as biosensors, transmission spectra were acquired while immersing the nanoresonators in different liquids. To this end, I realized a PDMS microfluidic device (see APPENDIX A.2.1 for details) with two 1.88 nl chambers—one for the sample and the other to measure the background signal. The chip was covalently bonded to a glass coverslip aligning the 250 µm × 250 µm big signal-chamber to a 250 nm × 125 nm array of nanoresonators fabricated on the glass. Reference gold markers were also created on the coverslip to control the spot size and to align the beam focus on the array of nanoresonators (FIGURE 2.7). Transmission spectra were acquired with a commercial Fourier trasform infrared (FTIR) Nexus spectrometer equipped with a white light lamp and a PbSe detector.

Water, ethanol, isopropanol were flushed into the chip at 0.4 µl/ min, using an external syringe pump (Harvard apparatus). Before and after each measurement, the microchamber was cleaned with deionized water (DI-H_2O) water and dried for 15 min by exposure to an external lamp. In FIGURE 2.8a the shift of the resonance is reported as a function of the refractive index of the different liquids that were injected

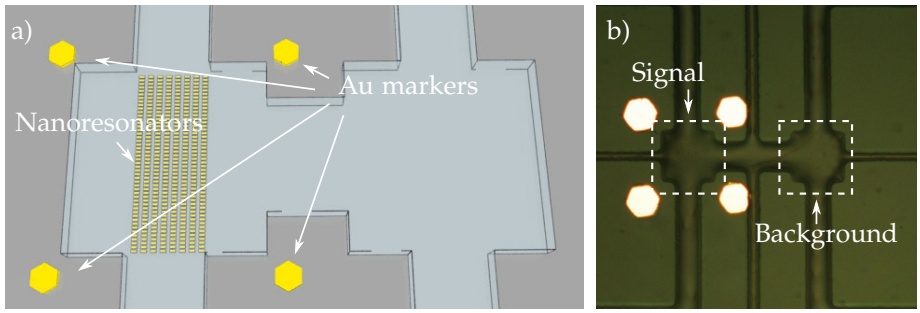

Figure 2.7: Microfluidic device for detection of LC-nanoresonators. (a) Sketch of the microfluidic chambers used for the detection of LC-nanoresonators in acqueous environment and (b) microscope image of the actual microchannel network used.

into the microfluidic chip[68–70]. The 4 data-sets were acquired at room temperature in 4 separate experimental sessions in 2 different days to test the repeatability of the measurement. The time of each measurement was 30 min.

In order to quantify the ability of the nanoresonators to discriminate between different environments, the change in the position of the resonance peak in for the three above mentioned liquids was measured as the bulk sensitivity S, that is defined as the spectral shift $\Delta\lambda$ originated by a certain refractive index change Δn of the external environment,

$$S = \frac{\Delta\lambda}{\Delta n}. \tag{2.22}$$

Bulk sensitivity was calculated from the slope of the linear fit, resulting in 280 nm per refractive index unit. The performance of the device was determined by its figure of merit, i. e. the sensitivity S divided by the full width half maximum (FWHM) of the resonance. In our experiments we found a figure of merit of almost 6. The sensitivity of the resonance peak position and line-shape to the chemical-physical features of the local environment makes these devices promising for sensing applications.

Detection of solutes

The resonance of these nanodevices was influenced by the chemical binding of molecules to one of the metal facets as well as by the dielectric properties of the external environment, enabling the detection of specific molecular interactions or the kinetic study of chemical binding. We measured the transmission spectra of the nanoresonators at different time-points while a solution 1:1000 of cysteamine and

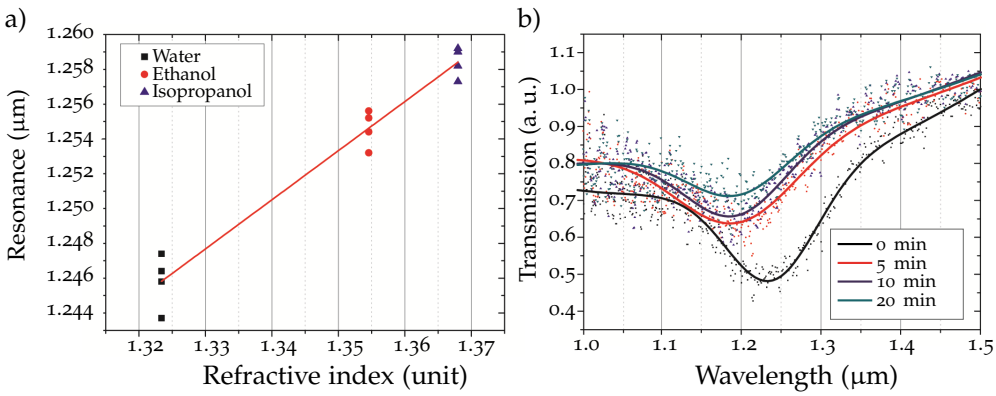

Figure 2.8: On-chip optical detection of LC-nanoresonators. (a) Shift of the resonance for 3 liquids with different refractive indexes injected into the chamber. The linear fit is represented by the red line. (b) Transmission spectra resolved in time during cysteamine-binding. The graph shows a blue shift associated to the cysteamine-binding.

water was flowing through the microfluidic chip. Cysteamine is known to bind to the gold layer with its thiol groups[71]; in a circuit model, it acts as an external impedance that causes a damping of the resonance[72]. This behavior is reported in FIGURE 2.8b, witnessed by a blue shift of the transmission spectra.

Conclusions

The nanoresonators proposed here showed several interesting properties, making them a candidate for several application requiring detection of particles in water environments. In particular, I want to stress that:

- the top-down approach allows for the design of their optical response;
- the dependence of the resonance frequency from the environmental composition enable the use of the nanoresonators as sensors of the physical-chemical environment;
- the nanoresonators can be fabricated on transparent supports compatible with LoC applications as well as on sacrificial materials (e. g. Gallium Arsenide[67]) allowing for their detachment and use *in vivo* as colloidal suspension.

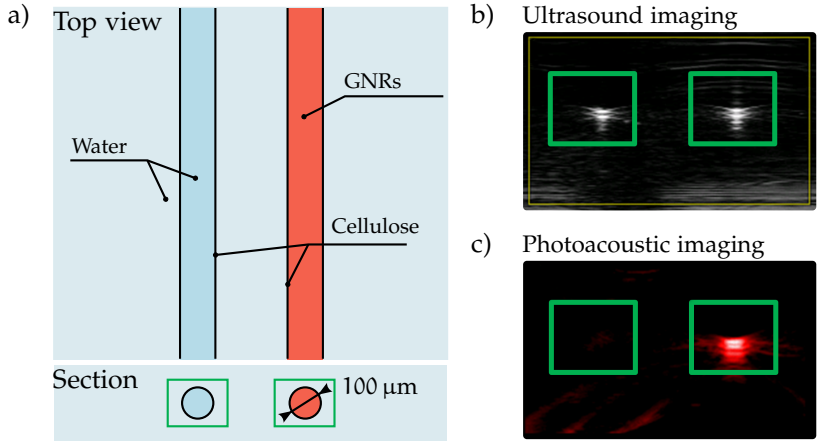

Figure 2.9: Gold nanorods in photoacoustic imaging. (a) Scheme of the cellulose microcapillaries used to test the photoacoustic system. The capillary on the left is filled with water, the other with the GNRs. (b) Ultrasound imaging of the two capillaries. No difference between the capillaries can be seen. (c) Photoacoustic imaging. Signal is collected only from the capillary filled with the GNRs.

2.3.3 Microstructured phantoms for photoacuostic imaging

Photoacoustic imaging (PAI) and therapies are emerging techniques that combine the high-contrast and spectroscopic specificity of optical methods with the spatial resolution of ultrasonic imaging[73,74]. In PAI, ultrasounds are generated by optical excitation, usually provided by a laser. The light is absorbed by endogenous chromophores (e. g. haemoglobin, melanin, water or lipids[75]) or exogenous contrast agents (CAs)[76] which produce a localized increase in temperature. The consequent thermoelastic expansion generates broadband acoustic waves that can be detected using ultrasound receivers. Since ultrasounds travel through tissues with minimal scattering and attenuation, PAI is capable of locating optically absorbing objects deep within tissue, providing advantages over other optical methods.

In order to enhance the sensitivity and spectroscopic specificity of photoacustic signals, CAs are used. CAs are substances selected for their physical properties (i. e. high optical absorption and acoustic emission wavelengths) and interaction with living tissues (i. e. minimal interplay with healthy tissues and efficient targeting of diseased ones). The fitness of a CA for a certain application can be defined only in combination with the detection apparatus, testing on models capable of mimicking soft-tissue properties. These models are known as *phantoms*. In this section I am reporting my results testing the performance of GNR as contrast agents for photoacoustic imaging.

Material	Impedance Z (KRayl)	Velocity (m/s)	Density (g/cm^3)
Air[81]	0.04	330	0.0013 (at STP)
Blood[81]	161	1570	1.04
Soft tissues (avg)[82]	163	1540	1.01–1.06
Bone[83]	780	4080	1.5–2.0
Water[81]	148	1480	1.0
PDMS[84]	150	1300	1.5

Table 2.1: Mechanical properties of soft tissues. Table reported from reference[85]

Gold nanorods

The physical and optical properties of GNRs make them good candidates as contrast agents for PAI[73,76,77], since they exhibit minimal toxicity and are suitable for conjugation with ligands to gain molecular specificity. Their absorption spectrum displays a longitudinal plasmonic mode with a peak whose position can be controlled by changing the aspect ratio of the rods and placed within the near-infrared window—the range of wavelengths where light exhibits deepest penetration into biological tissue[78]—i. e. in the interval 650–900 nm.

The GNRs used here were produced by Dr. Ratto, from CNR, Istituto di fisica applicata of Firenze (Italy) according to the protocols previously reported[79,80] (see APPENDIX A.3 for additional details). The length of the rods was 53 nm with a lateral diameter of 11 nm, resulting in an excitation peak at 840 nm with a FWHM of 160 nm. The acousto-optical behavior of these rods is shown using a simple phantom composed of two semi-synthetic cellulose capillaries immersed in water, with diameters of 100 µm (FIGURE 2.9a). One of the capillaries was filled with a suspension of GNRs, the other one with water. Since the two capillaries have identical dimension and acoustic impedance, no appreciable difference can be detected using ultrasound imaging (FIGURE 2.9b). Using optical excitation instead, is possible to distinguish the capillary filled with GNR from the one filled with water (FIGURE 2.9c).

Microfluidic phantom

The device presented here is a microfluidic chip designed to mimic the mechanical and topographical properties of vascularized soft-tissues. The chip was created by means of standard PDMS soft lithography using an SU8 mold (see APPENDIX A.2.2 for additional details). The fluidic layer is composed by 6 parallel channels whose lateral size varies from 50 to 500 µm, comparably with those of the tiniest fluidic

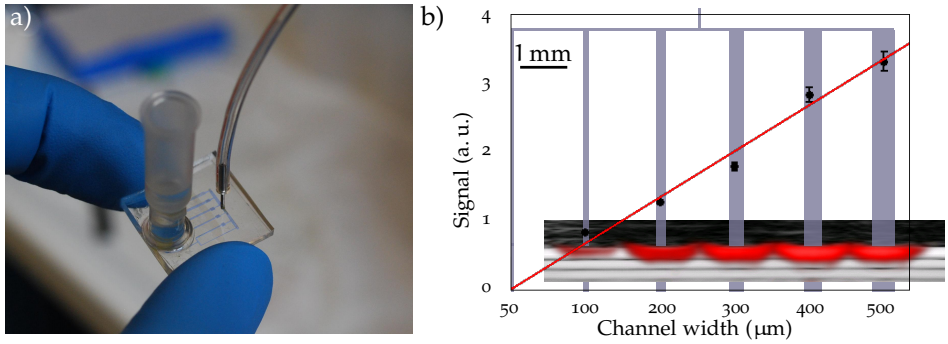

Figure 2.10: PDMS microfluidic phantom. (a) Picture of the microfluidic phantom. (b) Plot of the intensity photoacoustic signal and linear fit of the distribution (red line). The ultrasonic image (grayscale) is superimposed to the PAI (red bands). The geometry of the microchannel network is represented in blue, the width and the spacing of the channels is in scale with the PAI.

elements found in human bodies—i. e. the blood vessels composing the microcirculation[86]. In particular, the microchannels have lateral size of 50, 100, 200, 300, 400 and 500 μm (FIGURE 2.10a), and a thickness of 50 μm.

The optical and acoustic properties of PDMS make it a suitable material for PAI, because its optical transparency leads to low attenuation during optical excitation and its acoustic impedance (parameter derived from the mass density of the material and the velocity of the acoustic wave in it) is comparable with those of soft tissues[85]. Typical values of acoustic impedance for several biological tissues are reported in TABLE 2.1 on the preceding page.

Photoacoustic measurements were performed in collaboration with the group of Dr. Menichetti, from CNR, Istituto di fisiologia clinica of Pisa (Italy). The microchannels were loaded with a 87 nM solution of GNRs in water. FIGURE 2.10b shows the quantification of the photoacoustic signal (S) collected as a function of channel width (w_i, with i=1:6). As expected, the signal increased linearly with the width of the channel. Indeed, the intensity of the generated ultrasound is proportional to the number of GNRs in the integration volume, $n_i = C_i V_i$. Since all the channels were loaded with the same concentration of nanoparticles ($C_i = C_0$), the amount of GNRs excited by the laser was determined by the lateral width of the excitation beam (d) and the cross-section of the microchannel. In this particular chip, since all the channels have the same height ($h_i = h$):

$$S_i = \alpha C_0 V_i = \beta w_i,$$

with $\beta = \alpha C_0 h\, d$. FIGURE 2.10b also shows that the signal from the 50 µm-channel could not be detected, suggesting that the detection limit was reached.

Conclusions

The chip proposed here has shown the optical and acoustic properties desirable for photoacoustic applications. Moreover, the reduced size of the chip and the precise control over channel-network geometry allows for a great versatility in modeling the structure of vascularised tissues. Overall, these results proved that microfluidic devices posses promising features that make them suitable for the construction of phantoms for PAI.

2.4 TAILORING CO-CULTURES IN CLOSED CHAMBER

In the previous section I discussed LoC devices meant to be a key component of wider analysis systems; in this section I will concentrate on a *stand-alone* microfluidic system designed for cell-culturing in a highly controlled environment.

Microfluidics has brought great improvements to tissue culture devices, allowing fine control over the local chemistry[46] and physics[40] of extracellular environment *in vitro*, owing to the highly predictable fluid dynamics characterizing fluid flow at the microscale (see SECTION 2.1.1). A number of bio-devices were proposed to study relevant cell biology aspects, such as cell migration[87], axon guidance[88] and stem cell differentiation[89]. Although devices such as these have shown great potential, several drawbacks have limited their widespread use in cell biology. Indeed they typically require complex fabrication processes, bulky external pressurization systems for valve and liquid actuation that are normally connected to the microchip by fixed tubing. Additionally, dedicated skilled operators are necessary to run such experiments. Recently, a few alternative ways to actuate and control flows in microenvironments were proposed, using cells themselves to drive liquid routing[90] and open chambers to facilitate cell loading and medium exchange[91].

Here, I introduce an original microfluidic gradient generator for culturing cells in closed microchambers that is compatible with standard biological procedures and does not require external control units and tubing. Its architecture allows easy handling of the liquids and simple and efficient cell loading protocols to position selected cell types in different areas of the microchamber. Co-cultures with an initial topographical organization were set up, and migration and chamber colonization processes were studied by time-lapse microscopy. Finally, the chip was applied to the study of the anti-cancer properties of catechin–dextran conjugate.

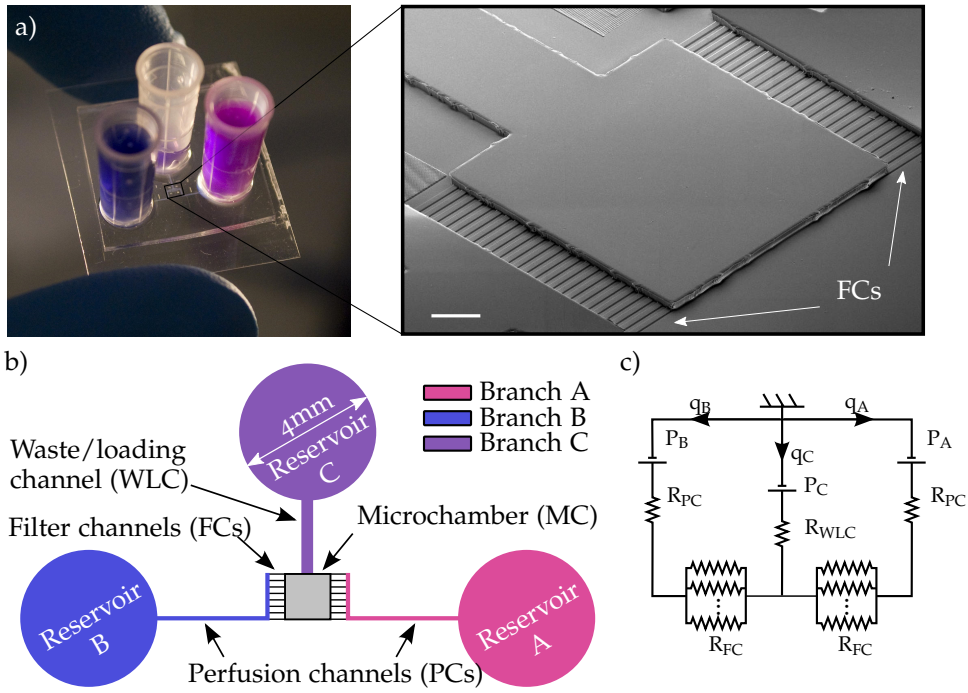

Figure 2.11: Microfluidic chip architecture. (a) Photography of the PDMS chip and SEM image of the microchamber (MC) and filter channels (FCs). Scalebar 100 µm. (b) Schematics of the whole microfluidic network. (c) Simplified equivalent circuit of the fluidic impedances.

2.4.1 Chip Architecture

A schematic view of the chip design is shown in FIGURE 2.11. The fluidic network is composed of a central 7.5 nL chamber ($500 \times 500 \times 30\ \mu m^3$), from which three channels depart in a T-shaped geometry. These channels connect the microchamber (MC) to open liquid reservoirs (LRs), which can be filled by standard pipetting, providing a hydrostatic pressure of 150 Pa. Two sets of $2.5 \times 10\ \mu m^2$ parallel microchannels are located between the MC and the two lateral channels (see FIGURE 2.11) acting as filters for suspended microparticles and, during cell loading, as barriers for suspended cells. For this reason, in the following they will be called filter channels (FCs). Their hydraulic resistance is much greater than the other microchannels (TABLE 2.2) so that more than the 90% of the total pressure drop is located at their ends. As a consequence, morphological imperfections of the fluidic accesses or along the large-section microchannels marginally affect the pressure values at the 3 open sides of

	$L \times w$ (μm²)	h (μm)	A (μm²)	R (mBar s/nL)
Perfusion channels	$3\,000 \times 150$	30	$4.5 \cdot 10^3$	$10.19 \cdot 10^{-2}$
Waste/loading channel	$2\,000 \times 200$	30	$6.0 \cdot 10^3$	$4.92 \cdot 10^{-2}$
Filter channels	100×10	25	2.5	91.34

Table 2.2: Channel geometrical characteristics and hydraulic resistance. L, w and h are channel length, width and height, respectively, A is channel cross-section and R is the hydraulic resistance calculated by equation (2.15)

the MC and its fluid dynamics. Details on the fabrication of the chip are reported in APPENDIX A.2.3.

The chip hydraulic resistance was dimensioned in order to have a fast liquid turnover in the MC while minimizing the flow rate and, consequently, the shear-stress applied to the cells. This point is crucial, since high flow rates lead to rapid equilibration of the liquid levels in the reservoirs and to the end of the perfusion. Owing to the FC high resistance, however, the maximum flow rate achievable using the hydrostatic pressure provided by the reservoirs is limited to 2.5 nL/s. Given the large volume of the reservoirs, the pressure drop is reduced only by the 2%/h of chip operation—for 450 mL reservoirs. Nevertheless, this flow rate corresponds to a turnover time of the liquid in the MC of 3 s, assuring a fast delivery of fresh nutrients to the cells and washout of metabolic wastes.

2.4.2 Fluid dynamics

The fluidic behavior in the MC is determined by the balance of the flows through the lateral channels, called perfusion channels (PCs), and the central channel, called the waste/loading channel (WLC). Given the symmetry of the devices, 2 pressure differences ΔP_S and ΔP_D were defined to describe the MC fluid-dynamics:

$$\begin{cases} \Delta P_S = P_A - P_B \\ \Delta P_D = P_C - \frac{P_A + P_B}{2} \end{cases} \tag{2.23}$$

where P_A, P_B and P_C are the pressures at inlets A, B and C, respectively. The hydraulic resistance of the microchannel network—see EQUATION (2.15) on page 11—was chosen so that fluids could be actuated using the hydrostatic pressure provided by the reservoir liquids. The resulting equivalent circuit is represented in FIGURE 2.11C and

Standard operating mode		ΔP_D (Pa)	ΔP_S (Pa)
Symmetric	loading	150	0
	perfusion	−150	0
Asymmetric	right-side loading	75	150
	left-side loading	75	−150

Table 2.3: Standard operating modes. The table reports the input pressures associated to each standard operating modes defined in this section.

the value of each element of the circuit is reported in TABLE 2.2. ΔP_S and ΔP_D were used to calculate the flow rates along the branches A, B and C ($q_{A,B,C}$):

$$q_A = \frac{1}{2R}\Delta P_S - \frac{1}{R + 2R_{WLC}}\Delta P_D, \tag{2.24a}$$

$$q_B = -\frac{1}{2R}\Delta P_S - \frac{1}{R + 2R_{WLC}}\Delta P_D, \tag{2.24b}$$

$$q_C = \frac{2}{R + 2R_{WLC}}\Delta P_D \tag{2.24c}$$

where R_{WLC} is the hydraulic resistance of the WLC and R is the equivalent seen from the MC to $LR_{A,B}$ ($R = R_{WLC} + R_{FC}/25$).

EQUATION (2.24c) show that the sign of ΔP_D determines the flow direction in the central channel q_c. For positive values the liquid flows from LR_C to the MC, passes through the FCs and reaches LR_A and/or LR_B; in the following we will refer to this case as *loading mode*. For negative values ($\Delta P_D < 0$) the flow direction is inverted, and the liquid enters into the MC from one or both the PCs, and reaches LR_C. This operating mode will be called *perfusion mode*. The balance between flows in the PCs is regulated by ΔP_S: the flow is symmetric if this variable is equal to zero and spatially biased otherwise. The difference between the flow rates $q_A - q_B = \Delta P_S/R$ can be used to insert a lateral flow drift in the MC. This bias reaches a critical point for:

$$|\Delta P_S| = \frac{2R}{R + 2R_{WLC}}|\Delta P_D| \tag{2.25}$$

corresponding to the virtual exclusion of one of the two PCs from the fluidic network ($q_i = 0, q_j = q_C$, with $i, j = A, B$ and $i \neq j$).

In order to assess device performance in creating and controlling different fluidic configurations, several combinations of ΔP_D and ΔP_S were simulated by finite ele-

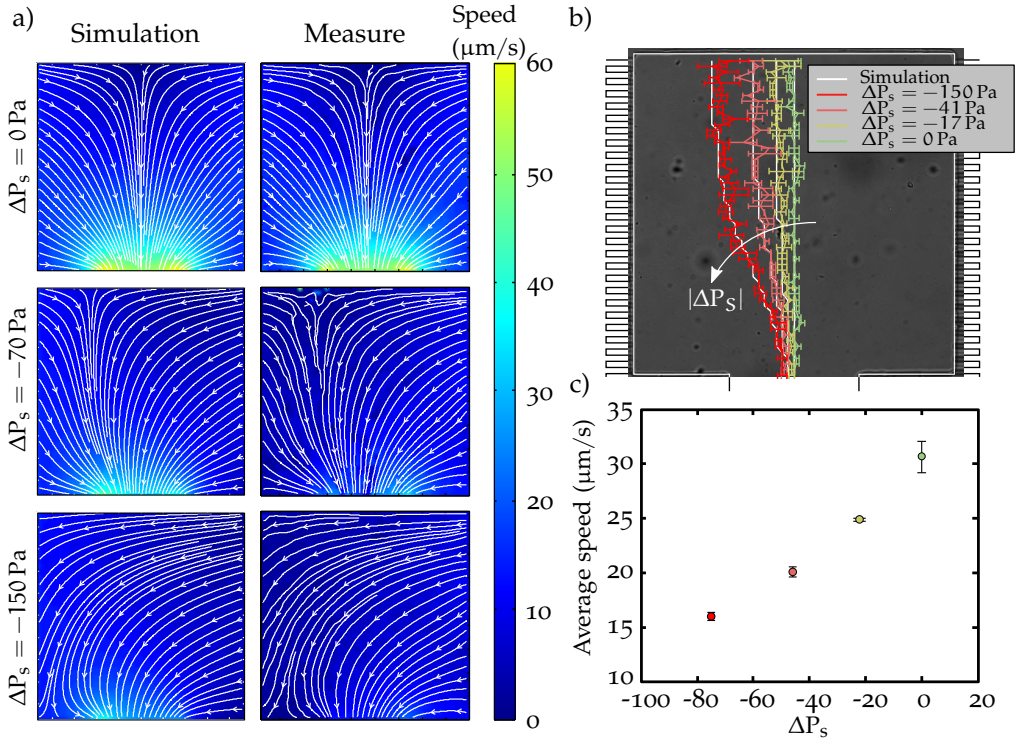

Figure 2.12: Chip fluid-dynamics characterization. (a) Comparison between calculated and experimental velocity fields in the MC. (b) Unbalanced flow in the MC: the position of the interface between fluid flows from the PCs is calculated (solid line) and measured (coloured bars) for different values of ΔP_s. The average speed of each pressure configuration is plotted in (c).

ment method analysis and experimentally characterized by spatio-temporal image correlation spectroscopy (STICS)[92], as detailed in APPENDIX B.2. Data reported in FIGURE 2.12 demonstrate that the hydrostatic pressure alone could finely control the microfluidic device, and that all measurements agreed remarkably well with data obtained *in silico*. As expected, laminar flow dominated the fluid dynamics in the MC ($Re = 8 \cdot 10^{-4} \ll 1$, $Pé = 10 \gg 1$) and as a consequence, opposite parts of the MC could be chemically decoupled by operating in perfusion mode. This is achieved if the diffusion of the solute molecules is slow compared to the fluid velocity in the MC. For example, in the case of a small molecule in water (e. g. glucose, diffusion coefficient $D_g = 600\,\mu m^2/s$), the time required for complete diffusion within the MC is of the order of 104 s, a value much greater than the typical fluid turnover time (7.5 s for a slow rate of 1 nL/s). The velocity field in the MC (FIGURE 2.12) could be used to calculate the shear-stress experienced by cells. According to EQUATION (2.10),

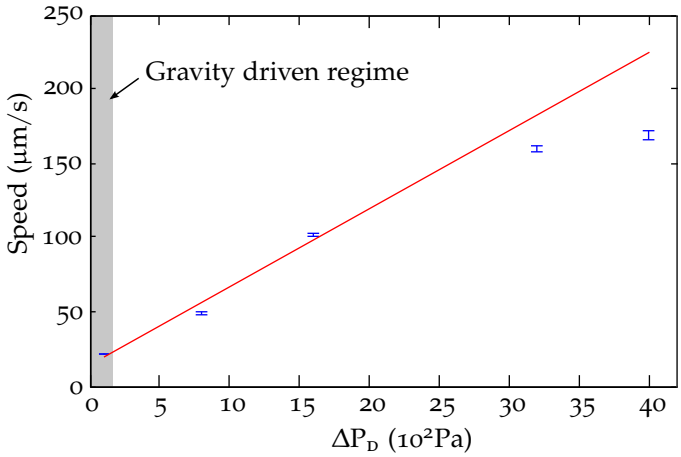

Figure 2.13: Speed measurement in active-pressurization-mode. Measure of speed (SD reported as blue bars) in the MC during active pressurization. A linear fit of the first three points (pure resistive regime) of the curve (red line) is reported.

the maximum spatially-averaged value, obtained for standard symmetric perfusion, is 8.3 ± 0.4 mPa. Yet, 90% of the MC area experience shear-stress values lower than 15 mPa (see APPENDIX B.3 for details).

Hydrostatic- and active-pressurization

An increasing number of studies are proposing hydrostatic-pressure-driven microfluidic devices for implementing cell cultures at the microscale[60,93,94], but this pumping methods has few disadvantages that must be taken into account. In particular, the maximum flow rates that can be achieved are limited by the reservoir capacities and a dynamic control of the flows requires to add or remove liquids from the reservoirs. For our geometrical design, a strategy to overcome these issues was to directly connect the liquid reservoirs with pressurized-air lines. Since no liquids were injected into the chip, the thermal equilibrium of the reservoirs with the chip was not compromised and dead volumes were not increased. Moreover, air-to-liquid interfaces were easily connected/disconnected without the risk of trapping air bubbles in the fluidic network. The graph in FIGURE 2.13 shows the average velocity measured in the MC as a function of the external pressure applied to LR_C. The first part of the curve ($\Delta P_D = 1.6 \cdot 10^3$ Pa) shows a linear trend compatible with a pure resistive behaviour. At steady state the pressure-driven flow is regulated by $q = \Delta P/R$, where q is the flow rate and ΔP is the pressure drop. Since q is proportional to the average

velocity (v) in the channel: $v/\Delta P = \alpha$, where α is the slope of the speed–pressure curve. The slope of the linear fit calculated for $1 \leqslant \Delta P \leqslant 1.6 \cdot 10^3$ Pa (red line in FIGURE 2.13) is $5.35 \cdot 10^{-2} \pm 0.74 \cdot 10^{-2}$ µm/s Pa, in agreement with simulations ($5.28 \cdot 10^{-2}$ µm/s Pa). For higher pressure values the average measured speed saturates. This behavior suggests the presence of pressure leaks that probably stemmed from a non-optimal sealing between the external tubing and the LRs.

2.4.3 Automated cell-loading

During typical operation, the whole chip (reservoirs included) was maintained within an incubator ($T = 37\,°C$, 5% CO_2) in thermal equilibrium with the external environment. In this condition, on-chip liquid reservoirs led to a reduction of dead volumes, efficient gaseous and thermal equilibration between the chip and the environment. This minimized the presence of temperature and gas–liquid solubility gradients along the liquid paths, resulting in negligible air bubble nucleation and microchannel clogging. Gas bubble formation is a very limiting factor in microfluidic devices and the published approaches to address this issue focused on removing bubbles already present in the chip by using dedicated elements such as hydrophobic paths to create gas–liquid interfaces on-chip[95], bypass channels to collect and drive air bubbles off-chip[96] or vacuum lines for gas removal[97,98]. However, the integration of bubble trappers increases device-manufacturing and operation complexity. Here, the prevention of gas bubbles nucleation in the microchannels was obtained using open liquid reservoirs, i. e. localizing the liquid-to-air interface on chip.

Cell loading was obtained by exploiting the difference in cross-sections between the FCs and the rest of the channels (TABLE 2.2). Since suspended cells typically have a circular cross-section with an average diameter greater than 10 µm, they cannot pass through the thin FCs ($2.5\,\mu m \cdot 10^1 \mu m$) which act as barriers, leading to cell accumulation at their ends. The loading procedure can therefore be divided into three phases:

1. $LR_{A,B}$ were emptied and LR_C was filled with the cell suspension, as schematized in FIGURE 2.14a;
2. flow was activated by gravity from LR_C down to the MC (FIGURE 2.14b), cells moved into the MC by viscous drag and progressively accumulated at FCs entrances (FIGURE 2.14c);
3. when all FCs were occluded by cells, the flow automatically stopped, thus preventing an excessive cell density to build up (FIGURE 2.14d).

Cells adhered and spread on the MC bottom layer in approximately 30 min, reopening FCs and therefore restoring liquid flow (FIGURE 2.14e). After cell spreading LR_A

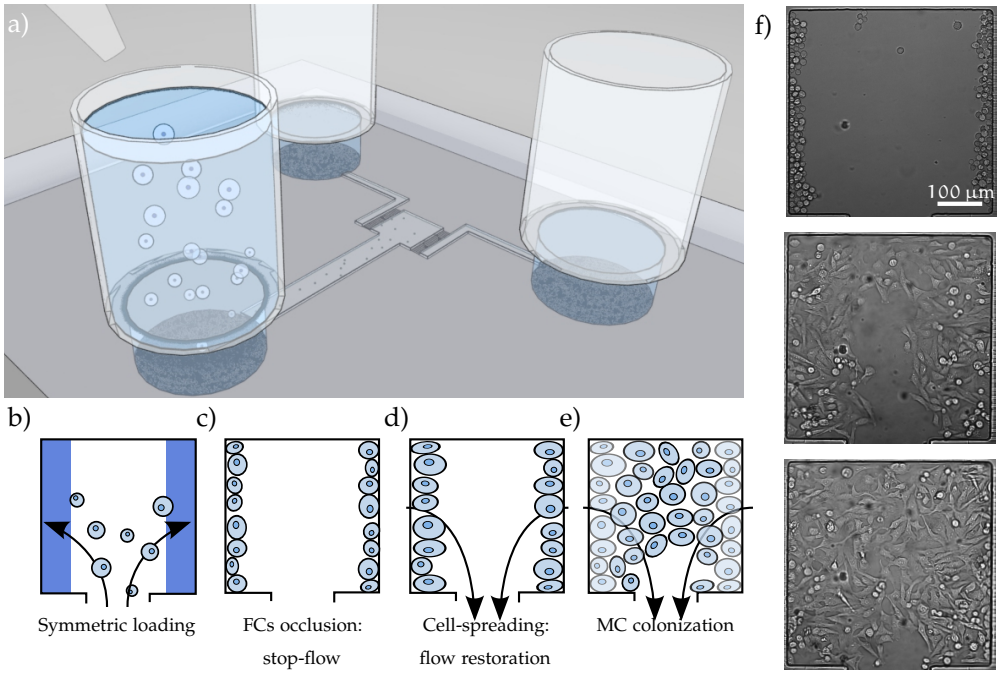

Figure 2.14: Automated cell-loading in closed microchamber. (a) Sketch of the chip during cell-loading. Cell suspension is added in LR_C while $LR_{A,B}$ are emptied. Cells, moved by viscous drag, start flowing inside the MC and are collected on the FCs (b), progressively occluding them until flow stops (c). Upon cell adhesion and spreading (i. e. in $\approx$ 30 min), FCs are freed and flow is restored. LR_C can be emptied and $LR_{A,B}$ can be filled with culture medium to achieve perfusion of the MC (d), monitoring cell-migration and MC-colonization (e). (f) Bright field imaging of MC-colonization by HeLa cells.

and LR_B were filled with standard cell culture medium in order to obtain flow inversion, i. e. fluids moved from $LR_{A,B}$ down to the MC and reached LR_C. The use of FCs allowed a reduction of cell-suspension density with respect to those typically required by standard loading methods[99–101]. Moreover, cells localized only in the active part of the device (i. e. the MC) thus avoiding possible chemical interactions with cell colonies developing in other parts of the microfluidic chip. This effect is known as *cellular valving* and was also implemented by other groups for single-cell positioning in microchannels[90,100]. Our chip yielded for the first time cellular valving as an automated process for cell loading and for controlling cell density in the culture area, operations that typically require pneumatic soft valves and complex chip geometries[6,89,102,103]. After cell-loading, liquid reservoirs were accessible to

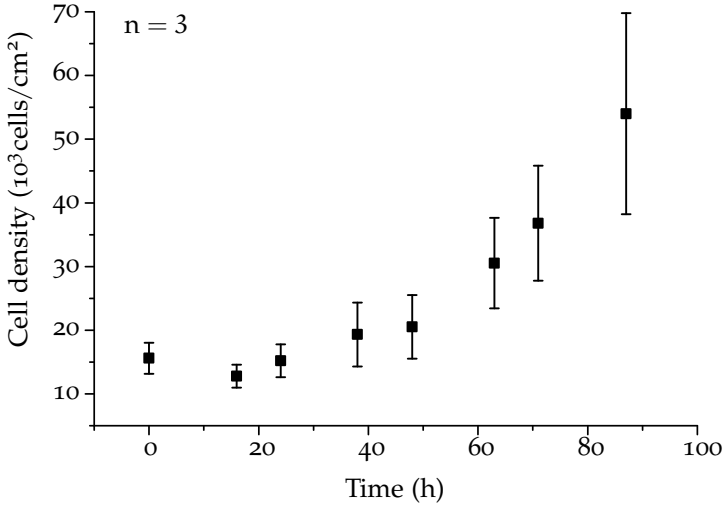

Figure 2.15: HeLa cells growth-curve during standard perfusion. Cells were loaded inside the MC and cultured under standard perfusion until confluence. Bright field images were acquired every 12 h to count cell number on every time-point. The measure was replicated 3 times and data are reported as mean±SD.

deliver substances (e. g. drugs, growth factors, etc.) into the MC via the FC. Details of the cell-loading procedure are reported in APPENDIX B.5.

FIGURE 2.14f shows a time-lapse describing the *standard symmetric loading* of HeLa, and the colonization of the MC under *standard perfusion* (see TABLE 2.3 on page 34). These images show that the colonization of the MC was characterized by a first phase where suspended cells adhered and spread, occupying the area close to the FCs and then started replicating, reaching confluence with a density of about $6 \cdot 10^{-4}$ cells/cm^2. This behavior was quantified and reported in FIGURE 2.15, where the number of cells is plotted vs. time during standard symmetric perfusion. An initial lag of 24 h preceded a regular growth curve, in agreement with what observed in similar conditions by other groups[94,104,105]. The cultures showed a growth rate of $0.023 \pm 0.002\,h^{-1}$ and a viability, calculated as the percentage of Calcein AM-positive cells, at 72 h of $88 \pm 3\%$ (see APPENDIX B.7 for details).

These values are in line with those measured in standard culture conditions by us ($0.028 \pm 0.007\,h^{-1}$) and by other groups (i. e. $0.025\,h^{-1}$ on average in multiwell plates[106]). They also are very similar to those measured in other published microfluidic devices under similar flow conditions[94,104]. The time required to reach confluence depends on the initial cell density and can be reduced using more concentrated cell-suspensions during the loading phase. In order to measure the doubling

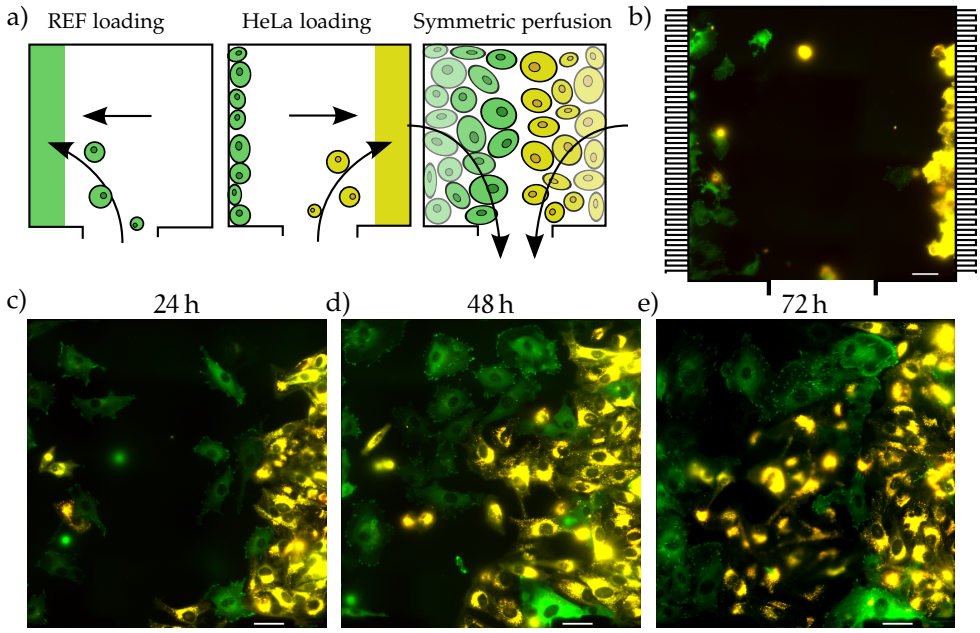

Figure 2.16: Asymmetric cell loading and co-culture. (a) Schematic loading protocol for co-culture experiments. (b–e) 72 h-time-lapse sequence of a REFs (green) and HeLa cells (yellow) co-culture. Scale-bars 50 µm.

time, the initial cell density was chosen to reach confluence in long terms (> 72 h), allowing a more accurate calculation of the growth rate. Cells did duplicate and showed a healthy morphology, demonstrating that the nutrients provided by the perfusion and the washout of the waste was sufficient for reaching and maintaining confluence. Finally, we also stress that shear-stress did not reduce cell viability and growth.

2.4.4 Tailoring co-cultures by serial asymmetric loading

The chip presented here can also easily obtain cell patterning or co-cultures inside the MC. To this end, an asymmetric cell loading protocol was described and demonstrated. The procedure is similar to the above described one except that the input pressures are set below the critical point calculated by EQUATION (2.25) (see APPENDIX B.5). This condition is satisfied by filling one of the opposite LRs and emptying the other. The resulting pressure configurations ($\Delta P_D = 75$ Pa, $\Delta P_S = \pm 150$ Pa) were called *standard asymmetric loadings*, as reported in TABLE 2.3 on page 34. Since

$P_C = P_i$ (with $i = A, B$), the liquid flowed towards LR_j ($P_j = 0$, with $j \neq i$) and the suspended cells collected on the corresponding FCs. The sign of ΔP_s determines the side of the MC at which the cells collected. The absolute value of ΔP_D is less than those used for symmetric loading (TABLE 2.3), resulting in a 50% reduction of the WLC flow rate and slower cell loading. Importantly, loading efficiency was not affected by this flow reduction. After cell adhesion and spreading fluid flow was restored, a second asymmetric loading could be performed towards the opposite side of the MC. This was obtained by simply inverting the sign of ΔP_s and could be applied to introduce a second, different cell population for co-culture experiments.

In order to demonstrate this operation mode, REF and HeLa cells were loaded into the MC and cell migration was followed by time-lapse fluorescence microscopy for 72 h. A schematics of the loading protocol is reported in FIGURE 2.16a. First, REFs, a cell line stably expressing paxillin-EGFP, were loaded into the left side of the MC and left to adhere for 1 h; second, HeLa cells stained with vybrant (Invitrogen), a vital fluorescent membrane dye, were sent to the other side of the MC (see TABLE 2.3 on page 34 for details about the pressure configurations in each working modality). After 1 h, standard perfusion mode was set and time-lapse acquisition started. FIGURE 2.16b–e show the two cell populations (REF in green and HeLa in yellow) migrating from the adhesion sites towards the central part of the MC. Migration was qualitatively different for the two cell kinds: while REFs colonized the free space from the adhesion side as single scattered cells, HeLa migration was mostly collective. Finally, after 72 h of culture, the spatial cell distribution developed in a mixed monolayer, in which small REF clusters were embedded into the HeLa sheet FIGURE 2.16d,e. At the end of the experiment both REF and HeLa did not show any visible evidence of necrosis or apoptosis.

2.4.5 Continuous perfusion in chemically-anisotropic environment

Owing to the characteristics of laminar flow, the gravity-driven operating mode could be successfully exploited to chemically decouple opposite sides of the MC, and to form chemical gradients whose spatial profiles are determined by ΔP_s and ΔP_D. We applied the present chip to the study of the anti-cancer properties of catechin-dextran conjugate. Catechin (CT) is a widely studied natural active ingredient found in many natural matrices, including green tea, and is widely recognized as co-adjuvant in cancer therapy[107,108]. CT conjugation with dextran (Dex) leads to improved CT stability while maintaining anti-cancer activity *in vitro*[109]. Cancer cells (HeLa) were loaded into the biochip and cultured to confluence under *standard symmetric perfusion* (TABLE 2.3 on page 34). CT-Dex was then delivered from one of the PCs. Symmetric perfusion was maintained for the whole experiment, leading

to the formation of a stable and symmetrical CT-Dex gradient within the MC. This gradient formation technique is similar to the one of the microfluidic jet device (μFJ) reported in[49], but this last device is based on open chambers so is not suitable for perfusion studies.

In order to better characterize the spatial distribution of drug concentration, a preliminary experiment was carried out with a fluorescently-labeled variant of the drug, obtained by substituting the CT with fluorescein with the same stoichiometric ratio. This substitution does not alter the diffusion properties of the compound, since fluorescein is very similar in weight and charge to CT (332.31 and 290.27 Da, respectively) and both of them are much smaller than the Dex (5 kDa). The dye (150 μg/mL in DMEM) was administrated from the left PC and DMEM from the right one. Figure 2.17a shows an epifluorescence image of the MC area where the bright and dark regions are associated with high and low concentration levels of labeled-Dex, respectively. Remarkably, $\Delta P_S = 0$ Pa led to the transition region being placed at the center of the MC and $\Delta P_D = 150$ Pa led to a very steep concentration gradient. Specifically, the spatial extent of the concentration gradient was limited to 75 μm, in very good agreement with the simulations (Figure 2.17b), demonstrating that the two sides of the MC were chemically decoupled.

Other devices, like the ones presented by Taylor et al.[93] and Peyrin et al.[110] were based on subcellular-sized channels for creating compartmentalised cultures that could be chemically isolated by hydrostatic pressure. However, this architecture is based on the physical separation of two culture chambers and allows neither for perfusion of the cell cultures, nor for chemical gradient generation. Instead, continuous perfusion devices such as the T-sensor[111] could exploit the slow diffusion typical of laminar flow to create chemical gradients at the meeting point of converging microchannels. Kunze et al.[101] proposed a device where the cells were cultured in two chambers separated by a connecting channel. A linear gradient was generated in this channel by loading two different solutions in the culture chambers, but the equilibration time of the reservoirs was limited to 75 min. Our chip combines the advantages provided by these two technologies in a versatile and easy-to-use tool for continuous perfusion bioreactors.

As previously mentioned, HeLa cells were loaded into the device and left to grow until confluence. Calcein AM was then administrated from both PCs to stain viable cells; then, CT-Dex (150 μg/mL in DMEM) was introduced from the left PC. The fluorescence signal was monitored by time-lapse microscopy for 5 h (figure 2.17c). Cells were not affected by CT-Dex during the first 2 h of treatment. Then intense blebbing affected the cells close to the CT-Dex administration area and fluorescence started to decrease, indicating progressive cell death. The wave of cell death propagated toward the center of the chamber, reducing the integrated Calcein AM fluorescence signal in the treated area down to below 10% after 260 min of treatment

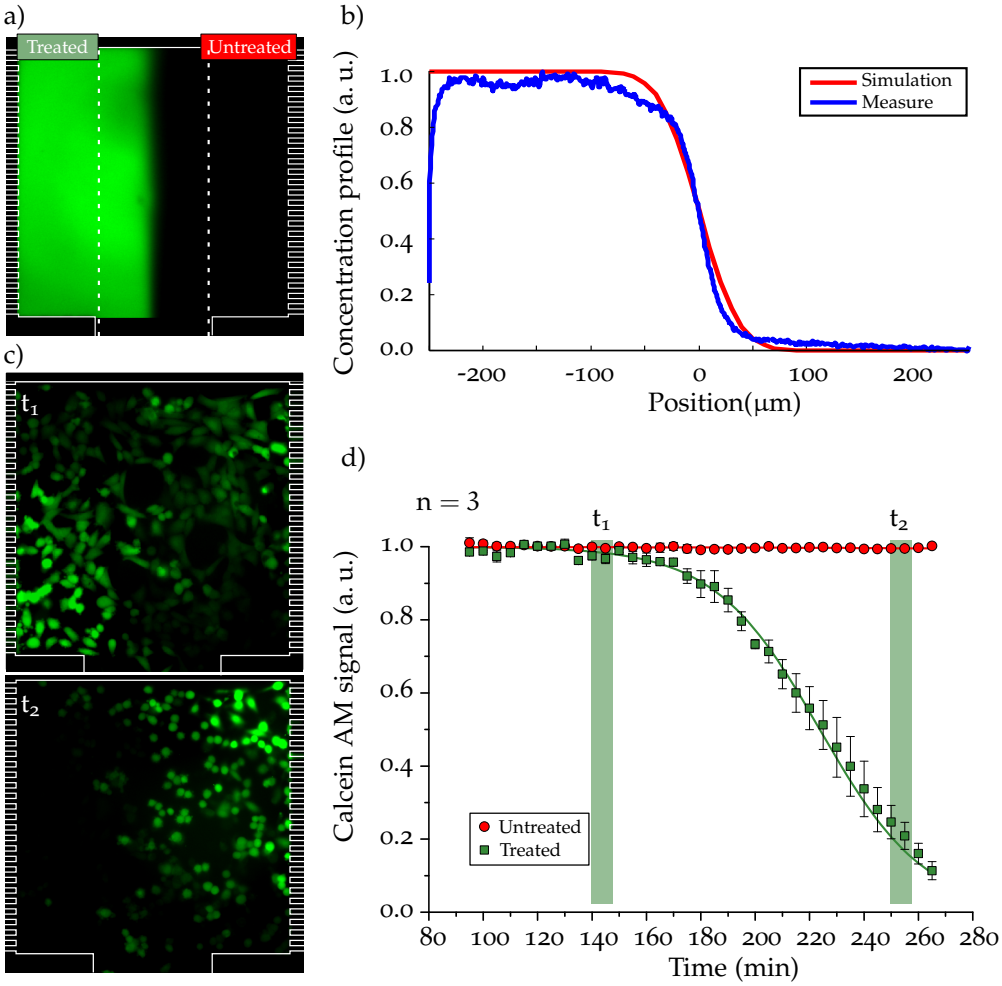

Figure 2.17: CT–Dex-induced cell-death. (a) Visualization of a stable fluorescein–Dex gradient in the MC (standard perfusion). Dashed lines identify two regions of the MC (treated and untreated) where the drug concentration is considered constant (high and low, respectively). (b) Comparison between theoretical and experimental gradient profiles. (c) Calcein AM fluorescence at different times during CT–Dex treatment. (d) Quantification of the Calcein AM signal during CT–Dex local administration measured by time-lapse fluorescence microscopy. Green and red curves are the normalized integral of the fluorescence signal in treated and untreated regions, respectively. The signal was normalized to take photobleaching into account. The measure was replicated 3 times and data are reported as mean±SD.

(FIGURE 2.17d). Conversely, non-treated cells (right side of the MC, FIGURE 2.17a) showed a stable Calcein AM signal throughout the experiment (FIGURE 2.17c), indicating that laminar flow was not significantly affected by the presence of the cells. Moreover, this demonstrates the efficacy of the drug anti-cancer activity, and that cell viability was not reduced by possible cross talk with the neighbor dying cells. To the best of our knowledge, this is the first example of a bio-chip where the dynamics of drug-induced death in cancer cells was studied. Previous reports present chips mainly based on cyclic voltammetry and commercial drugs such as etoposide, placlitaxel, hydroxyurea, cyclophosphamide, etc.[112–115] were used. In these papers, a good anticancer activity (reduction of the cell viability by 50%) was recorded only after 12 h (for etoposide and placlitaxel) or 24 h (for hydroxyurea and cyclophosphamide) incubation times. Our data report a reduction of cell viability to about 10% after only 260 min, indicating that CT-Dex can rapidly interact with and kill HeLa cancer cells.

2.4.6 Conclusions

Here, I presented a tubeless microfluidic device that is able to achieve long-term cell culturing and chemical-gradient shaping with no need of external pressure systems. This device exploits the careful dimensioning of the hydraulic resistances to achieve precise control over fluid dynamics in a closed MC and uses the pressure of liquid columns in open LRs as driving force. This approach requires no ancillary equipment for operation and therefore can be readily used in standard tissue culture laboratories. The open LRs also allow for a fast and efficient thermal and gaseous equilibration of the liquids with the chip, providing an efficient way to prevent gas bubble nucleation inside microchannels.

A self-limiting automated cell loading protocol exploiting sub-cell cross-section channels was successfully developed, leading to the fast and reproducible filling of the MC with cell suspensions. This protocol is based on the concept of cell valving and exploits a feedback-controlled loading that allows a correct handling of the device even by unskilled operators. Moreover, co-cultures with initial topographical organization were obtained by means of serial asymmetrical loadings, and the migration of two different cell types (i. e. HeLa and REFs) was monitored for 72 h by high-resolution fluorescence imaging.

Finally, I performed an assay to study the kinetics of an anti-cancer molecule, the CT-Dex conjugate, on HeLa cells. A rather fast action compared to data obtained with other commercial drugs (i. e. etoposide, placlitaxel, hydroxyurea and cyclophosphamide) was demonstrated. The fluidic concept described and demonstrated here is not limited to the present realization, but can be rather straightforwardly applied to other chip geometries and adapted to other biological studies.

3 BREAKING TOPOGRAPHICAL ISOTROPY

The translation of micro- and nanofabrication techniques to the field of tissue engineering generated great interest owing to the potential to recreate in vitro *some of the structural features of physiological systems. In this chapter I will first introduce the basis of cellular environmental sensing by describing the formation and maturation of the molecular complex named focal adhesion. Then, I will briefly review some of the micro- and nano-structured scaffolds currently used in tissue engineering and focus on a specific, directional geometry named nanograting. I will therefore present my results in exploiting hot embossing to pattern two polymers widely used in cell biology (i.e. PET and COC) with gratings of different periodicity. Finally, I will present the results obtained in culturing human mesenchimal stromal cells (hMSCs) and human umbilical-vein endothelial cells (hUVECs) on the nanostructured foils, detailing the effects of the gratings on cell-morphology and focal adhesion turnover.*

3.1 INTRODUCTION

3.1.1 Biological actors in mechanotransduction

In SECTION 1.2 I briefly introduced the molecular machinery responsible for the mechanical sensing of the extracellular environment. Since this topic has a key-role in understanding the cell-substrate interplay, it is worth reviewing it in more detail.

As previously stated, the interplay between the cell and the extracellular matrix (ECM) is mediated by molecular complexes named focal adhesions (FAs). These complexes have a double role, being involved both in anchoring the ECM and in regulating cytoskeletal organization. This is possible thanks to the intrinsically modular structure of FAs and their connection with the actin cytoskeleton by means of stress-fibers[12], as shown schematically in FIGURE 3.1.

The *receptor module* is formed by trans-membrane proteins which are able to anchor the cell to the ECM by binding specific ligands. Integrins are the most important

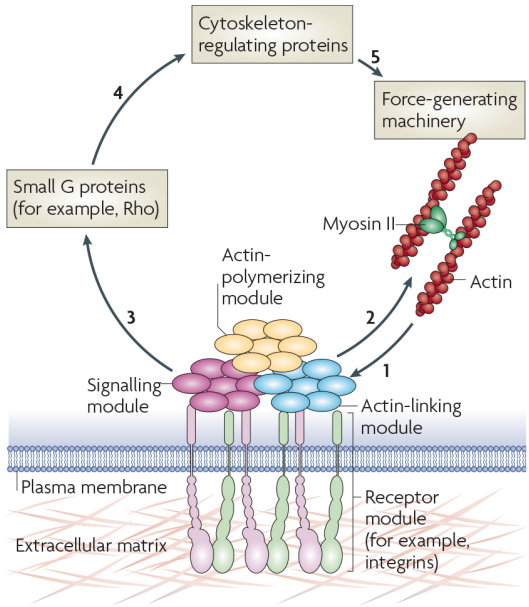

Figure 3.1: Structure and functional scheme of a focal adhesion. Forces that are generated by actin polymerization and myosin II-dependent contractility (step 1) affect specific mechanosensitive proteins in the actin-linking module, the receptor module (represented by integrins) and co-receptors, the associated actin-polymerizing module and the signalling module. Acting in concert, these interacting modules, with their particular mechanosensitive components, form a mechanoresponsive network. The effect on the actin cytoskeleton (step 2) depends on the integrated response of the entire system to interactions with the matrix and to applied mechanical forces. Stimulation of the signalling module eventually leads to the activation of guanine nucleotide-exchange factors and GTPase-activating proteins, leading to activation or inactivation of small G proteins, such as Rho and Rac (step 3). These G proteins affect actin polymerization and actomyosin contractility through cytoskeleton-regulating proteins (step 4), thus modulating the force-generating machinery (step 5). Image reproduced by [12], Rightslink licence number 3478100067553

and represented receptors of this family. Consequently to the binding with ECM, integrins undergo a conformational change, triggering the clustering of the proteins forming the intracellular complex. Detailing a complete list of the proteins involved in the formation of FAs is very complex [12] and falls beyond the purpose of this section. In the following, I will only concentrate on the main molecular actors required for the topographical sensing of the ECM.

The first proteins recruited on the adhesion site are talin and vinculin. Together, these proteins work as a mechanosensitive element, gathering integrins and providing a binding site for actin (*actin-linking module*) [12]. This step has a fundamental importance, since the survival of the early adhesion complex depends on the ability

to link the contractile elements of the cytoskeleton, i. e. the stress fibers (arrow 1 in FIGURE 3.1). The mechanical stimulation provided by stress fibers induces FAs to mature, elongating in the direction of the experienced force[116]. This process is autocatalytic, since the link to actin fibers is accompanied by enrichment in proteins promoting local actin polymerization (e. g. zyxin), resulting in a stronger coupling with stress fibers (*actin polymerizing module*, arrow 2 in FIGURE 3.1). The strengthening of the connection with the actin cytoskeleton is not the only feedback provided by FAs. Indeed, the inclusion of proteins such as paxillin and FAK allows for the triggering of a signalling cascade which involves the regulation of the whole cytoskeleton[12] by the regulation of guanine-nucleotide exchange factors (GEFs), which impacts on the Rho family GTPases[117] and, finally, to the contraction force exerted by the cell (*signalling module*, arrows 3–5 in FIGURE 3.1).

The presence of such a sophisticated sensing and regulatory mechanism suggests that the physiological environment contains signals and stimuli meant to instruct cells. This statement will be discussed in the following section.

3.1.2 Structural anisotropy in bio-matrices

The microscopic structure of living tissues is functional for their correct development and physiology[118,119]. Examples are widespread in the body, underlying the important link between role and shape. Particularly representative cases that should be mentioned are

- the organization of contractile and flow-resisting tissues, i. e. miocardium and endothelium;
- the migration of interneurons in the developing brain.

The first case regards tissues whose function requires a linear polarization. Indeed, all the cardiomyocytes in a single unit need to be aligned in order to yield for an efficient contraction, while endothelial cells (ECs), which organize in a tight sheet—extending in the axial direction of the blood vessel—polarize to better withstanding the shear-stress imposed by the blood flow. Both these tissues develop on fibrous ECMs composed of an ordered, directional mesh of sub-micron-sized collagen fibers[120,121], which directs the formation of polarized cellular layers.

The second example regards the formation of a much more complex and heterogeneous structure, i. e. the brain. Interneurons are a class of inhibitory neurons with a critical role in modulating synaptic activity[122], and an impairment in their functionality may result in neurodevelopmental disorders[123]. It is therefore important to notice that during embryonic development, interneurons arise from the ganglionic eminence and migrate into the developing cerebral wall in order to reach their final

location. As observed by Yokota et al., this process is guided by the presence of the ordered scaffold composed by the radial glia[124], which drives the interneurons by changing their migration pattern from tangential to radial, yielding for a correct development of the brain.

These examples underline that tissue engineering has to cooperate with micro- and nanofabrication technologies, since the quality of the tissues cultured *in vitro* relies on our ability to embed features of the physiologic environment inside artificial ECMs.

3.1.3 Artificial ECMs: a state-of-art

The technique able to produce scaffolds that most closely mimic the fibrous structure of ECMs is, without doubt, *electrospinning*. Exploiting the electrostatic force, electrospinning allows for the deposition of nanometric-sized fibers on a target collector[32]. This technology is compatible with a wide variety of bio-degradable polymers (e. g. collagen, PCL, etc.[32,34,125]) that can be loaded with soluble drugs—yielding for a passive and diffusive delivery—and arranged both in random or oriented meshes[126]. Even though these features allow for a good control of the bulk properties of the fibrous matrix, a fine positioning of the fibers at the micrometer-scale[127] is not within the capabilities of electrospinning. Moreover, the polymers used are usually not transparent[32], resulting in a poor compatibility with high resolution microscopy.

Important information about the cell-substrate interaction can be obtained by exploiting planar topographies realized on the surface of optically transparent materials (e. g. glass). 2D patterns are indeed very important for the optimization of biomedical devices such as stents or prostheses, since their performance is deeply influenced by the ability to prevent (for stents) or promote (for orthopedic prostheses) the integration with healthy tissues[128,129].

Remarkable results for surface modification were achieved by micro-contact printing[130], demonstrating that micrometer-sized adhesive islands can not only guide cell-shaping, but also interfere with the cell-survival mechanism[12,131]. These studies allowed for an analysis of the correlation between cell-morphology and the internal stress distribution[132], revealing the complex organization of the stress fibers and FA distribution in cells growing on adhesive fibronectin patterns. McBeath et al. demonstrated also that cell fate in human mesenchimal stromal cell (hMSC) can be directed by the induction a proper cell morphology, switching between adipogenic and osteogenic differentiation[133].

The control over cell-morphology can also be achieved without the chemical patterning of adhesion molecules, by exploiting micro-grooves and carved structures,

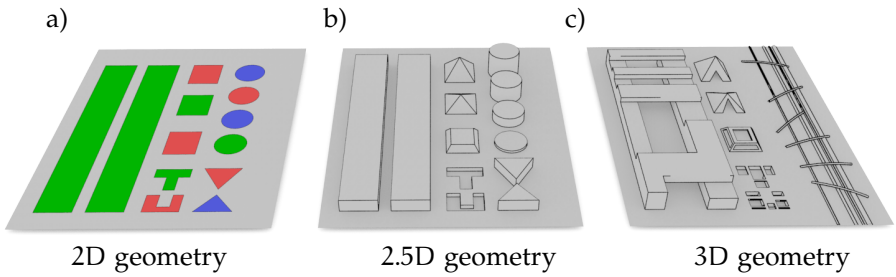

Figure 3.2: Topography dimensionality. (a) 2D topographies have no height and can be realized by printing motifs on the surface of the scaffold. (b) 2.5D topographies can have a height (or depth), but can still be considered as *textures*, since their height can be described using a 2D space (i. e. the height of the structure, $h(x, y)$). (c) 3D structures can present suspended elements and hollow structures that can be only described using three spatial coordinates.

e. g. gratings[134], pillars[135], pits[136], etc. These scaffolds are considered in-between 2D and 3D structures because even though they have a height/depth, they can be defined as a function of a bidimensional coordinate system, i. e. the surface of the scaffold (see FIGURE 3.2). For this reason, such topographies can be considered as surface-structures and addressed as 2.5D-architectures. Such structures can also be read by the cells, and therefore be used to deliver instructions to them. An attempt to understand the *topographical vocabulary* used by cells was done by Unadkata et al.[137], which implemented an algorithm-based approach to create a wide number ($> 2.1 \cdot 10^3$) of random topographies, and analyzed their impact on hMSC differentiation by means of high-throughput screening. Interestingly, the results obtained by Undakata confirmed that cell-fate is correlated with cell-area, and in particular more efficient osteogenic differentiation is obtained for cells with smaller area and increased major axis[137].

Even though the high-throughput screening of randomly-generated topographies may result in a detailed analysis of cell-substrate interaction, it is very onerous and only aims at the selection of a particular cell-phenotype, with only a marginal attention to the molecular processes linking the causes to the consequences.

Micro- & nano-gratings

Micro- and nanogratings (NGs) represent a class of rationally-designed, directional topographies. These structures are composed of an array of alternating ridges and grooves of varying width, periodicity and depth (w, Λ and d respectively, as sketched in FIGURE 3.3). Despite its simple design, this 2.5D topography has great potential for tissue culturing and regenerative medicine since its regular and anisotropic structure

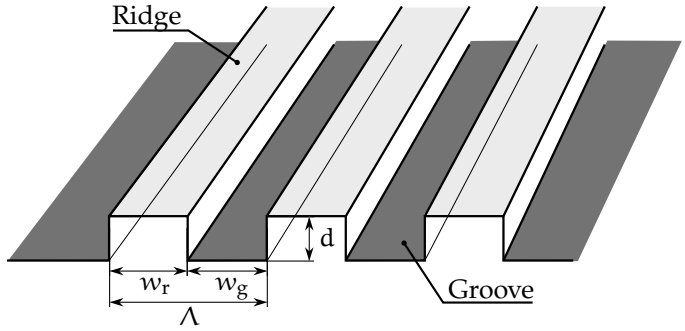

Figure 3.3: Structure of a nanograting. The schematics represents a grating, i. e. a structure composed by parallel ridges and grooves with depth d and width w.

recalls the features of ECMs found in linearly oriented tissues (see SECTION 3.1.2). Indeed, by exploiting the aspect ratio (AR) of the grating, defined as the ratio between depth and width of the ridges

$$AR = d/w_r, \tag{3.1}$$

and the stiffness of cell-membranes it is possible to prevent cells from reaching the narrow grooves carved on the surface of the scaffolds[138]. This means that adhesion will only be formed on top of the NG, and as a consequence FAs are constrained on the top of the ridges. The NG can therefore be used to select the orientation of FAs: since their shape is elliptical and oriented in the direction of the experienced traction force (see SECTION 3.1.1), a NG whose ridge-width is smaller than FA-major axis results in the collapse of the adhesion not aligned with the grating[134]. Finally, since the cytoskeletal traction is centripetal[139], this selection promotes a cell-phenotype characterized by an elongated morphology aligned with the NG and with FAs located at the opposite borders of cell body[120,140].

This last feature strongly influence cell-motility, since motion is determined by the anchoring and releasing of FAs, which pull the cell in the direction of the stronger adhesion[12]. If FAs are homogeneously distributed on cell-perimeter, any direction is available and migration results in a random walk. On the contrary, the polarization of cytoskeleton and FAs also biases the direction of endogenous contraction, making it directional[40] and faster[141].

In conclusion, the effects of scaffolds patterned with NGs on cells growing on them can be summarized as

- shaping of FAs by the collapse of misaligned ones;
- promotion of a bipolar morphology with stretched cytoskeleton;

Name	Periodicity (Λ)	Depth (d)	Aspect ratio (AR)
$\Lambda 1$	1 μm	350 nm	0.70
$\Lambda 2$	2 μm	350 nm	0.35
$\Lambda 4$	4 μm	350 nm	0.18

Table 3.1: Nanogratings with constant depth. The table reports the features of the gratings with geometry Λn.

- selection of a linear migration pattern aligned with the NG.

In the rest of this thesis I will focus on my results in realizing biocompatible micro- and nanostructured scaffolds to control cell morphology and migration patterns of different cell-types.

3.2 NANOGRATINGS: DESIGN & FABRICATION

Design

The NGs realized during my Ph. D. were designed according to the scheme in FIGURE 3.3 on the preceding page. All the gratings have a duty-cycle of 0.5, meaning that ridges and grooves have the same width. For this reason, in the following I will simply refer to *NG-linewidth* ($w \equiv w_r = w_g$). Each topography will be identified by its *periodicity* ($\Lambda = w_r + w_g = 2w$) and its AR and inserted in one of the following groups:

Λn NGs characterized by a nominal depth of 350 nm and a periodicity n (TABLE 3.1);

$\Lambda n_{1:1}$ NGs characterized by a nominal AR of 1 and a periodicity n (i. e. $w_r = d$, TABLE 3.2).

Fabrication

As previously stated, micro- and nanofrabrication techniques represent a powerful tool for the fabrication of artificial ECMs. The fabrication protocols, introduced and extensively used for electronic engineering applications[3], found several issues hindering their direct application for life science applications:

Name	Periodicity (Λ)	Depth (d)	Aspect ratio (AR)
$\Lambda 1_{1:1}$	1 µm	500 nm	1
$\Lambda 2_{1:1}$	2 µm	1 µm	1
$\Lambda 4_{1:1}$	4 µm	2 µm	1

Table 3.2: Nanogratings with constant aspect-ratio. The table reports the features of the gratings with geometry $\Lambda n_{1:1}$.

MATERIALS Standard lithographic techniques rely on thin UV- or electron-sensitive polymers (called *resists*) that can be impressed and developed, leaving a pattern that is transferred on the underlying substrate (in general silicon) by chemical or physical etching[142]. Unfortunately, the compatibility of such materials with cells and living tissues in general is not assured.

TIME High-precision techniques for creating sub-micron patterns usually are based on a serial workflow. An example is provided by electron beam lithography (EBL), which is able of realizing features of the order of tens of nanometers or less[143], by moving an electron-beam over a suitable resist, realizing a pattern at a time. On the other hand, the request made by biological applications of a great number of substrates with wide patterned areas conflicts with the rapid increase of exposure time requested by serial fabrication.

Thermal nanoimprinting

A way to overcome these issues is provided by hot embossing. This technique yields for the transfer of a pattern—down to the nanoscale—from a master to a thermoplastic replica. FIGURE 3.4a shows the scheme of the hot embossing process. First, a thermoplastic material is brought in contact with the mold and the temperature is raised above the glass transition temperature (T_g) of the thermoplastics, making it a viscous fluid. Then, pressure is applied to ease the polymer flow inside the features of the mold. Finally, the sample is cooled and pressure is removed, leaving the thermoplastics in a shape complementary to the one patterned in the mold.

This process is *fast*—an imprint cycle only requires few minutes—and *parallel*[144], because all the features on the mold are transferred simultaneously. As a consequence, the long fabrication times required for the creation of the nanopattern are only needed for the mold fabrication and have therefore a negligible impact on the overall process.

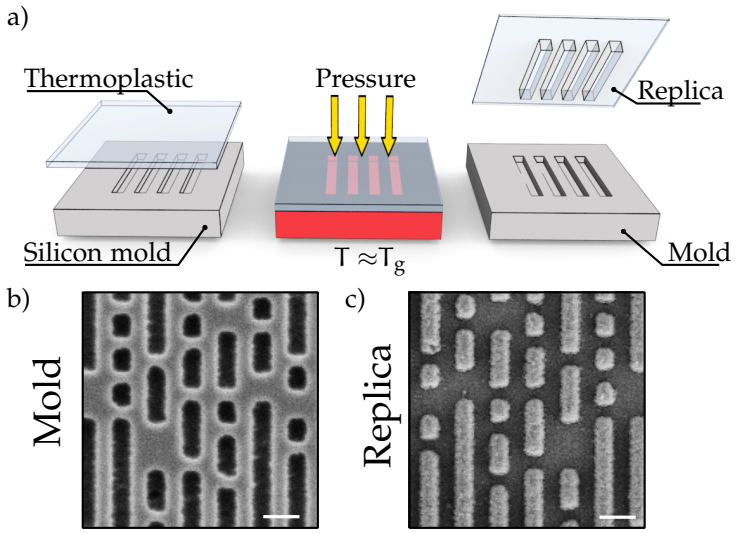

Figure 3.4: Thermal nanoimprinting. (a) Sketch of the hot embossing process. (b) SEM image of a nanostructured silicon mold. (c) SEM image of the COC replica of the nanopattern shown in (b). The patterns are complementary depth (reflected by the inverse grayscale map) and mirrored on the x axis. Scalebars 1 μm.

Materials & Replicas

Hot embossing is a very attractive technology also because many of the substrates customarily used in tissue culture are made by thermoplastic materials, e. g. poly-(styrene) (PS), poly (ethylene terephthalate) (PET), cyclic olefin copolymer (COC)[145]. During my Ph. D. I concentrated on two of these polymers:

PET is a material with a low glass transition temperature (T_g= 75 °C) and good biocompatibility. Indeed, it is approved by the United States food and drug administration (FDA), and it has been already successfully adopted for biomedical devices[146]. PET films are highly transparent, flexible and with high mechanical strength.

COC was already introduced in CHAPTER 2 as an optical support for high-resolution microscopy and cell culturing. This polymer is widely used for its high transparency, chemical stability and compatibility with injection molding[147] (T_g= 134 °C). COC is flexible, resistant and gas permeable, therefore suitable to be the sealing layer of closed culture environments, where gas exchange has to be preserved (e. g. bioreactors or leak-proof culture dishes).

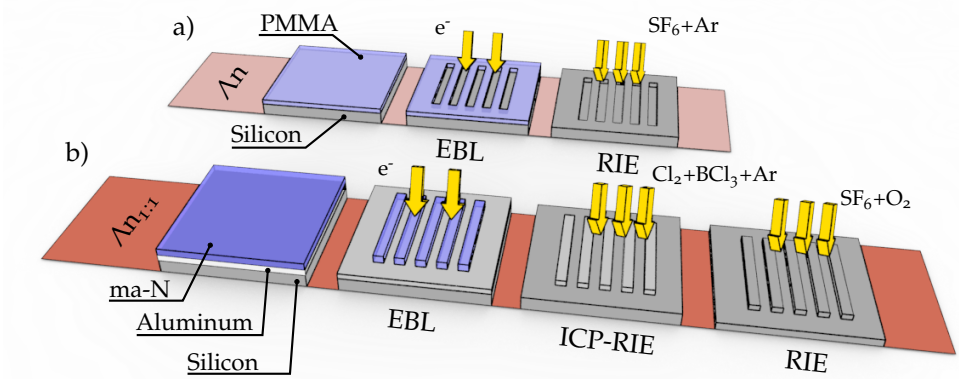

Figure 3.5: Mold fabrication protocols. The schematics represent the fabrication protocols used for the realization of Λn and $\Lambda n_{1:1}$ molds. (a) Λn molds were realized by using the pattern exposed on PMMA as etch mask during the RIE step (SF_6+Ar). This approach only requires two steps (i. e. EBL and RIE, but the etch of the polymeric mask limits the maximum depth that can be obtained. (b) $\Lambda n_{1:1}$ molds were realized by using a metal (Al) mask for the RIE step (SF_6+O_2). The Al mask was patterned by a combination of EBL and ICP-RIE (Cl_2+BCl_3+Ar).

The replicas were fabricated using an Obducat Nanoimprint 24 system (Obducat, Sweden), according with the protocols reported in APPENDIX A.5. The fidelity of the pattern transfer was verified by comparing the scanning electron microscope (SEM) images of master and replica, as shown in FIGURE 3.4b,c. Here, the mold is realized in silicon (gray areas in FIGURE 3.4b) where 500 nm-wide lines are carved (black areas). The lines are randomly interrupted, creating rectangular elements whose minimum size is $500 \times 500\,nm^2$ (this particular geometry will be discussed in detail in CHAPTER 4). The same patter, mirrored in the x direction, is found on the COC replica (FIGURE 3.4c). No appreciable differences can be found between the two geometries, demonstrating that the hot embossing process does not introduce shape-alterations in features of this size. Stylus profilometry (Bruker, Germany) also showed that nanostructure-depth is not significantly altered by the hot embossing process, since the average difference in depth between mold and replica was only of 3% for COC structures and 2% for PET ones.

Mold fabrication

Silicon molds were fabricated using standard nano-lithography: the NG was first impressed on a resist by means of electron beam lithography (EBL) and then transferred to the silicon by reactive ion etching (RIE).

Different fabrication protocols were used to produce the two designs described in SECTION 3.2, as sketched in FIGURE 3.5. The NGs with constant depth (Λn, see

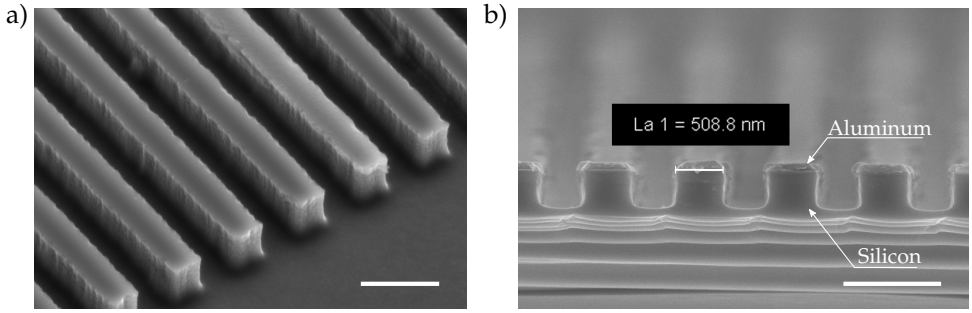

Figure 3.6: SEM imaging of silicon molds. (a) Tilted view of a $\Lambda 1_{1:1}$ mold. (b) Cross-section of a mold with the same topography. Residual Al mask is visible above the silicon grating. Scalebars 1 μm.

TABLE 3.1 on page 51) were fabricated using the PMMA pattern created by EBL as etching mask (SF_6+Ar plasma). This configuration minimizes the number of fabrication steps needed to create the mold, but could not be used to create high-aspect ratio structures, since the plasma used to etch the silicon also resulted in a fast etching of the polymeric mask. For this reason, the NGs with constant AR ($\Lambda n_{1:1}$, see TABLE 3.2 on page 52) were created by exploiting a metallic mask. To this aim, a 100 nm-thick aluminum (Al) layer was first evaporated on silicon and used as resist-underlayer during the EBL. Then, it was patterned by ICP-RIE (Cl_2+BCl_3+Ar plasma), using the resist as mask. Given the resistance of the Al mask, an SF_6+O_2 plasma could be used in the silicon etch step, resulting in gratings with well defined, vertical edges (see FIGURE 3.6). Details of the fabrication protocols are reported in APPENDIX A.4.

In order to increase the total patterned area I used ma-N 2403, a negative optical and e-beam resist with a low exposure dose if compared to PMMA—16.5 μC/cm² at 10 kV v.s. 320 μC/cm² at 30 kV for a $\Lambda 1$ NG. Thanks to this combination of parameters, it was possible to pattern a circular area with a diameter of 9 mm (i. e. 0.63 cm²) in a single overnight EBL (≈ 15 h), achieving an almost-complete covering of the culture area available in a standard 12 mm WillCo dish (WillCo Wells, Netherlands).

3.3 CELL SHAPING AND POLARIZATION

3.3.1 Nanostructured materials in orthopedics

In the field of orthopedics, many biomaterials are currently under investigation to develop surgically implantable devices for promoting enhanced osteogenesis. Promising results were achieved using composite scaffolds, in which mineral components

(e. g. hydroxyapatite[148] or tricalcium phosphates[149]) were embedded to promote bone regeneration in polymer matrices (e. g. PCL[150]). A recent study proposed to graft residues of bone morphogenetic proteins and adhesion peptides to PET surfaces to promote osteogenic differentiation and mineralization[151]; Saito et al. instead covered PET foils with TiO_2 to take advantage of the mechanical properties of the supporting PET and from the bone-bonding capability of TiO_2 [152].

To the best of our knowledge, physical modifications of PET, such as specific topographical features, were never introduced with the aim of enhancing osteointegration. Nevertheless, the morphology of mesenchymal stromal cells (MSCs) can determine their ability to proliferate and differentiate[133,137,153] and the local substrate micro- and nanotopography can drive cell shaping by mechanical stimulation[132,154,155]. For this reason, I fabricated PET-NGs with different geometries, and studied their interaction with human mesenchimal stromal cells (hMSCs), investigating their effect on cell-morphology, cytoskeleton architecture and also nuclear position.

3.3.2 Mesenchimal stromal cell interaction with PET gratings

In this study I used NGs with geometry $\Lambda 1$ and $\Lambda 2$ (see TABLE 3.1 on page 51) and a control surface, named FLAT . In order to represent a reliable control, FLAT samples were processed by the same hot embossing treatment used for the patterned substrates (see APPENDIX A.5.1 for additional details), using a polished silicon wafer as the mold.

Scaffold cytocompatibility

Cell adhesion was assessed by acquiring bright-field microscopy images of living cells after 30 min from seeding on each substrate and counting single attached cells per field. The number of cells on the NGs was normalized to the corresponding value measured for the FLAT. No differences were found, indicating that the presence of NGs does not modify hMSC adhesion. Cell viability was evaluated by triple labeling with Calcein AM, propidium iodide (PI) and Hoechst. Calcein AM and PI positive cells were considered as viable and necrotic cells, respectively; Hoechst allowed detecting pyknotic nuclei as marker for apoptotic cells (see APPENDIX B.7 for details). Experiments were performed after 24 and 72 h from seeding. Both $\Lambda 1$ and $\Lambda 2$ revealed no reduction in the percentage of viable cells with respect to the FLAT control; consistently, negligible necrosis and apoptosis were measured for all the tested substrates.

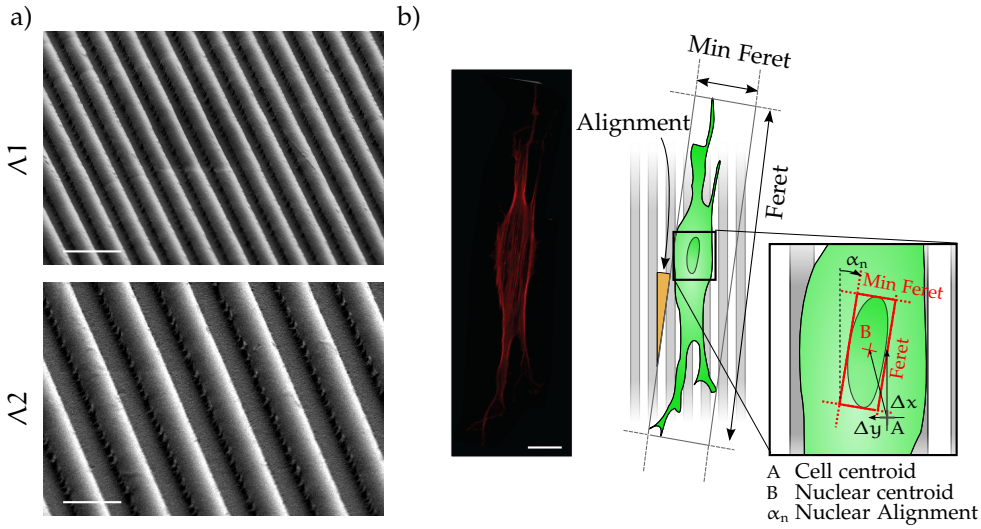

Figure 3.7: PET-NGs and hMSC morphological parameters. (a) SEM NGs with Λ1 (top) and Λ2 (bottom) geometry. Scalebars 2 μm. (b) Actin staining of an hMSC on Λ1 grating (left) and schematics of the morphometric analysis performed (right). Feret and min feret were calculated on the cell profile. Cell alignment was calculated as the angle between grating and feret directions. Nuclear morphology was calculated with a similar procedure, using nuclear profile. Scalebar 30 μm.

3.3.3 Cell morphology analysis

The effect of NGs on polarization and alignment of hMSCs was evaluated by measuring the following set of cell morphological parameters: feret, min-feret, area and alignment (FIGURE 3.7b, see also APPENDIX B.10 for additional details). Cell-feret showed a small increase only for Λ2, while for Λ1 the values remained unaltered with respect to FLAT (FIGURE 3.8a). Conversely, an evident reshaping resulted in a significant min-feret reduction that decreased, after 24 h from seeding, down to about the 50% for both Λ1 and Λ2 with respect to FLAT (FIGURE 3.8b). Cell area reduction was instead observed only for Λ1 (FIGURE 3.8c). These data indicate that NGs act on cell shaping by inhibiting the lateral expansion (reduction of min-feret and unmodified feret), and by selecting a polarized hMSC morphotype aligned to the NG.

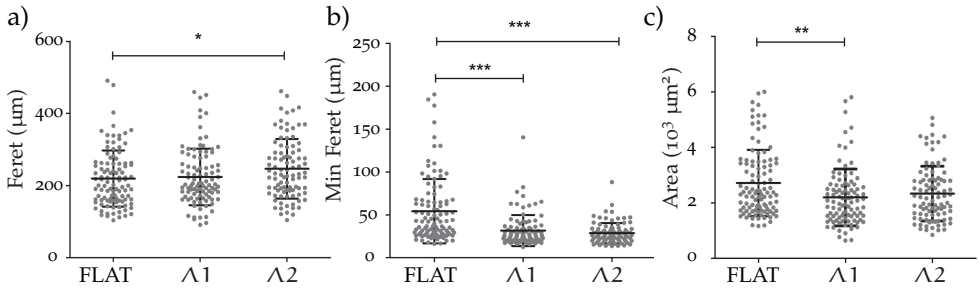

Figure 3.8: hMSC morphology on NGs. (a) Feret, (b) min feret and (c) cell area, measured for Λ1, Λ2 and FLAT substrates. Data were reported as single observations (dot) and mean±SD (black bars) and analyzed by non-parametric ANOVA Kruskal-Wallis and Dunn's Test ($n = 3$ independent experiments, 294 cells; *$P < 0.05$, **$P < 0.01$, ***$P < 0.001$).

Cytoskeletal organization and alignment to NGs

The topography-induced effects on intracellular organization were evaluated by staining for actin, tubulin and nuclei on cells fixed at 24 h from seeding on Λ1, Λ2 and FLAT.

Cytoskeletal directionality was calculated by means of bidimensional Fourier transform (FT) using the *directionality* function of ImageJ. This algorithm produces a histogram in which each bin represents the intensity of the spatial spectrum in a certain direction of the image. Two morphometric parameters can be extracted from this distribution: the first is the direction in which the cytoskeleton is oriented, which is identified by the maximum of the histogram. The *alignment* of the actin and tubulin fibers to the NG is therefore defined as the difference between this direction and the direction of the grating. The second parameter, hereafter named *dispersion*, represents the anisotropy of the cytoskeleton—which is maximum when all the fibers extend in the same direction and minimum when they are randomly distributed—reflected in the width of the distribution (see APPENDIX B.10 for additional details).

The graph in FIGURE 3.9a shows that the NG was able to align both the analyzed cytoskeletal components, i. e. actin microfliaments (red dots in FIGURE 3.9a) and tubulin (green dots), and that this alignment was coherent with the one of the whole cell body measured by the cell-feret (gray dots). A significant decrease was also measured in dispersion for both NGs with respect to FLAT (FIGURE 3.9b) indicating a tighter fiber arrangement. A similar trend was observed for the tubulin signal (FIGURE 3.9c), but no significance emerged.

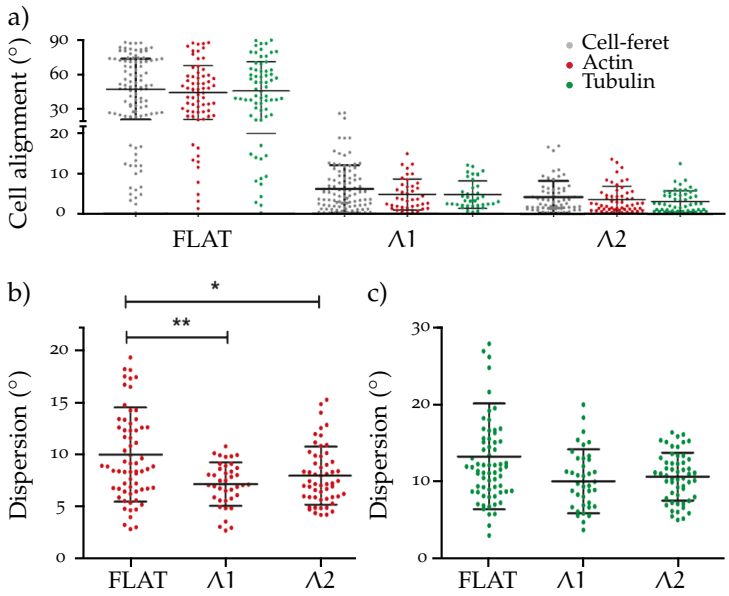

Figure 3.9: Chytoskeletal organization of hMSC on NGs. (a) Alignment of cell-bodies (gray dots), actin microfilaments (red dots) and microtubules (green dots). (b) Dispersion of actin and (c) microtubules. Data are represented as single observation (dot) and mean ± SD (black bars) and analyzed by non-parametric ANOVA Kruskal-Wallis and Dunn's Test ($n = 3$ independent experiments, 164 cells; *P $<$ 0.05, **P $<$ 0.01, ***P $<$ 0.001).

Nuclear morphology

Finally, the effect of NGs on nuclei was evaluated by measuring the nuclear morphology and displacement with respect to the cell centroid (see the schematics in FIGURE 3.7 on page 57b). The nuclei could effectively align to the NG pattern, probably as a result of the interaction with the polarized cytoskeleton[156–158] (FIGURE 3.10a). Concerning nuclear displacements, Δx and Δy were not significantly affected by the NGs (FIGURE 3.10b and c, respectively): only Δy significantly decreased for cells on $\Lambda 1$ with respect to those on FLAT.

Altogether, these data showed a limited effect of NGs on nuclear reshaping. Nevertheless, they revealed a good nuclear alignment to NGs that qualitatively correlated with the behavior of microtubules.

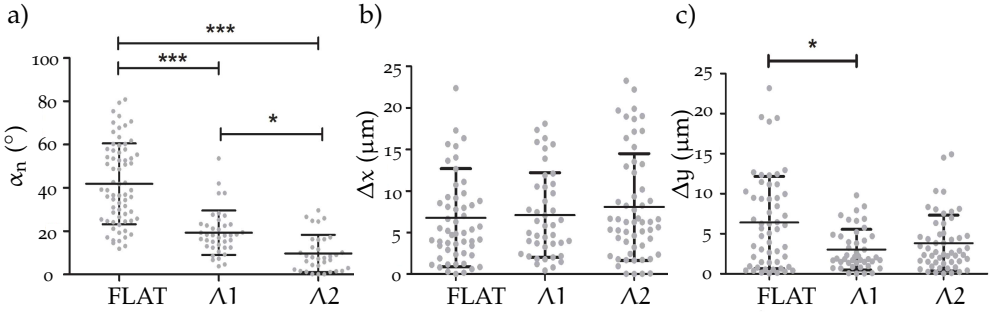

Figure 3.10: Nuclear morphology on NGs. (a) Nuclear alignment. (b) x and (c) y nuclear displacements from cell-centroid. Data are reported as single observations (dot) and mean ± SD (black bars) and analyzed by non-parametric ANOVA Kruskal-Wallis and Dunn's Test ($n = 3$ independent experiments, 164 cells; *$P < 0.05$, **$P < 0.01$, ***$P < 0.001$)

3.3.4 Conclusions

This study introduces PET-NGs as scaffolds for the stimulation of MSC mechanotransduction mechanisms. PET substrates were fabricated by hot embossing and did not require surface functionalization with adhesive molecules for cell adhesion and spreading, making these structures promising for rapid biomedical translation without the need of further chemical modification.

Cell and nuclear morphology, as well as cytoskeletal components were shown to be similarly affected by NGs, and that NG ridge sizes of 500 nm and 1 μm. Both geometries were effective in stimulating cell polarization, without compromising cell viability. In particular, polarization resulted from the inhibition of lateral cell expansion (reduction of min-feret and unmodified feret), and selection of a cell morphotype aligned to the NG lines. Alignment was similar for Λ1 and Λ2, in line with other studies exploiting other nanostructured materials[159,160]. Given that shaping into elongated morphologies was demonstrated to induce osteogenic differentiation[137,161], our results suggest that PET-NGs could be used in orthopedic applications to promote osteogenic induction.

3.4 SURFACE TOPOGRAPHY & FA–MOLECULAR TURNOVER

3.4.1 Endothelium and cell polarization

The endothelium lies at the blood-tissue interface of mammalian vessels. It regulates body homeostasis by controlling transport phenomena between the bloodstream

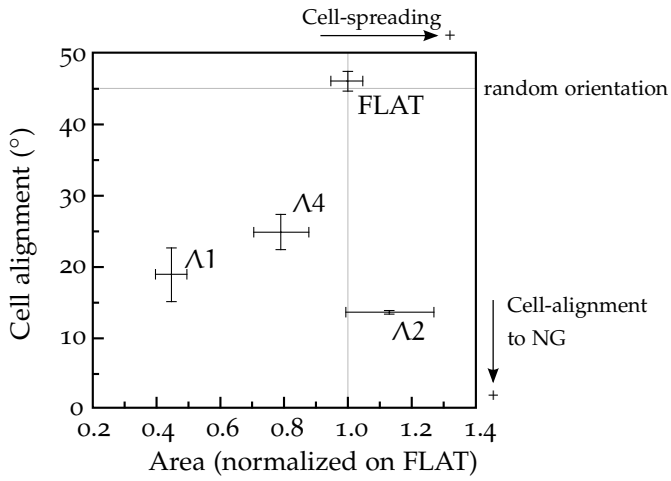

Figure 3.11: hUVEC morphology on patterned surfaces. The graph reports cell spreading (x-axis) and alignment (y-axis) to the different gratings tested. The bottom-right region of the graph corresponds to a high alignment to the grating and well spread morphology. Bars represent the of 3 independent experiments (mean±SEM).

and surrounding tissues, the exchange of gas and nutrients, and the movement of effector cells. A differentiated endothelium is composed of a confluent, growth-arrested monolayer of endothelial cell (EC) that polarizes in response to mechanical and chemical stimuli, and interacts with a topographically-structured ECM named basal matrix. The interaction between ECs and the basal matrix is critical to endothelium functions in physiological and pathological processes. By exploiting micro- and nano-engineered substrates it is possible to investigate the complex interaction between the basal matrix and the endothelium. While several specific applications of surface texturing were reported, a general understanding of the link between geometry of surface topography, FA maturation dynamics, cell-generated contractility and the resulting EC behavior is still missing. In this section, I will focus on how the lateral feature size of different gratings controls FA maturation dynamics.

3.4.2 Contact guidance on single endothelial cells

The biocompatibility of cyclic olefin copolymer (COC) substrates interacting with hUVEC is well established [40,138]. In order to evaluate the effect of the lateral feature size of anisotropic patterns, we used a set of gratings with periodicity varying in the interval $1-4\,\mu m$ and geometry Λn (see TABLE 3.1 on page 51). The groove depth

of 350 nm matches the average values reported in previous studies[40,138,162,163] to induce effective contact guidance on ECs.

Endothelial cell morphology

The scatter plot reported in FIGURE 3.11 shows the response of individual ECs to the underlying structure in terms of variation of cell-area (i. e. spreading) and cell-body orientation (i. e. alignment). The morphological analysis was conducted according to the criteria introduced in SECTION 3.3 and schematized in FIGURE 3.7 on page 57b (see APPENDIX B.10 for additional details).

Fully-spread ECs on FLAT substrates displayed random alignment, leading to an average orientation angle ($45.7 \pm 1.4\,^{\circ}$). Interaction with anisotropic patterns narrowed the orientation distribution, resulting in an average alignment angle of $18.6 \pm 3.8\,^{\circ}$ on $\Lambda 1$ gratings. Despite that result, spreading was significantly decreased for that geometry, reaching $44.6 \pm 5.0\%$ of the basal area of cells in the case of control (FLAT) substrates. A great increase of the lateral periodicity ($\Lambda 4$) led to a partial recovery of cell spreading, reaching a value of $78.7 \pm 8.6\%$ of the FLAT control, but also decreased the efficiency in terms of alignment to the grating ($24.6 \pm 2.5\,^{\circ}$). Interestingly, gratings with $\Lambda 2$ geometry proved ideal for both ECs spreading ($112.7 \pm 13.8\%$ of the FLAT control) and alignment ($13.3 \pm 0.3\,^{\circ}$).

3.4.3 Polarization of endothelial cell monolayers

After characterizing the effects of the gratings on single cells, we examined how anisotropic patterns affect ECs in growth-arrested endothelial monolayers. Here, cell polarity was revealed by the orientation of actin microfilaments and microtubules using the FT-analysis introduced in SECTION 3.3.3 (see APPENDIX B.10). In control endothelia grown on FLAT substrates, cells showed a uniform angular distribution of actin and tubulin filaments. Gratings were efficient in significantly reducing the alignment of filamentous actin to the grating, as shown in FIGURE 3.12a. The alignment of microtubules showed a similar behavior for all tested substrates, although the distributions were characterized higher variance (FIGURE 3.12b).

In summary, the cytoskeleton of ECs aligned along the underlying pattern, with actin microfilaments being better oriented than microtubules. Additionally, pattern $\Lambda 2$ outperformed the other tested geometries in inducing the re-modeling and re-orientation of cytoskeletal components.

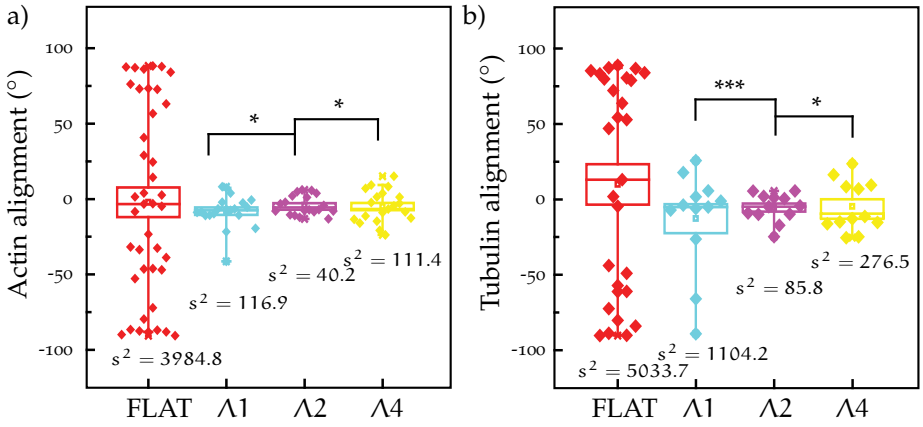

Figure 3.12: Cytoskeletal organization of hUVEC monolayers. FFT analysis of (a) actin and (b) tubulin cytoskeleton on hUVEC monolayers. Each point represents the cytoskeletal alignment on a single area of the hUVEC monolayer. Up to 15 areas were analyzed on a single sample (3 independent experiments were conducted). Boxes represent standard error of the mean and whiskers 5–95 percentile. Means were tested using homogeneity of variance and analyzed using Levene's test. *$P < 0.1$, ***$P < 0.001$

3.4.4 Focal adhesion stability in migrating cells

FAs act as sensors of substrate topography, and topographical features are known to interfere with the maturation and stability of FAs[140,164]. The resulting dynamics of FA assembly and disassembly is linked to several processes such as cell adhesion and migration[165,166]. A high FA turnover is prevalent in migrating cells whereas stable adhesion are generally detected in fully spread, non-migrating cells[167]. In order to test the hypothesis that gratings interfere with endothelial migration through a modulation of FA turnover, ECs were transfected with paxillin-GFP and monitored by time-lapse microscopy using a total internal reflection fluorescence (TIRF) microscope (see APPENDIX B.9). As previously established[140] fluorescently-labelled paxillin (see SECTION 3.1.1) correctly localizes to FAs and does not influence the migratory behavior.

The change of pixel-intensity during the time-lapse was used to monitor the paxillin-GFP at the cell-to-substrate interface (FIGURE 3.13a). The molecular activity was therefore estimated calculating the normalized standard deviation (SD) of each pixel during time (see APPENDIX B.11.1 for additional details)

$$\sigma(x,y) = \frac{SD_t(x,y)}{mean_t(x,y)}.$$

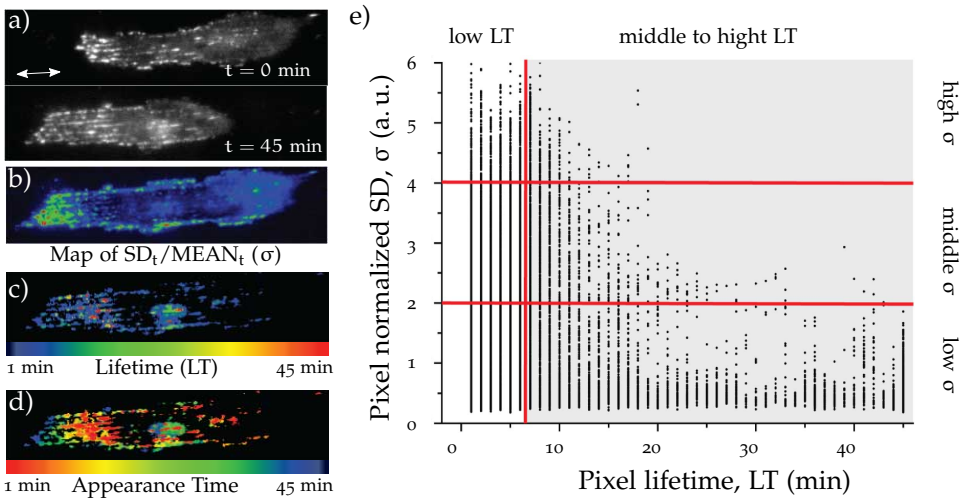

Figure 3.13: Focal adhesion dynamics on migrating hUVECs. (a) TIRF images of a hUVEC migrating on a $\Lambda 1$ grating (white arrow stands for grating's direction). FAs are visible as bright spots thanks to the fluorescent labeling of paxillin. (b) Map is used of pixel normalized standard deviation σ is used to calculate and lifetime LT (b) and appearance time AT (c). (d) Scatter-plot of the pixels in a TIRF time-lapse of a hUVEC cell migrating on a FLAT substrate. The pixels are grouped depending on their LT and σ values.

FIGURE 3.13b provides an example of a σ-map for an EC migrating on grating $\Lambda 1$. Data were filtered with a threshold in the σ-domain to remove the background signal and the pixels were grouped according to the amount of time and temporal point their signal was above the threshold. These two parameters were named pixel-lifetime (LT) and pixel-appearance time (AT), respectively. Color-maps of LT and AT relative to the cell in FIGURE 3.13b are reported in FIGURE 3.13c and d, respectively.

The molecular activity in FAs was evaluated by composing scatter-plot with the data of pixel-LT and σ. FIGURE 3.13e shows such a plot for a cell migrating on a FLAT substrate. Low-LT pixels were excluded to avoid possible noise originating from fluorescence fluctuations, and the resulting scatter-plots was subdivided into three categories corresponding to high, middle and low σ (gray area in FIGURE 3.13e).

FIGURE 3.14 shows the relative difference in the amount of pixels in each σ-category comparing $\Lambda 1$ and $\Lambda 2$ gratings with respect to the FLAT controls. Importantly, the fraction of high- and middle-SD pixels was strongly reduced in cells migrating on grating $\Lambda 1$ as compared to FLAT (reduction of $86.7 \pm 6.1\%$ and $68.7 \pm 4.7\%$, respectively), while no significant differences could be found for $\Lambda 2$ gratings. These data indicate that FAs formed by migrating ECs on $\Lambda 1$ gratings were characterized by

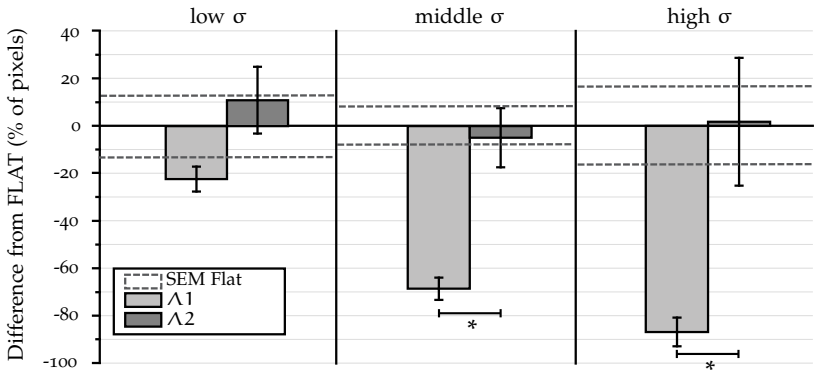

Figure 3.14: Focal adhesion life time. Quantification of graph FIGURE 3.13e. Relative difference in the amount of pixels in each σ-category. Deviations of Λ1 and Λ2 from FLAT are shown as mean±SEM of 15–21 time-series per condition. Mann-Whitney test was used to assess significance. *$P < 0.0001$

a slower turnover and an overall increased stability compared to ECs migrating on FLAT substrates or Λ2 gratings.

3.4.5 Conclusion

In this section I showed how the surface topography of a COC foil can be used to guide the formation of an ordered and polarized EC-monolayer. Three different geometries (namely Λ1, Λ2 and Λ4) were screened depending on the morphological alteration induced on individual cells and on confluent layers. Remarkably, Λ2 geometry was shown to be capable of aligning cells to the grating without impairing their spreading, providing an interesting tool for endothelial organization. A directionality analysis was performed evaluating the spectral properties of two major cytoskeletal elements (i. e. actin microfilaments and tubulin) for the different gratings used. Finally, TIRF microscopy was used to monitor the molecular turnover of paxillin in FAs, comparing the dynamics on Λ1 and Λ2 gratings with the one observed on standard FLAT substrates. I believe that these results can be valuable for regenerative medicine applications, since they could have the potential to improve the efficiency of rationally-designed, active surfaces at the interface with the blood stream.

4 DIRECTIONALITY MODULATION BY TOPOGRAPHICAL NOISE

Anisotropic geometries such as micro- and nanogratings represent an important tool to obtain cell contact guidance, however the regularity of their geometry can lead to several drawbacks. First, physiological systems are characterized by the coexistence of overall-ordered structures and local-disorder caused by stochastic alterations in tissue composition. These antithetical features reduce the biomimicry of artificial, regular geometries. Second, the design of implantable scaffolds must take into account the progressive loss of directionality due to the topographical deterioration—i. e. accumulation of bio-debris or the bio-degradation of the scaffold. In this chapter I will introduce a novel approach to modulate the intensity of the topographical, directional stimulus by the use of randomly-distributed nano-modifications. A Fourier transform algorithm for the quantitative calculation of directionality will be presented and a continuous spectrum of noisy topographies—spacing from nanogratings to a flat surfaces—will be tested on two biological models: neurite pathfinding of NGF-differentiated PC12 cells and directional migration of Wharton's jelly human mesenchymal stem cells.

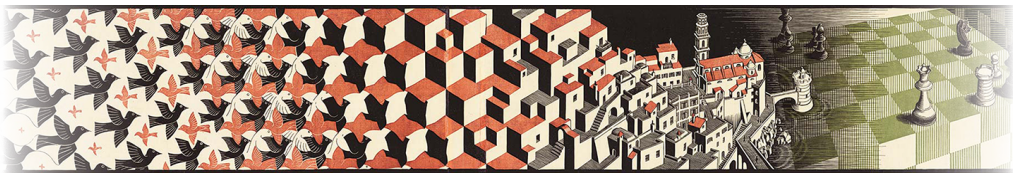

4.1 INTRODUCTION

In CHAPTER 3 I showed how highly anisotropic micro- an nanotopographies can be used to deliver a directional stimulus to cells. In all the reported experiments, the intensity of the directional signal was fixed and triggered only by the presence of the topography, thus leading to simple on/off topographical activation. This limitation hinders the possibility to investigate the cell response to partial anisotropy, a condition typically found in organs and tissues, where directional signals are usually covered by biotopographical noise, e. g. rests of apoptotic cells, sclerotic plaques[168], alterations of ECM-proteins or of their proteolysis[169], differences in collagen fiber banding[170], formation of gaps and/or neuroma after nerve injury[171], and degradation of implantable prostheses[172].

Few studies investigated cellular response to nano-topographical disorder, focusing on non-directional geometries. In particular, Huang et al. obtained important information on integrin clustering using ordered and disordered adhesion-molecule motifs, demonstrating that disorder can improve cell-adhesion for low ligand-densities[173]. Dalby et al. also showed that the introduction of topographical disorder in a lattice of nano-holes stimulates hMSCs to produce bone mineral also in the absence of osteogenic supplements—low or negligible mineralization occurred on ordered patterns[174,175] However, cellular response to partially distorted directional topographies remained uninvestigated.

In this chapter I will define a novel category of anisotropic nanotopographies characterized by the possibility to modulate the intensity of directional stimulus by the addiction of topographical noise. First, I will describe the design and fabrication, proposing a general FT-based method for the quantification of substrate anisotropy. Then I will describe the effects of such devices on neurite pathfinding, using NGF-differentiated PC12, and on polarization of migration patterns, using Wharton's jelly human mesenchymal stem cells (WJ-hMSC).

4.2 NOISY NANOGRATINGS: DESIGN AND FABRICATION

4.2.1 Design

A general strategy for the creation of partially-ordered topographies is described by this simple work-flow:

1. selection of a master geometry with the highest directionality and definition of *topographical sub-units*;
2. definition of *regular* and *modified* sub-units;
3. alteration of the master geometry by the insertion of modified topographical sub-units.

1. Master geometry and sub-units

As a master geometry I chose the $\Lambda 1$ grating (1 μm-period, 350 nm-depth, see TABLE 3.1 on page 51). This choice is based on our previous studies, showing that this geometry can induce cell-elongation and polarization of cell migration patterns along the grating lines[140,164,176]. The grating was divided in two kinds of sub-units: *ridge-units* (marked with the number 1 in FIGURE 4.1a) defined as $500 \times 500 \times 350\,\text{nm}^3$ blocks, and *groove-units* (marked with a 0) defined as empty spaces with the same

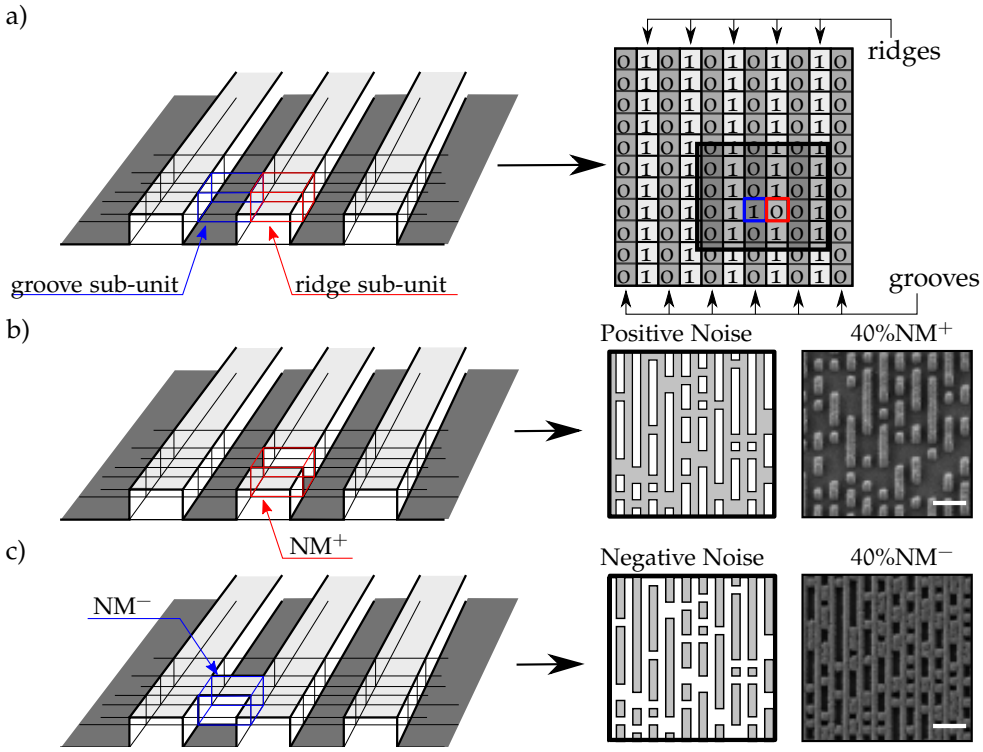

Figure 4.1: Nanomodifications on nanogratings. (a) Sketch of a grating and identification of the two topographical sub-units, groove (blue) and ridge (red). On the left side, the matrix-visualization of the grating used by the pattern-generation software. Ridges identified by a 1 and grooves by a 0. NMs result in a change of the distinguishing number associated to the sub-unit. Positive (b) and negative (c) NMs are sketched (left column) and shown by means of SEM imaging (right column).

size (see FIGURE 4.1). Given this definition, an ideal grating can be mapped on a 2D matrix where even and odd columns are 1 and 0, respectively.

2. Nano-modifications

Nano-modifications (NMs) were inserted in the master geometry by changing a ridge-unit into a groove-unit or vice-versa. Two types of modification were defined in this studies. The first, named positive nano-modification (NM^+), is characterized by the presence of a groove-unit along the ridges, resulting in a reduction of the total area available for cell-adhesion (FIGURE 4.1b) while a negative nano-modification (NM^-) is the result of a ridge-unit bridging adjacent ridges (FIGURE 4.1c).

As previously demonstrated[134,138], NGs interfere with the formation and maturation of FAs, confining them on top of the ridges and forcing their maturation along the grating. The presence of nano-modifications interferes with FA-maturation, introducing gaps that can block the growth of aligned adhesions (NM^+) or bridges allowing misaligned ones (NM^-).

3. Noisy topographies

The density of randomly distributed nano-modifications in a master geometry was used to modulate its directionality. A DXF file (AutoCAD, Autodesk, USA) containing the final design of the noisy topography was produced by a custom-made Matlab script (MathWorks, USA) and used to fabricate silicon molds for hot embossing as reported in SECTION 3.2 and APPENDIX A.4.1.

Each pattern was described by two parameters: the type of nano-modification used (i. e. positive or negative) and the probability p of a modification-event (i. e. the insertion of a nano-modification). FIGURE 4.1b and c show a sketch of the two noise-types and an SEM image of COC gratings with $p = 40\%$ (i. e. $40\%NM^+$ and $40\%NM^-$, respectively).

This process is very versatile, since the Matlab script works in a parametric way, allowing for an easy variation of the final geometry in terms of grating-periodicity Λ, relative size of the ridge- and groove-units or total patterned area. Moreover, adding the nano-modifications during the design of the topography leads to the creation of map scaffolds, allowing for easy evaluation of the spectral properties of the structure and making it possible to replicate the same geometry indefinitely, yielding for high reproducibility during the cell-topography interaction experiments.

4.2.2 Substrate directionality quantification

The nano-modification-probability p is a good indicator of the overall topographical disorder, but it is not suitable for a quantitative measure of directional stimulus associated to a certain region of the pattern. To this aim, a specific parameter named *directionality* (δ) was defined to provide better insight into the intensity of the directional signal delivered to the cells. In the following, a general definition of δ will be given by introducing a general method for its quantitative calculation.

The directionality of a noisy NG can be seen as the combination of the directional and periodic stimulus provided by the NG and the randomly distributed nano-modifications. The relative weight of these two components can be easily visualized and quantitatively evaluated by means of the FT of a given nanopattern. δ was defined

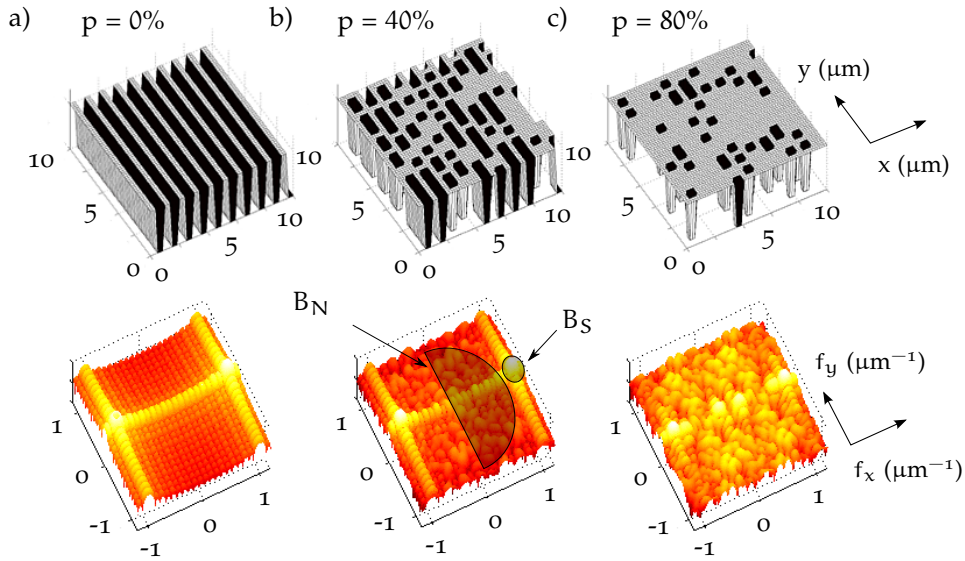

Figure 4.2: Directionality quantification. Model of a $10\,\mu m \times 10\,\mu m$ area of a nanotopography (top row) and representation in the spatial frequency domain (bottom row) for increasing density NM^{-}. The amplitude spectra are characterized by a main peak corresponding to the spatial frequency of the $\Lambda 1$ grating ($\Lambda = 1\ \mu m^{-1}$) and by low-frequency noise ($\Lambda < 1\ \mu m^{-1}$). Signal band (B_S) and noise band (B_N) are represented on the (b) spectrum.

as the averaged ratio between the signal of to the periodic component and the low-frequency noise:

$$\delta(p, A) = \left\langle \frac{\frac{1}{B_S}\iint_{B_S} \left|FT_{p,A}(f_x, f_y)\right| df_x df_y}{\frac{1}{B_N}\iint_{B_N} \left|FT_{p,A}(f_x, f_y)\right| df_x df_y} \right\rangle, \tag{4.1}$$

where $FT(f_x, f_y)$ is the bidimentional FT of the pattern, B_N and B_S are the noise and signal bands, respectively (see FIGURE 4.2), and A is the nanopatterned area used for the FT calculation. Ten patterns were averaged for each $\delta(p, A)$. The central frequency and width of these bands depend on the periodicity of the master geometry and the type of nano-modification used (see APPENDIX B.4 for additional details).

The effect of NM^{-} on the power spectrum of a $10 \times 10\,\mu m^2$ NG is shown in FIGURE 4.2. For $p = 0\%$ (FIGURE 4.2a), the spectrum is dominated by the two peaks at $f_y = 0\,\mu m^{-1}, f_x = \pm 1\,\mu m^{-1}$, reflecting the periodicity of the $\Lambda 1$ grating used as

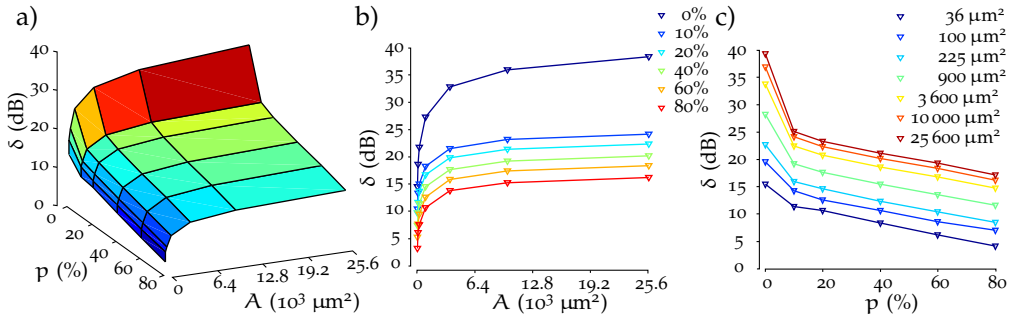

Figure 4.3: Quantification of substrate directionality. (a) 3D plot of substrate directionality $\delta(p, A)$ as a function of grating area (A) and nano-modification probability (p). (b) Substrate directionality as a function of the grating area $\delta(A)$, for several values of p. (c) Substrate directionality as a function of nano-modification probability $\delta(p)$, for several values of A. Curves calculated for NM^-.

master geometry. As p increases (FIGURE 4.2b and c), nano-modifications increasingly impact the overall NG organization and reduce the intensity of the peaks in the FT domain. The spectra in FIGURE 4.2 show how randomly distributed local distortions result in the appearance of low frequency components in the FT domain.

The images were generated by introducing a random variation in the value of each pixel, mimicking the impact of surface roughness on the topography. Roughness was modeled as noise with a flat probability density and a 6 nm amplitude. Including surface roughness in the computation of δ allowed for the calculation of a directionality value for $p = 100\%$ (i. e. FLAT substrates), which would otherwise have a null spectrum, introducing a singularity in EQUATION (4.1).

Directionality dependence on pattern area and noise density

FIGURE 4.3 shows the calculation of δ for $0\% < p < 100\%$ and $6 \times 6\,\mu m^2 < A < 160 \times 160\,\mu m^2$. As expected δ has monotonic behavior, increasing with A (FIGURE 4.3b) and decreasing with p (FIGURE 4.3c). A strong decrease of $\delta(A)$ is visible for $A < 20 \times 20\,\mu m^2$ for all the values of p. This effect can be explained by considering that a reduction of A results in a smaller number of periods available for the spectral reconstruction of the master geometry, with a reduction of the intensity in the signal band.

A systematic characterization of the dependence of δ from p and A is very important to determine the actual signal delivered to cells, since topographical sensing is limited to cell-adhesion area. Typically values of cell-area span in the interval 100–3 000 μm^2 [138,176,177]. For this reason, a single substrate may result in different directionality depending on cell type.

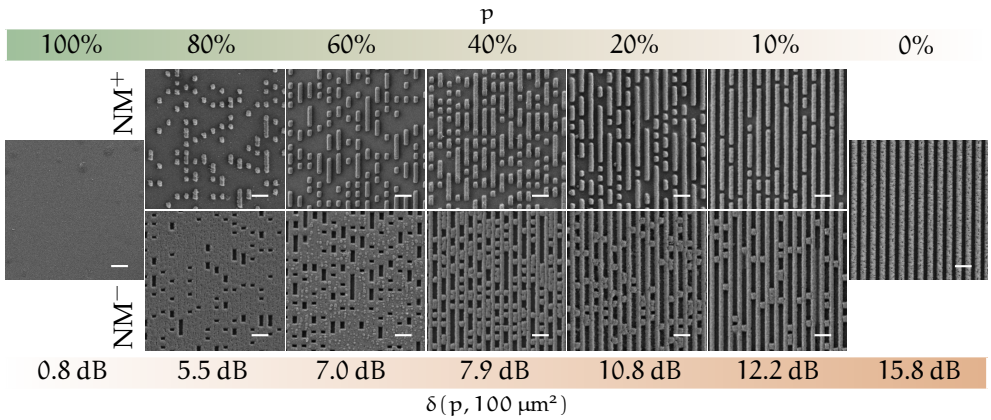

Figure 4.4: Set of noisy nanogratings. SEM images of COC nanotopographies are reported. The structures are sorted for increasing directionality. The lower bar reports δ values calculated for $A = 10 \times 10\ \mu m^2$. Scalebars 2 μm.

4.2.3 Fabrication

Two sets of 6 molds with p varying from 0 to 100% (NM^+ and NM^-) were fabricated according the protocol described in the SECTION 3.2 and APPENDIX A.4.1. The patterns were replicated on COC, and the effect of noise on substrate wettability was assayed by static contact angle measurements[178]. Indeed, surface energy—and, in particular, water wettability—are known to affect the cell–substrate interaction and modulate cell adhesion, spreading and proliferation[179,180]. The average contact angle on the whole set of topographies was $87 \pm 7\,°$, with no evident dependence on p. No statistically significant difference ($P > 0.05$, One-Way ANOVA, Tukey multiple comparison test) could be found between the whole set of imprinted substrates. However, all samples showed a reduced hydrophilicity when compared to unimprinted COC foils ($79 \pm 7\,°$). The imprinting process therefore modified the COC surface wettability, but this effect did not depend on the imprinted nanotopography. Thus, the introduction of noise did not lead to artifacts in the cell response owing to the altered surface wettability.

4.2.4 Conclusions

In this section I described the design of original noisy topographies with controlled directionality. The patterns were realized from $\Lambda 1$ gratings, and substrate directionality was modulated by the addition of a controlled density of point-like nano-mod-

ifications. Two types of topographical noise, called positive and negative noise, were realized by the insertion of gaps along the ridges of the grating, or bridges between adjacent ones, respectively. A general quantitative definition of directionality was proposed, discussed and applied to our nanostructures. Finally, the topographies were transferred onto transparent COC foils by hot embossing.

4.3 NEURONAL PATHFINDING ON NOISY NANOSTRUCTURES

The mammalian nervous system is an example of highly polarized tissues[181]. Neurons are cells specialized in connecting biological units (e. g. neuron-neuron, neuron-myocytes, sensory neuron-neuron) allowing for directional propagation of information within the body. Examples can be found in the complex neuronal networks in the central nervous system or in the long-extending neurons of the peripheral nervous system. This connectivity relies on the formation of cell-protrusions named *neurites*, which act as cables, allowing the propagation of electrical signals. In order to find their target, neurites are able to detect and follow molecular gradients, e. g. paracrine secretions, and mechanical stimuli, e. g. the physical structure of the ECM[1]. Correct wiring has crucial importance for the functionality of neuronal networks, and deficiencies in this process can lead to severe neurological disorders[118] such as schizophrenia[119].

PC12 cells are a cell line often used as an *in vitro* model for neuronal differentiation[182,183]. They respond to several growth factors, neurotrophins, and hormones and can be used to assess distinct responses during differentiation[184]. When stimulated, PC12 cells recapitulate several steps of neuronal differentiation as they block proliferation and extend multiple neurites. Nerve growth factor (NGF) is the classical inducer of neuronal differentiation[182]. We previously showed that the interaction of differentiating PC12 cells with NGs with $\Lambda 1$ gratings results in neurite selective consolidation, leading to a highly specific neuronal cell morphotype, characterized by bipolarity and neurite alignment to the NG lines. In the following I am going to report the use of PC12 cells to investigate neurite contact guidance on noisy topographies.

4.3.1 Cell viability

Cell adhesion and viability studies were carried out to assess the biocompatibility of noisy NGs. Cells were seeded on the substrates and allowed to adhere and grow

up to 24 h under standard cell-culture conditions (see APPENDIX B.6.5). No significant difference in adherent viable cells (Calcein AM^+) was found between the noisy substrates and FLAT substrates[178] ($P > 0.05$, One-WayANOVA, Dunnett multiple comparison test). A single difference ($P < 0.001$, One-WayA NOVA, Dunnett multiple comparison tests) was found within the nanostructured substrates, between the $\Lambda 1$ grating and the 80%NM^+. This condition corresponds to substrates with scattered post-like nanostructures, whereas the majority of the area is flat (FIGURE 4.4). Cells contacting the surface must then locally adapt and stretch their membrane for effective spreading, a condition that can slow-down or prevent cell adhesion[185,186]. Overall, PC12 adhesion and growth were shown to be comparable with standard, unpatterned substrates.

Cell viability was then correlated with cell death level, which can be estimated as the percentage of necrotic cells (PI^+ cells) over the total cell number. The cell death level was similar for all the tested substrates ($P > 0.05$, One-Way ANOVA), and it is comparable to that of the flat control[178]. Specifically, after 24 h, the measured percentage of dead cells was lower than 2% for all nanotopographical noise sets, in agreement with the value found in standard culture conditions.

4.3.2 Neurite alignment

PC12 neuronal differentiation was induced by NGF administration (100 ng/ml). Neurite length was then measured and interpreted as a marker of cell-differentiation efficiency. No significant difference in neurite extension between the different noisy topographies and the flat surface was found ($P > 0.05$, One-Way ANOVA, Tukey multiple comparison test)[178]. No specific trends could be correlated with δ, suggesting that neither NGs nor nano-modifications affect or inhibit neurite cell growth. In particular, the average *neurite length* ℓ (see APPENDIX B.10.1) was found to be $28 \pm 2\,\mu m$, $37 \pm 2\,\mu m$ and $35 \pm 2\,\mu m$ (mean $\pm$ SEM) at 24, 48 and 72 h, respectively, in agreement with what is reported in the literature for standard culturing conditions[140,164,187] .

Neurite alignment α_n was defined as the average angle between neurites and NG direction (FIGURE 4.5a and APPENDIX B.10.1). As expected, neurites interacting with control NGs ($\delta = 15.8$ dB) aligned to the grating ($\alpha_n = 4.3 \pm 1.1\,^\circ$ at 72 h, mean $\pm$ SD). The progressive addition of nano-modifications—i. e. the decrease of δ—was reflected by a loss of neurite alignment, down to the value measured on isotropic, FLAT substrates ($\delta = 0.8$ dB, $\alpha_n = 43.6 \pm 4.1\,^\circ$ at 72 h). The resulting curves showed a sigmoidal trend, as reported in FIGURE 4.5b for NM^+ (green) and NM^- (red) at 72 h. It was therefore possible to define a threshold value as the δ at which α_n is 50% of the maximum misalignment. This value will be named δ_{50} (see FIGURE 4.5b).

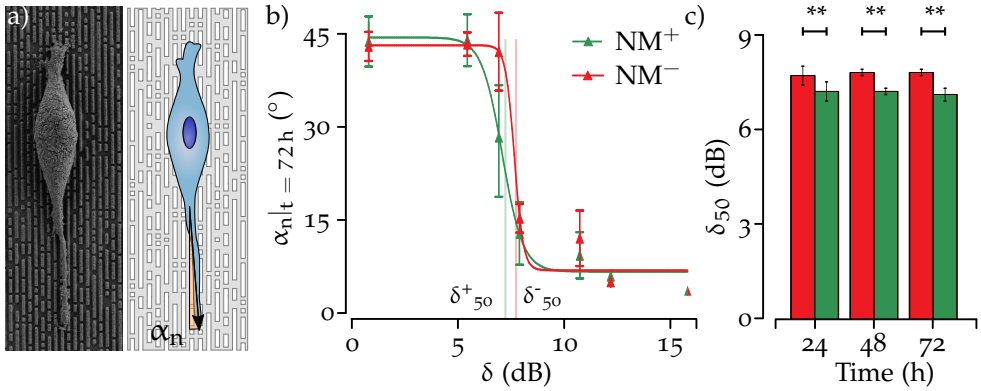

Figure 4.5: PC12 neurite alignment. (a) SEM image of a differentiated PC12 cell on NM$^+$ and sketch depicting how neurite alignment α_n is defined. (b) Neurite alignment at 72 h for NM$^+$ and NM$^-$. Sigmoidal fit is graphed for each dataset. δ_{50} for both curves are indicated. (c) δ_{50} on positive and negative noise for the three time points measured. **P $<$ 0.01

According with the results reported in FIGURE 4.5c, topographical-reading thresholds were located at $\delta = 7.8$ dB and $\delta = 7.2$ dB for negative and positive noise, respectively. These values correspond to $p \approx 40\%$ and $p \approx 50\%$, respectively, meaning that PC12 cells could follow the NG even if about 50% of its ridges or grooves were randomly modified. The comparison between the two types of noise showed that neurites growing on gratings with NMs$^-$ had a higher δ_{50} than those growing on NMs$^+$ ($P < 0.01$, Student's t-test), indicating that PC12 cells are more tolerant to positive than negative noise. This effect could be explained with the different constraint imposed by the two types of nano-modifications on FA-maturation: NMs$^+$ interrupt the ridges, reducing the space available for cell-adhesion and hindering the elongation of FAs. On the contrary, NMs$^-$ create bridges between adjacent ridges, allowing the maturation of misaligned FAs.

4.3.3 Focal adhesions and nano-modifications

In order to have better insight into the role of FAs in topographical sensing of partially masked geometries, a detailed analysis of FA organization during the early stages of cell adhesion and neurite outgrowth was implemented and is reported in the following. PC12 cells were transiently transfected with EGFP-paxillin (see APPENDIX B.8), seeded on noisy NGs, and differentiated by NGF administration as described in the previous section. Paxillin spatial distribution was then acquired by TIRF microscopy (see APPENDIX B.11.2 for additional details), allowing the visualization of FAs at the cell basal-membrane, minimizing the background signal originat-

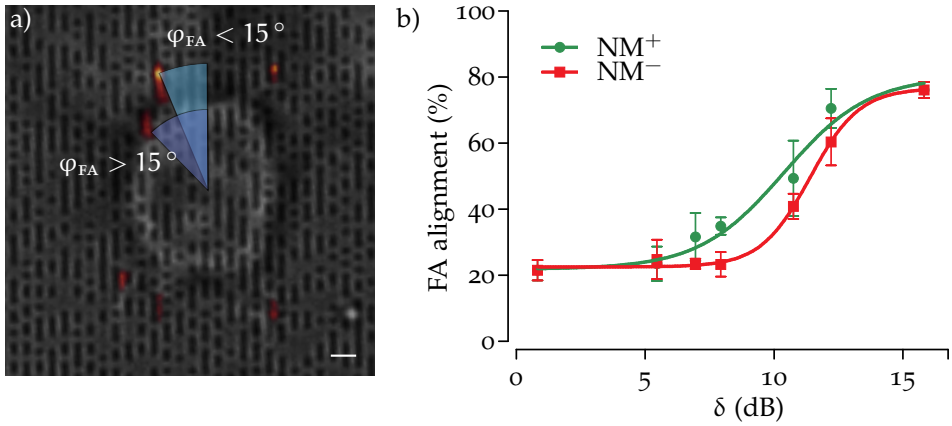

Figure 4.6: Focal adhesion alignment on noisy nanogratings. (a) Bright field imaging of a PC12 on a 20%NM$^-$ grating. TIRF imaging of EGFP-paxillin is over-imposed, showing FAs as bright spots. The alignment angle formed by two representative FAs is sketched and colored in light or dark blue if the adhesion was aligned ($\varphi_{FA} \leqslant 15°$) or misaligned ($\varphi_{FA} > 15°$), respectively. Scalebar 3 µm. (b) FA alignment as a function of substrate directionality δ, on positive (green line) and negative (red line) noise, reported as the % of aligned FAs. Data are reported as mean ± SEM (1 530 FAs quantified). Gratings with $\delta \geqslant 12.2$ dB are significantly different than gratings with $\delta \leqslant 7.9$ dB and FLAT ($P < 0.05$–0.001) for both NM$^+$ and NM$^-$; $\delta = 15.8$ dB vs. $\delta = 10.8$ dB NM$^-$ ($P < 0.01$, One-Way ANOVA, Tukey's test)

ing from the cytoplasm. FA spatial distribution, density (number of adhesion per cell), and maturation (adhesion area) was measured in all the studied substrates.

Focal adhesion distribution

The decrease of δ induced an increase in the number of FAs per cell, both for negative and positive noise, with respect to an unmodified NG[188], reaching significance for $\delta \leqslant 7.0$ dB ($P < 0.05$, One-Way ANOVA, Dunnett's test). FA distribution was analyzed by grouping the adhesions depending on the angle φ_{FA} they formed with the grating, using cell-center as vertex (see the schematics in FIGURE 4.6a). If $\varphi_{FA} \leqslant 15°$, the adhesion was considered *aligned*, if $\varphi_{FA} > 15°$ it was considered *misaligned*. The graph in FIGURE 4.6b shows FA alignment loss, with an δ_{50} of 11.3 ± 0.1 dB and 10.0 ± 0.3 dB for NMs$^-$ and NMs$^+$, respectively. Negative noise had a greater impact on contact guidance compared to positive noise ($P < 0.05$, δ_{50} NM$^-$ vs. NM$^+$), in line with what observed for neurite alignment.

Small	Intermediate	Large
$A_{FA} \leqslant 1\,\mu m^2$	$1\,\mu m^2 < A_{FA} \leqslant 2\,\mu m^2$	$A_{FA} > 2\,\mu m^2$

Table 4.1: Focal adhesion size. FAs are divided in 3 groups depending on their size.

Focal adhesion maturation

FA maturation is accompanied by an increase in the size of individual adhesions and can be evaluated by TIRF microscopy[134,140,178]. Therefore, for each substrate FAs were divided in three categories depending on their area (A_{FA}), as reported in TABLE 4.1. The graphs in FIGURE 4.7a and c on page 79 show that aligned FA maturation was correlated to δ for both NM^+ and NM^-, and resulted in the increase of the small FA fraction as substrate directionality decreases (from approximately 45% for $\delta = 15.8$ dB up to values higher than 90% for $\delta = 5.5$ dB). No similar behavior was observed for misaligned FAs (FIGURE 4.7b and d on page 79).

Since FAs are important actors in the cytoskeletal organization and in the regulation of cell-contractility (see SECTION 3.1.1), we can argue that the fragmentation of FAs induced by high levels of topographical noise resulted in an overall reduction of contractility. This reduction would contribute to the loss of contact guidance since, as demonstrated in previous studies[140,164], PC12 alignment to NGs requires myosin-II contractility, and activation of Rho-associated protein kinase (ROCK).

4.3.4 Pharmacological tuning of contact guidance

In the following I will describe how the tolerance to topographical noise can be tuned by pharmacologically interfering with PC12 cell-contractility. Since the experiments presented in the previous paragraphs did not show qualitative differences between NM^+ and NM^-, the following analysis will be limited to the *positive noise*.

Blebbistatin, a myosin-II contractility inhibiting drug, was first tested. In line with our previous results[164], this treatment impaired mechanotransduction. Indeed, contact guidance in the presence of blebbistatin (25 μM) was less effective and neurite alignment was reduced for NGs tested. As shown in FIGURE 4.8a, this drug has a disruptive effect on cell-to-grating alignment, resulting in greater alignment angles α_n on each topography.

The effect of *nocodazole* was then assayed. This drug is a potent microtubule depolymerizing agent that was shown to activate the Rho-A-ROCK-MLC pathway, leading to an increase of cell contractility[189]. PC12 neurite alignment vs. substrate directionality in presence of nocodazole (10 nM) was measured after 24, 48 and 72 h of NGF-induced differentiation.

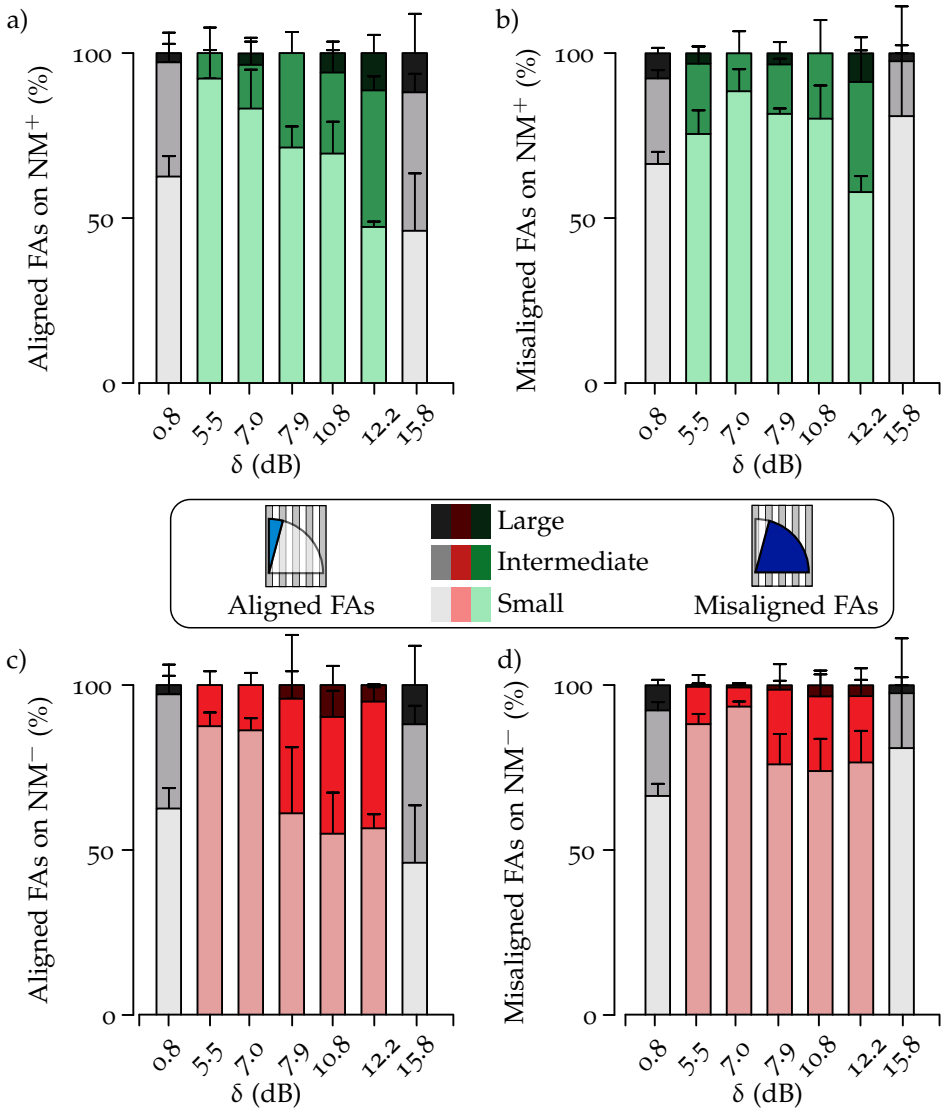

Figure 4.7: Focal adhesion maturation on noisy nanogratings. The bar plots show the relative distribution (% of the total) of small ($A_{FA} \leqslant 1\,\mu m^2$), intermediate ($1\,\mu m^2 < A_{FA} \leqslant 2\,\mu m^2$) and large ($A_{FA} > 2\,\mu m^2$) FAs for each substrate. Green and red bars are relative to gratings with positive (a,b) and negative (c,d) noise, respectively. Gray bars represent non-noisy topographies (i. e. $\Lambda 1$ grating and FLAT substrates). Data are reported as mean±SEM (1 530 FAs quantified).

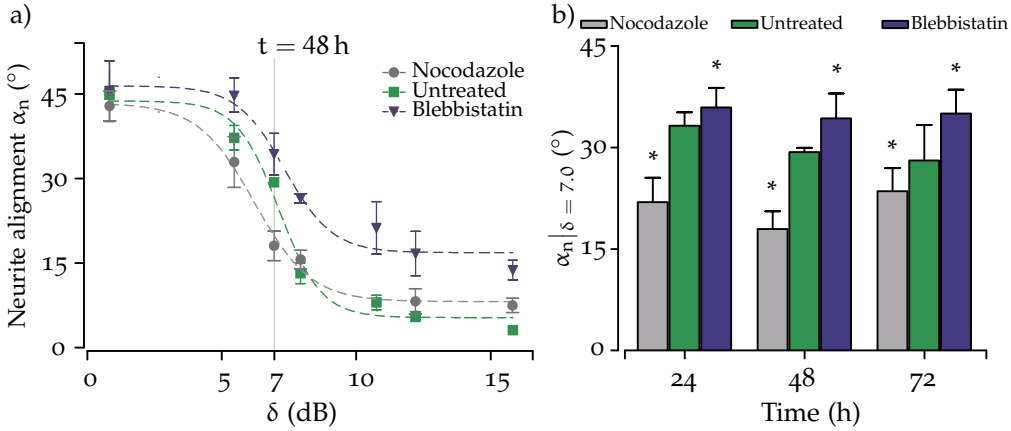

Figure 4.8: Pharmacological modulation of noise tolerance. a) Neurite alignment as a function of substrate directionality at $t = 48$ h in presence of nocodazole 10 nM (gray lines), blebbistatin 25 μM (blue lines) and for the control condition (green lines). Blebbistatin inhibits cell contractility and negatively affects neurite alignment on noisy NGs, $P = 0.053$ δ_{50} blebbistatin vs. untreated (Student's t-test). Data are reported as mean ± SEM (2 200 neurites quantified). c) Neurite alignment for $\delta = 7$ dB (60% noise) at $t = 24$, 48 and 72 h in presence of nocodazole (grey bars), blebbistatin (blue bars) and for the control condition (green bars): * $P < 0.05$ untreated vs. nocodazole and vs. blebbistatin (Student's t-test).

FIGURE 4.8 demonstrates that, contrary to what was obtained with blebbistatin, the tolerance of contact guidance to noise was significantly improved with respect to the untreated condition ($P < 0.01$, nocodazole 10 nM vs. untreated, Student's t-test). The resulting δ_{50} lowered to 6.6 ± 0.1 dB, 6.2 ± 0.3 dB and 6.5 ± 0.2 dB at 24, 48 and 72 h respectively, corresponding to a smaller neurite alignment angle α_n (i. e. a better guidance) on NGs with low directionality ($\delta \leqslant 7$ dB, i. e. $P = 60\%$ and 80%). Unlike blebbistatin, the effects of nocodazole at low levels of noise were barely-detectable (FIGURE 4.8a). A better insight over the opposite effects induced by blebbistatin and nocodazole is provided by the graph in FIGURE 4.8b, which compares neurite alignment α_n for samples close to the directionality threshold ($\delta = 7.0$ dB). The graph shows a significative reduction of α_n for the nocodazole-treated cells with respect of the untreated condition and, at the same time, a significative increase of the same parameter for blebbistatin-treated cells.

Finally, the effect of nocodazole on FA development was investigated. I focused this analysis in the region of high topographical noise ($\delta = 7.0$ dB), where the nocodazole-induced-increase of cell-contractility obtained the maximum effect in neurite alignment-recovery (see SECTION 4.3.4).

PC12 were transiently transfected with fluorescent EGFP-Paxillin, differentiated by NGF and treated with nocodazole after 6 h from NGF administration. FA spatial

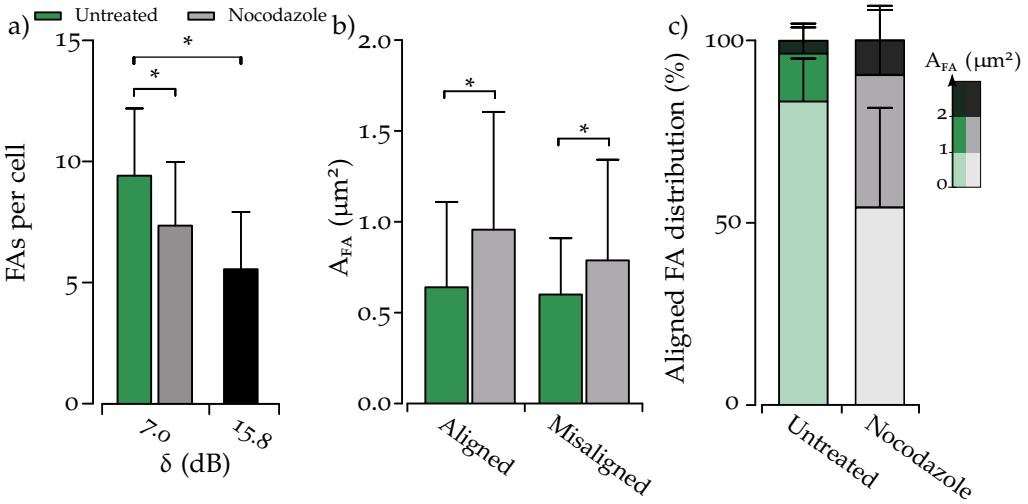

Figure 4.9: Focal adhesion development in presence of nocodazole. (a) Number of FAs per cell (mean ± SD, 44 measured cells; $n \geqslant 2$) for $\delta = 7$ in presence of nocodazole 10 nM (grey bar) and for the untreated condition (green bar). The black bar refers to NGs with no-noise (*$P < 0.05$ Student's t-test). (b) Area of aligned and misaligned FAs measured on NGs with $\delta = 7$ dB, in the presence of nocodazole 10 nM (grey bars) and for the untreated condition (green bars). Nocodazole leads to larger FAs (*$P < 0.05$ Mann Whitney test; mean ± SD, 242 FAs quantified; $n \geqslant 2$). (c) FA size distribution. Data are reported as mean±SD (242 FAs quantified; $n \geqslant 2$).

distribution was not affected by nocodazole ($P > 0.05$ nocodazole vs. untreated), while the number of FAs per cell had a significative reduction, reaching values comparable with the ones of an unmodified NG (FIGURE 4.9a).

FA maturation was favored by nocodazole: FIGURE 4.9b shows that FAs grew more in treated cells than in untreated ones ($P < 0.05$ nocodazole vs. untreated, Mann Whitney test), for both alignments. No significant difference was measured between aligned and misaligned FAs. Instead, the size distribution of aligned adhesions was affected (FIGURE 4.9c): the percentage of small FAs decreased while more adhesions with intermediate and large dimension were established.

These results indicate that the cell-contractility machinery has a crucial role in tuning cell sensitivity to directional stimuli, being able to increase or reduce the tolerance of neurite and FA alignment towards nanotopographical noise.

4.3.5 Conclusions

High-resolution live-cell imaging was performed on the noisy nanotopographies using both bright field and TIRF microscopy. Biocompatibility was demonstrated

by culturing PC12 cells and evaluating cell viability and NGF-induced neuronal-differentiation efficiency. No significant differences could be found with respect to unmodified NGs.

The effect of topographical noise on neurite alignment was analyzed, showing a sigmoidal loss from the values measured on $\Lambda 1$ gratings down to the random neurite distribution found on FLAT substrates. The modulation of directionality also influenced FA orientation and maturation, with a trend similar to the one observed for neurite alignment. This demonstrates that neurite pathfinding is capable of retrieving information from partially ordered topographies through a mechanism that involves FA-sensing.

Finally, pharmacological rescue of neurite alignment was investigated. Nocodazole, a potent microtubule depolymerizing agent that is known to increase cell contractility via Rho-A pathway activation, emerged as an effective drug to improve neurite alignment and aligned-FAs maturation at low substrate directionalities.

4.4 STEM CELL MECHANOTRASDUCTION ON NOISY NANO–TOPOGRAPHIES

The modulation of cell migration, invasion and terminal differentiation by artificial physical cues is of paramount importance for implementing effective stem cell based tissue engineering protocols for regenerative medicine applications[190]. Although micro- and nanomaterial driven differentiation has been studied by many groups[170,191,192] the regulation of stem cell migration by contact interaction is still largely unknown.

Bone-marrow human mesenchymal stem cells (BM-hMSCs) are the most commonly used cells in clinical applications and basic research. Many therapeutical approaches based on hMSCs have been proposed. Some of them take advantage of hybrid hMSC-biomaterial scaffolds that are implanted in the human body. When *in situ*, cells migrate off the scaffold and undergo terminal differentiation leading to device integration and regeneration of the damaged area. Beyond soluble factors, other factors can stimulate this process[193,194] and improve the final transplantation outcome[195,196] such as the physical properties of the scaffold (e. g. stiffness, density, topography, porosity, roughness).

Owing to the rather invasive extraction procedure, however, in the last few years, hMSCs have been actively sought for in other human tissues[197]. Wharton's jelly human mesenchymal stem cells (WJ-hMSC) are extracted from the part of the umbilical cord composed of a mucous-connective tissue matrix that is rich in stem cells, collagen fibers and proteoglycans[198,199].

Here, I will report my results in the study of WJ-hMSC polarization and migration as a function of the controlled directional stimuli provided by noisy NGs. Mechanotransduction in WJ-hMSC was measured by evaluating cell morphology and alignment, cytoskeleton polarization, FA development and spatial distribution by fluorescence microscopy on fixed and living cells. Finally, dynamical interaction of WJ-hMSC with negative noise (NM^-) was studied by the analysis of single-cell migration.

4.4.1 Cell viability

Experiments were performed at short and medium term: 24 h and one week after seeding. In order to detect living and dead cells, we used different fluorescent dyes and 3-channel epifluorescence microscopy.

Measurements demonstrated that none of the six topographies affects cell viability significantly. In particular, for both time points, the percentage of viable cells was ($94 \pm 2\%$) in line with typical values obtained for standard plastic substrates, e. g. tissue culture poly (styrene) (TCPS). This result confirmed the possibility to test our topographies in long-term experiments, such as cell proliferation, migration and differentiation assays.

4.4.2 Single cell morphological analysis

In order to quantify cell area, polarization and alignment to the gratings, cells were stained with Calcein AM and images were acquired by epifluorescence microscopy (two representative fields are reported in FIGURE 4.10a). Then, image binarization and automatic analysis were used to measure single-cell morphological parameters (FIGURE 4.10a).

FIGURE 4.10b shows the average cell area (A_{cell}) measured with the different nanotopographies. Overall, patterned surfaces resulted in a cell-area reduction of about 20% as compared to FLAT, even though this difference was not statistically significant. Remarkably, noise did not affect A_{cell} with respect to the no-noise condition ($\Lambda 1$ substrate). Results on cell polarization (ε_{cell})—defined as the ratio between cell-major and -minor axes—are shown in FIGURE 4.10c. WJ-hMSC are naturally polarized cells, with $\varepsilon_{cell} = 0.4 \pm 0.03$ on FLAT. As expected, interaction with $\Lambda 1$ led to ε_{cell} reduction of about the 25%. Contrary to what observed for cell area, ε_{cell} was restored to its FLAT value by nano-modifications, regardless of its density. The angular distribution of cell alignment (α_{cell}) for each substrate showed that cells on all the noisy NGs and on FLAT were randomly oriented[190]. Instead, as demonstrated in

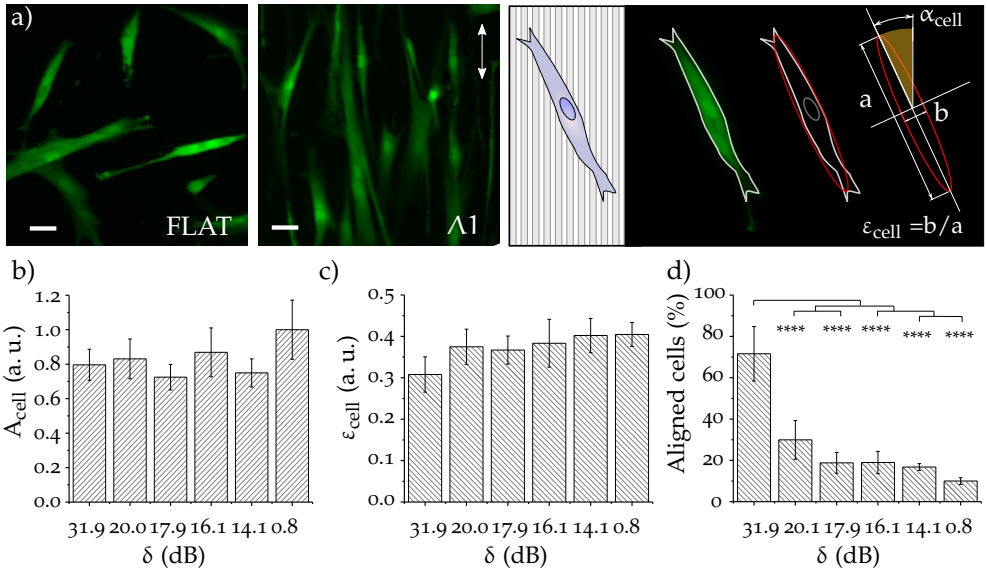

Figure 4.10: WJ-hMSC morphology. (a) Representative cell images at $t = 24$ h after seeding on Λ1 and FLAT. Cells were stained with Calcein AM. Scalebar 50 μm. A schematic of the method used for cell morphology characterization is reported. After fitting the cell contour with an ellipse, major and minor axes (a and b, respectively) and orientation (α_{cell}) were measured. (b) Cell area (A_{cell}) vs noise. Data were normalized to the FLAT value. (c) Cell polarization (ε_{cell}) vs δ. $\varepsilon_{cell} \to 0$ indicates full polarization, $\varepsilon_{cell} \to 1$ correspond to round shaped cells. (d) Percentage of aligned cells ($\alpha_{cell} \leqslant 15°$) vs δ. Four independent experiments were performed. (**** $P < 0.0001$)

FIGURE 4.10d, Λ1 induced a net (70%) and significant improvement of cell alignment with respect to all other conditions.

Analysis of cell cytoskeleton was performed by immunofluorescence techniques. Three fluorescent dyes were used to detect actin cytoskeleton, vinculin aggregation in FAs, and cell nuclei (see APPENDIX B.10). Confocal microscopy was used to acquire high-resolution images. FIGURE 4.11a reports six representative images of actin cytoskeletons, acquired on the different substrates. WJ-hMSC showed a well-organized cytoskeleton, with evident actin stress fibers. Fourier transform (FT) analysis was exploited to study the spatial organization of actin fibers (see APPENDIX B.10.3). FIGURE 4.11b shows that $85 \pm 6\%$ of cells grown on Λ1 presented well-oriented actin fibers extending along the grating-direction ($\alpha_{actin} < 15°$). Notably, this percentage was reduced by 42% in the presence of 20%NM^{-}, which resulted significantly more aligned than those with higher percentages of noise ($p \geqslant 60\%$).

Single-cell actin dispersion is reported in FIGURE 4.11c. In this case the best performances were also obtained with Λ1 gratings, whose dispersion was almost one

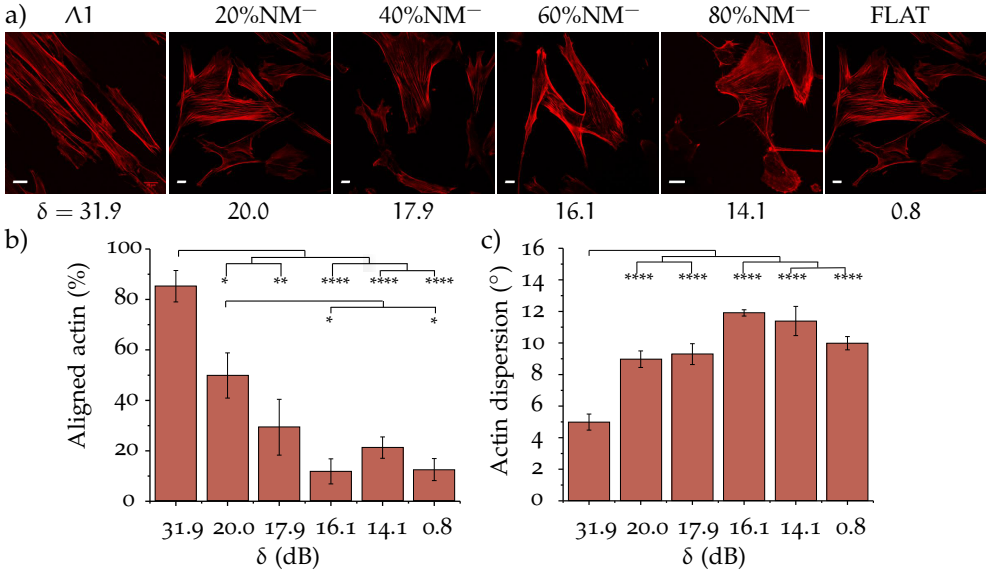

Figure 4.11: Actin cytoskeleton polarization. (a) Representative fluorescence images of actin cytoskeleton acquired at $t = 24\,h$ after cell seeding. Scalebars 20 μm. (b) Percentage of cells with aligned actin ($\alpha_{actin} \leqslant 15\,°$) vs δ. (c) Single cell actin dispersion vs δ. Five independent experiments were performed (*P < 0.05, ***P < 0.001, ****P < 0.0001).

half of the one measured for all the noisy topographies. Interestingly, data relative to high noise percentage (p = 60–80%) substrates indicated a greater dispersion with respect to data obtained on FLAT.

4.4.3 Focal adhesion morphology

FAs were detected as vinculin clusters (see SECTION 3.1.1) by immunofluorescence techniques and confocal microscopy (representative images are shown in FIGURE 4.12a). FA morphological parameters were semi-automatically measured from fluorescence images by image correlation methods[200]. FAs were modeled as ellipsoidal bodies and described by the following parameters: area (A_{FA}), axis length (d_{min} and d_{MAX}), elongation ($p_{FA} = d_{min}/d_{MAX}$), and alignment to the pattern (φ'_{FA}). We also quantified FA density (i.e. the average number of FAs per cell) and FA spatial distribution within single cells. FIGURE 4.12b indicates that NGs inhibited the full development of FAs. As shown in FIGURE 4.12c, Λ1 and the 20%NM⁻ led to $d_{min} \approx 0.55 \pm 0.03$ μm, a value comparable to the substrate ridge width.

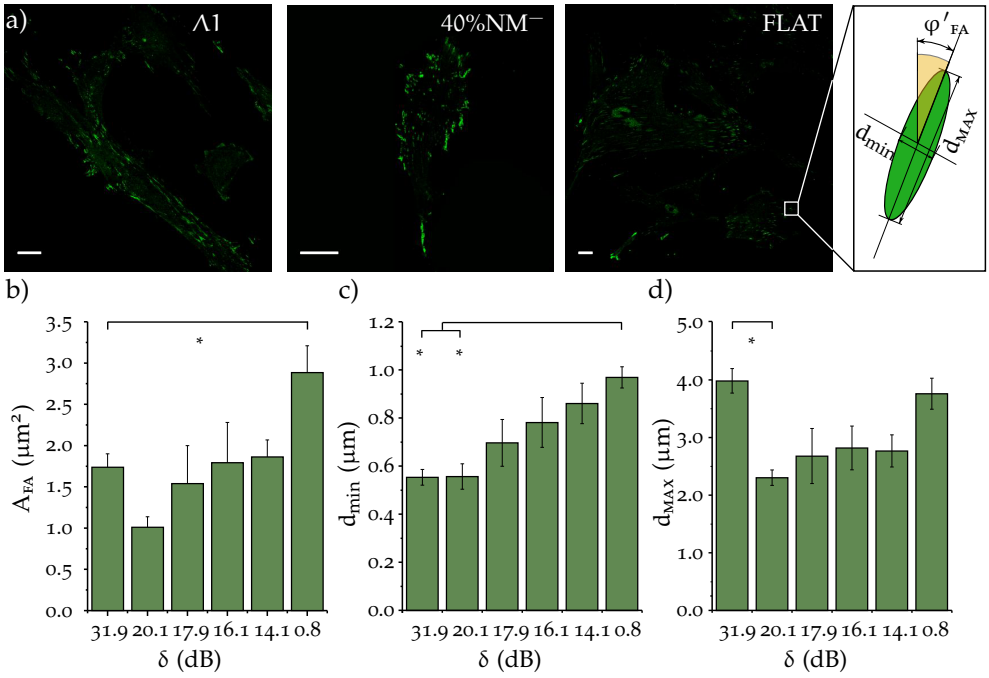

Figure 4.12: Focal adhesion morphology. (a) Representative fluorescence images of vinculin clusters on $\Lambda 1$, 40%NM^- and FLAT and schematics of FA morphometric analysis. FAs were modeled as ellipses, for which major (d_{MAX}) and minor axes (d_{min}), and directionality (φ'_{FA}) were measured. Scalebars 20 μm. b) Area (A_{FA}), (c) minor axis (d_{min}) and (d) major axis (d_{MAX}) vs δ. Three independent experiments were performed (*$P < 0.05$).

Increased noise made a larger surface area available for cell adhesion and FA maturation. Indeed, d_{min} reached values indistinguishable from those obtained on FLAT ($d_{min} < 1\,\mu m$) while d_{MAX} displayed a different response (FIGURE 4.12d). FAs could elongate freely on FLAT and $\Lambda 1$ ($d_{MAX} = 3.99 \pm 0.21\,\mu m$ and $3.76 \pm 0.27\,\mu m$, respectively), while noisy NGs reduced FA stretching by approximately 35%. Thus, these modifications affected both FA area and elongation, as shown in FIGURE 4.12b–d. FAs were naturally ellipsoidal with $p_{FA} = 0.259 \pm 0.007$ on FLAT. Polarization almost halved (46%) on $\Lambda 1$, while the presence of NMs^- restored the conformation found on FLAT. Moreover, as shown in FIGURE 4.12b, all the NGs—with or without nano-modifications—halved the A_{FA} with respect to the value measured on FLAT. The cells that were mainly affected by this effect were those grown on substrates with a low noise (p = 20–40%), where an increased number of FAs could also be observed [190].

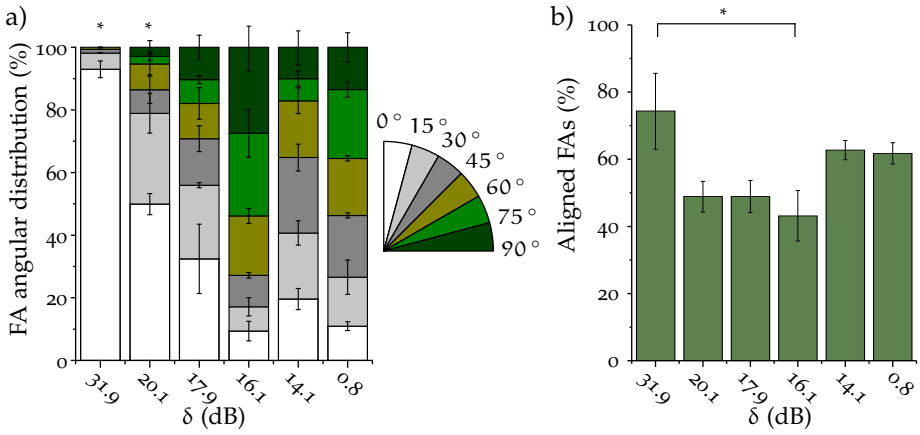

Figure 4.13: Focal adhesion alignment to nanogratings. (a) FA angle distribution with respect to the grating direction for different δ. Bin size: 15 ° (*P $<$ 0.05). (b) Percentage of aligned FAs ($\varphi'_{FA} \leqslant 15\,°$) vs δ (*P $<$ 0.05).

FA spatial distribution within single cells were also modified by NGs. Majority of FAs were aligned to the cell polarization direction on Λ1. FLAT and 80%NM$^-$ maintained 60% of FAs aligned to the cell axis, whereas low and medium percentages of noise reduced this alignment slightly. As expected, the radial distribution of FAs was unaffected by any of the substrates: 60% of FAs were consolidated at the cell periphery, where they experienced the maximum traction applied by actin stress fibers[190].

φ'_{FA} strongly depended on the specific topography used (FIGURE 4.13), showing a behavior similar to that obtained for cell alignment. On Λ1, cells established almost all the FAs (90%) parallel ($\varphi'_{FA} < 15\,°$) to the pattern, while no FAs were found with $\varphi'_{FA} > 60\,°$. The addition of NMs$^-$ broadened this distribution. On low-noise gratings (p = 20–40%) a reduced number of parallel FAs (40-–60%) and an overall rise of all the other bins of the angular distributions were measured. Above 60%NM$^-$ the distribution flattened, showing a slight increase of misaligned FAs ($\varphi'_{FA} > 45\,°$) for the 60%NM$^-$ pattern. FIGURE 4.13b focuses on aligned FAs ($\varphi'_{FA} < 15\,°$) demonstrating that Λ1 and 20%NM$^-$ lead to a significant increase in the number of aligned FAs with respect to all other substrates.

Summarizing, FAs primarily assemble along the cell periphery and exhibit a polarized shape defined by the pattern direction. FA size halved on Λ1 with respect to measurements on FLAT and was modulated by noise level. In particular, small FA clusters were favored by 20%NM$^-$, suggesting that this specific geometrical arrangement of imperfections may particularly influence FA maturation. This is supported

by the presence of a larger number of FAs at this noise level that we argue are part of a feedback mechanism to successfully counteract the presence of weak anchor points and to maintain the correct internal mechanical stress balance[175]. FA spatial distribution drives the formation of actin stress fibers that in turn align[12,201,202]. reflecting FA angular distribution, and finally lead to cell remodeling and alignment to the pattern. Good correspondence between cell alignment (FIGURE 4.10) and actin alignment (FIGURE 4.11) was found. Importantly, the actin reshaping did not significantly affect cell area, a condition that could promote pathological dysfunctions[203].

4.4.4 Single cell migration

WJ-hMSC migration was recorded by time-lapse microscopy after staining cell nuclei with a vital fluorescent dye (Syto16, Invitrogen, Italy). Frames were acquired every 15 min for 15 h, which allowed information to be gathered at two time-scales. None of the NGs affected migration global parameters, i. e. the distance from the origin after 15 h (R), total path covered in 15 h (S), average migration step (dS) or speed (V). Specifically, we measured $R = 127.2 \pm 3.5\,\mu m$, $S = 324.4 \pm 11.6\,\mu m$, $dS = 5.2 \pm 0.2\,\mu m$ and $V = 20.9 \pm 0.8\,\mu m/h$. These quantities were calculated by averaging the values measured for each substrate (see APPENDIX B.12). Nonetheless, migration directionality was driven by contact guidance. FIGURES 4.14a and b show representative tracks: cell random walks were observed on FLAT and were compared with $\Lambda 1$-driven migration in which tracks followed NG lines. Migration was then characterized along two directions: parallel (0 °–15 °) and perpendicular (75 °–90 °) to the NGs. For FLAT, one random direction was chosen together with its perpendicular. The percentage of parallel migration steps doubled on $\Lambda 1$ with respect to FLAT and high-noise topographies (60%NM^- and 80%NM^-), as shown in the graph in FIGURE 4.14d. A reduction, though to a lesser extent, was also found for 20%NM^- and 40%NM^-. On the contrary, gratings did not affect the parallel speed (V_{par}) (FIGURE 4.14f) and results were not significantly modified. The same was obtained for the speed calculated along other directions with angles up to 75 ° with respect to the grating. FIGURE 4.14e reports the percentage of perpendicular steps on the different substrates. As expected, $\Lambda 1$ led to a suppression of the migration across the ridges where increasing noise progressively reduced this constraint. Perpendicular movement was slower on $\Lambda 1$, leading to a reduced perpendicular speed (V_{per}) of 50% with respect to V_{per} on FLAT. Conversely to what was obtained for V_{par}, noise was found to affect V_{per} (FIGURE 4.14g). The presence of bridges between ridges made more anchoring points available, allowing easier movement across the grating.

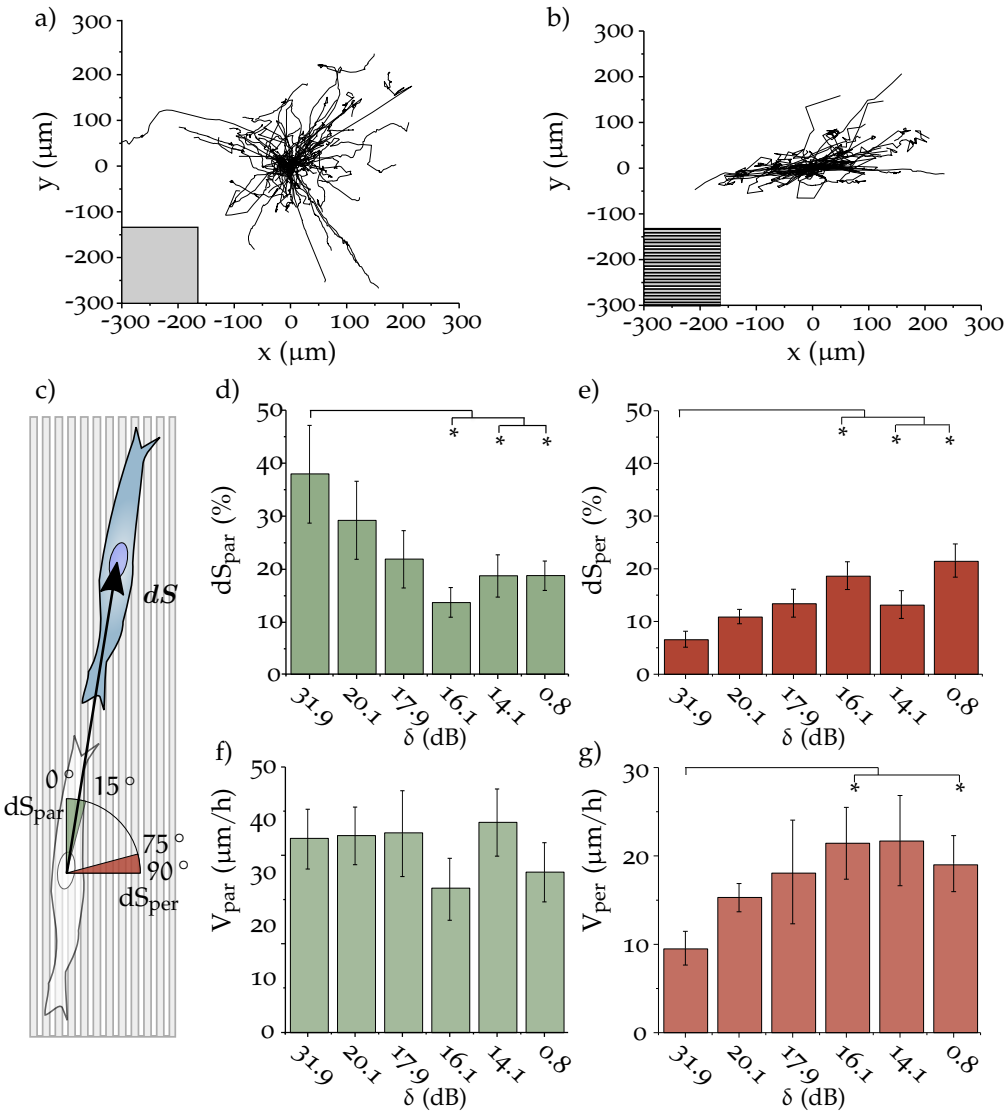

Figure 4.14: (a,b) Representative tracks of cells moving on Λ1 and FLAT surfaces, respectively. (c) Measurement schematic. (d) Percentage of steps aligned (dS_{par}) to the pattern direction (0–15 °) and (f) relative speed (V_{par}). (e) Percentage of steps perpendicular (dS_{per}) to the pattern directionality (75–90 °) and (g) relative speed (V_{per}). 4 independent experiments were performed (*$P < 0.005$).

Cell migration is one of the important biological processes regulated by ECM-cell interaction[156,204,205]: it is fundamental for embryogenesis, development, and for many other physiological processes such as tissue renewal or immune response. Migration is also pivotal for pathogenic processes (e. g. cancer-cell invasion of healthy tissues), and tissue repair after injury. Controlled migration would be particularly desirable with stem cells in order to drive injected cells towards their target position as rapidly as possible. These results showed that NGs do not strongly affect global migration parameters (path and speed), but can control the movement direction. This property is consistent with previous studies with other cell types (e. g. fibroblasts) on similar anisotropic substrates[206,207]. Cells freely moved on FLAT substrates, while their motion on NGs was confined along the pattern direction. This effect was tuned by NMs^{-}, which progressively reduced migration directionality. For $p \geqslant 40\%$, the substrates are ineffective in directing cell motion.

4.4.5 Dependence on δ

These results show a difference in WJ-hMSC tolerance to nano-topographical noise compared to what was found in SECTION 4.3 for PC12 neurite alignment. Nano-modifications interfere dramatically with WJ-hMSC ability to respond to noise-degraded directional stimuli, causing a major loss of cell-response after only $20\%NM^{-}$.

This behavior can be explained by considering the dependence of δ on the pattern area A (see SECTION 4.2.2). The average area of a WJ-hMSC-cell on a FLAT surface is $3\,421\,\mu m^2$, much wider than a PC12 (approximately $100\,\mu m^2$). Indeed, $\delta(p, 3421)$ monotonically decreases with p, but with a marked non-linear behavior, reducing by 42% when p increases from 0 to 20%. This effect rapidly saturates and a further increase of p from 20% to 80% leads to a reduction in δ of only 8%.

4.4.6 Conclusions

In conclusion, I investigated the influence of highly anisotropic and noisy substrates on WJ-hMSC by focusing on cell morphotype and migration by means of biochemical assays and fluorescence/confocal microscopy. My results show that migration on perfect nanogratings is highly directional. On the contrary, pattern degradation may means of negative nano-modifications (NMs^{-}) leads to a loss of cell directionality, even at very low noise levels. The same effect was also observed on cell morphology: while a slight cell area reduction was reported for all NGs, only the non-noisy gratings induced cell polarization. Molecular analysis revealed that cell polarization corresponds to actin cytoskeleton organization, with ordered stress fibers following NG lines. Furthermore, this cytoskeletal structure correlated with FA size and spatial

arrangement. In the case of unperturbed NGs we observed FAs that developed at cell terminations and were aligned to the pattern. Finally, we observed that NGs, with or without noise, constrained and stretched FAs along ridges, reducing their area and inhibiting their maturation. These results indicate that highly-anisotropic topographies might be successfully applied to drive stem-cell migration in new regenerative-medicine protocols. Importantly, I showed that pattern fidelity is crucial for proper translation of the topographical signal into the desired cell response: pattern degradation may result in altered mechanotransduction at molecular (rearrangement of FA and actin fibers), morphological (cell area and polarization), and functional (cell migration) levels. This indicates that small scaffold alterations resulting from interaction with the host tissue—e. g. deposition of extracellular matrix components, degradation of bioresorbable devices, cell invasion—need to be carefully considered when evaluating the actual scaffold operation time for active regenerative therapies.

5 TOWARDS PRE-CLINICAL TRANSLATION

Previously, I introduced micro- and nanogratings for polarizing cell bodies and migration patterns, discussing the potential benefits of their use in the field of regenerative medicine. In this chapter I will present the results obtained by applying directional topographies to a specific clinical problem, i.e. the regeneration of peripheral nerves. First I will introduce the problem and discuss an in vitro study of Schwann cell migration on PDMS gratings, comparing structures of different periodicity. Then I will present preliminary results on the pre-clinical translation of this technology using a rat model of median nerve transection. Finally, I will report the first results of a collaboration aimed to transfer of nanogratings onto PCL/PLA membranes, an FDA-approved, biodegradable polymer blend optimized for the regenerative medicine applications.

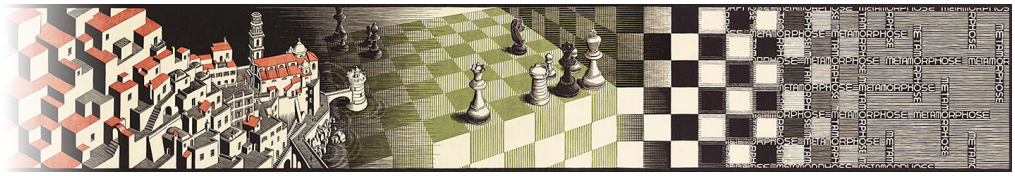

5.1 INTRODUCTION

Peripheral nerve injury is a common form of trauma with up to 400 000 cases each year[208,209]. Nerve lesions can significantly complicate the clinical course and outcome of injured patients and are present in about 5% of all open wounds in the extremities caused by sports or traffic accidents. In the peripheral nervous system, nerves regenerate spontaneously when injuries are minor. In the most severe lesions, in which there is distortion of the endo-neural tubes with or without peri-neural disruption (Sunderland grade III or grade IV), prognosis for spontaneous regrowth is diminished and surgical repair is often required. In complete nerve lesions (Sunderland grade V) axonal regrowth will not usually occur unless the nerve endings are free from scar tissue and are surgically reapproximated[210].

Although advances in surgical techniques have brought significant improvements, functional recovery is often suboptimal. The choice of surgical protocol is dependent on the size of the nerve gap between the proximal and distal stumps[211]. Short gaps can be repaired directly by mobilization of the proximal and distal stumps

with end-to-end coaptation and epi-neural suturing. Long nerve gaps (> 2 cm) require additional material to bridge the defect, which further reduces the functional outcome[212].

The current standard repair method is based on the use of autologous nerve grafts (*autografts*), which provide the regenerating axons with a natural guidance channel populated with functioning Schwann cells (SCs) surrounded by their basal lamina[213]. Nerve autografting, however, is far from being an optimal treatment, and even after optimal surgical repair the functional outcome is disappointingly poor, especially for sensory recovery[214]. This poor outcome is largely due to the death of primary sensory neurons, but also to the lack of fiber regeneration over the gap that leads to target-organ denervation.

A promising alternative to nerve autografting is the use of artificial scaffolds. They are typically composed of an active biomaterial embedded in a supporting conduit. This approach has several advantages over autografts. First of all it does not require the extraction of healthy tissue from the patient. Then, the scaffold typically provides a guidance channel and mechanical support, and reduces scar formation by limiting the invasion of the connective tissue into the lesion[215]. Moreover, it can be engineered to provide the optimal chemical and physical microenvironment for nerve functional recovery[216]. Basic research and clinical results have shown that bioabsorbable devices can induce comparable or even superior nerve reconstruction than nerve autografts[213]. Nevertheless, the functional recovery of the nerve is still not satisfying and the use of scaffolds is limited to rather small nerve gaps[217] (< 5 cm in humans and 1.5 cm in rats).

Anisotropic topographies represent interesting tools for peripheral nerve regeneration. Their ability to spatially bias cell migration patterns and neurite outgrowth can potentially reduce the times needed for the regrowing end to fill the nerve transection-gap. Moreover, surface structuring does not alter either the chemistry or the bulk properties of the scaffolds, making geometry- and material-optimization almost orthogonal processes. In the rest of this chapter I will describe the use of different micro-gratings to control the migration of SCs, glial cells crucial in the regulation of neuronal survival and differentiation[218,219]. In healthy peripheral nerves, SCs grow in close contact with axons, contributing to the propagation of electrical signals[219]. If a lesion causes nerve transection, SCs migrate from the stumps, guiding the regrowing proximal end towards the distal one. Given the crucial role that SCs have in peripheral nerve regeneration, the scaffolds for the treatment of nerve injury have to provide a suitable environment for the migration of these cells between the nerve stumps. Therefore, *in vitro* studies of SC interaction with the scaffolds are an accepted model for a preliminary evaluation of the scaffold performances before pre-clinical testing[208,218–220].

Name	Periodicity (Λ)	Depth (d)	Aspect ratio (AR)
$\Lambda 4_p$	4 μm	0.85 μm	0.43
$\Lambda 20_p$	20 μm	2.50 μm	0.25

Table 5.1: Microratings for nerve conduits. Gratings for the creation of microstructured PDMS membranes.

The topographies were initially fabricated on PDMS membranes, in order to obtain scaffolds suitable for *in vitro* analysis of cell migration and, notably, for pilot tests of *in vivo* nerve regeneration in a rat model of median nerve transection. PDMS has several features making it a widely suitable material material for biomedical use[221,222]: it is chemical and biological inert, non-toxic, has excellent mechanic resistance and elasticity, and is compatible with standard soft lithography techniques. These characteristics make PDMS very useful for scaffold-prototyping, but its lack of biodegradability imposes severe limits over its use for long-term applications. For this reason, I will finally present preliminary results on pattern transfer of nanogratings on a polymer blend of poly(caprolactone) and poly(lactic acid) (PCL/PLA), a biocompatible and biodegradable scaffold with interesting mechanical (strength, flexibility) and chemical (balanced hydrophobicity/hydrophilicity) properties[220] for the realization of implantable conduits.

5.2 SCHWANN CELL DIRECTIONAL MIGRATION ALONG PDMS MICROGRATINGS

5.2.1 PDMS-membrane fabrication

Two different topographies were produced on PDMS membranes (see SECTION A.6 for details). Membranes, produced by soft lithography, are suitable for bright field microscopy and yield for highly reproducible micropatterning over macroscopic areas (1 cm², FIGURE 5.1a). Two microgratings, named $\Lambda 4_p$ and $\Lambda 20_p$, were tested (see TABLE 5.1). These gratings have a periodicity of $\Lambda = 4\,\mu m$ and $\Lambda = 20\,\mu m$, respectively, with duty cycle 0.5 (i. e. $w \equiv w_r = w_g$, see FIGURE 3.3 on page 50). The depths are $d = 0.85\,\mu m$ and $2.5\,\mu m$, respectively, as reported in TABLE 5.1. Flat PDMS membranes (FLAT) were used as a control.

The different periodicity of the gratings used resulted in different guidance regimes—namely *contact guidance* and *boundaries guidance*—on SCs. The first is distinc-

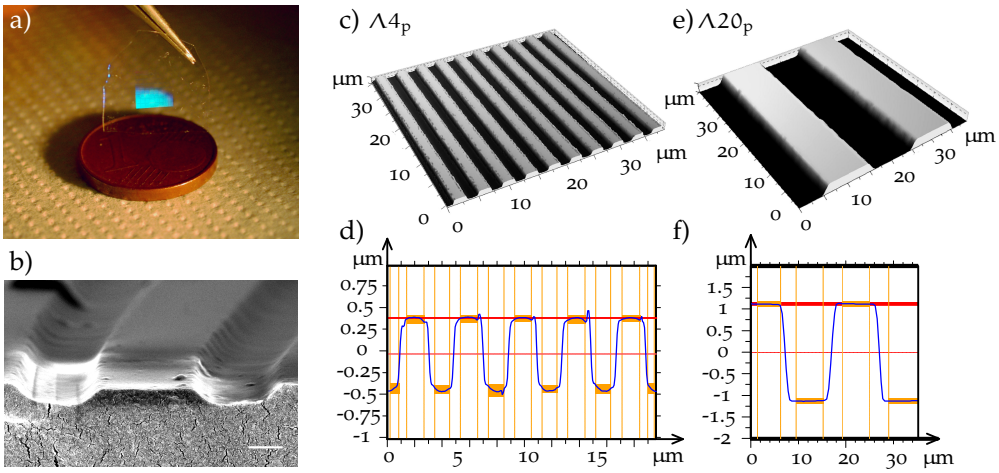

Figure 5.1: Microgratings on PDMS membranes. (a) PDMS membrane patterned with a $\Lambda 4_p$ grating (blue diffraction pattern). (b) SEM image of the cross-section of the $\Lambda 4_p$ grating. Scalebar 1 µm. (c) 3D representation of the structure of a $\Lambda 4_p$ grating and (d) profile of the grating, obtained by optical profilometry. (e) 3D representation of the structure of a $\Lambda 20_p$ grating and (f) profile of the grating, obtained by optical profilometry.

tive of gratings whose groove width is much less than cell diameter, and has been described in CHAPTER 3 and 4. The second regime characterizes the interaction between cells and structures wider than their body size. The resulting cell behavior is thus determined by physical boundaries of the grating, and whole cells can lay on ridges or inside the grooves[223]. Given that average SC body size is 250–300 µm², $\Lambda 4_p$ resulted in a contact guidance regime and $\Lambda 20_p$ in a boundary guidance regime.

5.2.2 In vitro Schwann cell migration

Substrate functionalization

Before cell culturing, the scaffold wettability was characterized by static water contact angle measurements along two different directions: parallel and perpendicular to the grating lines[217]. Overall, the membranes were hydrophobic, as expected for PDMS[224] surfaces. The patterns slightly increased the hydrophobicity, in particular along the perpendicular direction. In order to improve wettability and to allow cell adhesion and spreading, all the PDMS surfaces were chemically functionalized. As suggested by[223], functionalization was carried out by using poly-L-lysine 0.01% and laminin 50 µg/mL. To improve protein absorption, substrates were also exposed to oxygen plasma activation (see APPENDIX B.6.7) before functionalization.

Single cell migration analysis

Cell migration was acquired by time-lapse bright-field microscopy for 17 h with a time resolution of 15 min. Individual cells were manually tracked and quantitative parameters (e. g. distance from the starting point, speed, displacement) were measured as detailed in APPENDIX B.12. SCs, like other cell-types contacting similar gratings[223], were driven along the topography lines, while on FLAT substrates they showed random spatial migration (FIGURE 5.2). The total path S, calculated at 17 h, and the migration steps $\boldsymbol{dS}$ (see APPENDIX B.12 for additional details) were not affected by the presence of micropatterns, and they measured 481.5 ± 9.0 μm and 7.0 ± 0.1 μm, respectively. Interestingly, the cell displacement R on $\Lambda 20_p$ was instead significantly enhanced with respect to that of $\Lambda 4_p$ and FLAT membranes (see FIGURE 5.2g). Considering that the average cell velocity was similar for all the substrates (28.1 ± 0.5 μm/h), this improvement must originate from non-isotropic cell migration. In order to verify this hypothesis, migration data were analyzed by dividing the step vectors $\boldsymbol{dS}$ in two components: dS_{par} and dS_{per}, i. e. vectors forming an angle between 0 ° and 15 °, and between 75 ° and 90 ° with the grating lines, as sketched in FIGURE 4.14 on page 89. Random perpendicular directions were chosen for FLAT substrates. FIGURE 5.2g–i report the results of this analysis. $\Lambda 4_p$ and $\Lambda 20_p$ significantly induced cell motion directionality. In particular, 2 different effects were observed: first, both the gratings led to a significant increase of the percentage of dS_{par} with respect to the FLAT condition (FIGURE 5.2h); second, perpendicular motion was strongly inhibited on both of the gratings, that is, only 5% of the total was found within dS_{per} (FIGURE 5.2i).

These results agree with what was observed by Mitchel et al.[223]. These authors tested single SC migration along large PDMS-microgratings ($\Lambda = 30$ μm and 60 μm), but they did not report any data in the contact guidance regime (i. e. $\Lambda \ll$ cell body diameter). These results demonstrate that migration can be highly directional in both the interaction regimes, and that boundary guidance can be slightly more efficient than contact guidance. Specifically, $\Lambda 20_p$ showed a slightly stronger effect among the tested substrates.

Conclusions

Altogether, our data suggest the micrograting geometry as promising surface textures to meliorate artificial scaffolds for nerve regeneration applications, possibly improving the clinical course of patients suffering from injuries to the peripheral nervous system.

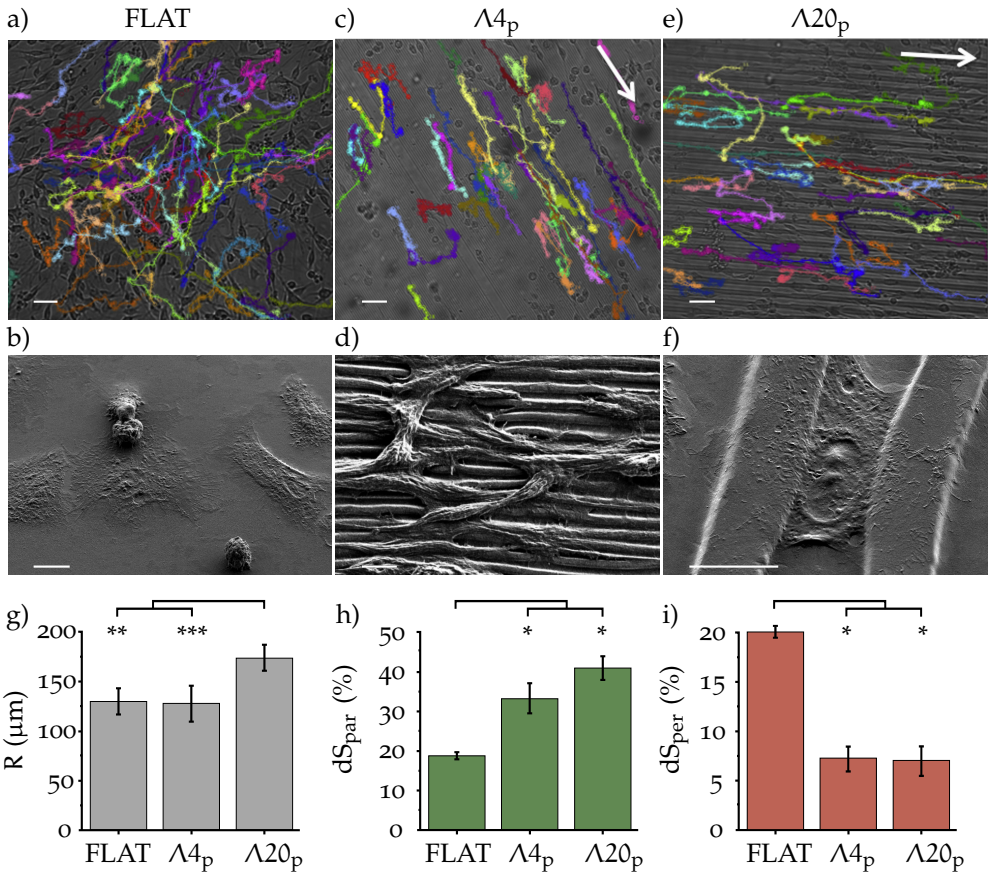

Figure 5.2: SC migration on microgratings. Representative bright-field images of cell migration on (a) FLAT, (c) $\Lambda 4_p$ and (e) $\Lambda 20_p$ PDMS substrates. White arrows represent the pattern direction. Coloured tracks were obtained by the Manual trackJ plugins of ImageJ software and they highlight SC motion. Scalebars 50 μm. Representative SEM images of SC on (b) FLAT, (d) $\Lambda 4_p$ and (f) $\Lambda 20_p$ PDMS substrates. Scalebars 10 μm. (g) Single cell displacement R after 17 h for the different substrates. (h) Percentage of cell steps ***dS*** parallel and (i) perpendicular to the pattern direction for each substrate.

5.3 IN VIVO EXPERIMENTS AND BIODEGRADABLE FILMS

5.3.1 Implantable PDMS membranes

Pilot *in vivo* experiments were conduced in collaboration with the group of Prof. Genua at the Università di Torino (Italy). Peripheral nerve regeneration was evaluated on a rat model of median nerve transection. The experimental protocol consisted of the surgical transection of a 1 cm portion of median nerve of a rat and the insertion of an artificial scaffold to bridge the severed ends (see FIGURE 5.3). The nerve was then left to regrow on the membrane and explanted after 3 or 7 days for the evaluation of the regrowth.

The thickness of the PDMS membranes was optimized using FLAT scaffolds. The best performance was achieved by membranes of $220 \pm 30\,\mu m$. Thinner membranes did not have the mechanical resistance necessary to withstand the surgery and broke during suturing to the nerve.

Experiments with FLAT membranes demonstrated that nerves can regrow on the PDMS scaffolds. FIGURE 5.3a shows a nerve explanted 7 days after the surgery, where an evident regrowth of the proximal stump on the $10\,mm \times 2\,mm$ membrane (dashed line in figure) is visible. The immunohistochemistry for neurofilament—a marker for neuronal cytoskeleton—is reported in FIGURE 5.3b and confirms that the membrane was successfully colonized by the regrowing axons of the proximal stump, even though the fibers did not seem to be highly aligned to the bridge.

These experiments also showed that the regrowing tissue did not cover both the sides of the membrane but, on the contrary, regenerated along a single side. For this reason, a protocol for the patterning of both sides of the membrane was developed (see APPENDIX A.6 for details), so that the nerve could be in contact with the micrograting independently from the side chosen for the regrowth.

The experimental protocol for the evaluation of the effect of micrograting in peripheral nerve regeneration used a bilateral surgery, implanting on one median nerve structured membrane and a FLAT one on the other. FLAT membranes were prepared with the same protocol used for the double-sided scaffolds described above, using a flat silicon wafer as mold. Even though the experiments are still ongoing, preliminary results suggest that micropatterned membranes provide a suitable environment for nerve regeneration. FIGURE 5.3e shows the early regrowth (3 days from the surgery) of a median nerve on a $\Lambda 20_p$ grating. This experiment reported a polarized outgrowth of the nerve extending between the stumps without the formation of clusters or neuroma-like structures. Further experiments are going to be performed to assess the long-term effects of the treatment, providing a more detailed

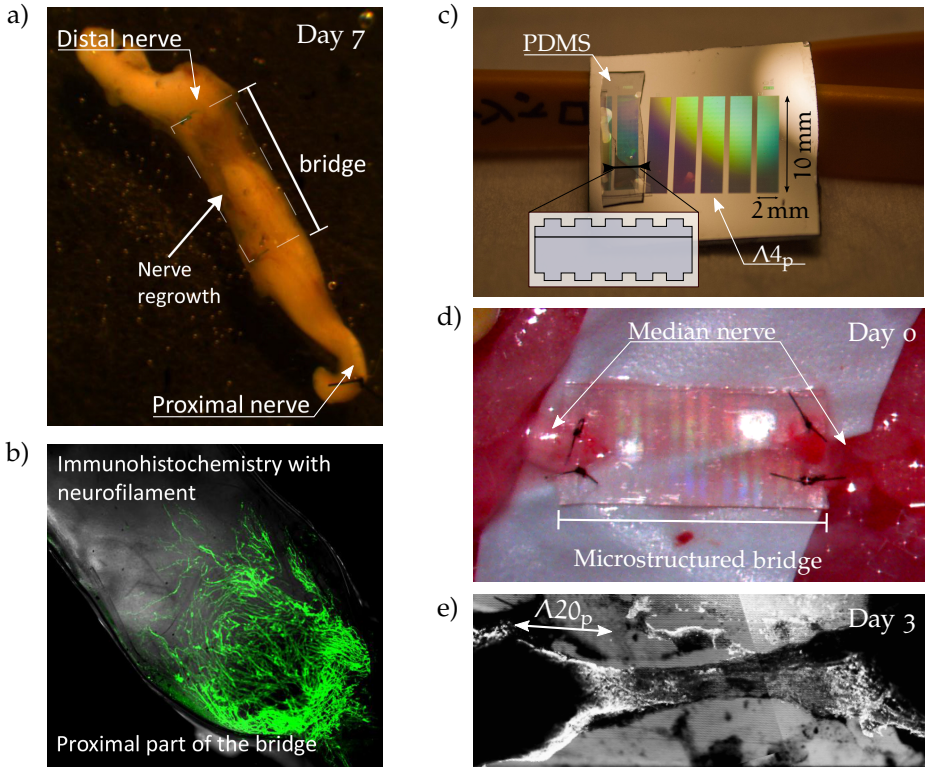

Figure 5.3: Nerve regeneration *in vivo*. (a) Median nerve regrowth (from proximal toward distal stump) on a FLAT PDMS membrane. (b) Immunohistochemistry with neurofilament, staining regrowing axons emerging from the proximal stump. (c) Microstructured mold and double-sided PDMS replica of $\Lambda 4_p$ grating. Five 2 mm × 10 mm areas are patterned on the same mold. One patterned membrane is placed on the left of the mold. The inset shows a scheme of the cross-section of the membrane (the top layer was partially removed for sake of visualization). (d) Surgery for the implant of a $\Lambda 20_p$ membrane. (e) Analysis of the early regrowth of the nerve on a $\Lambda 20_p$ membrane.

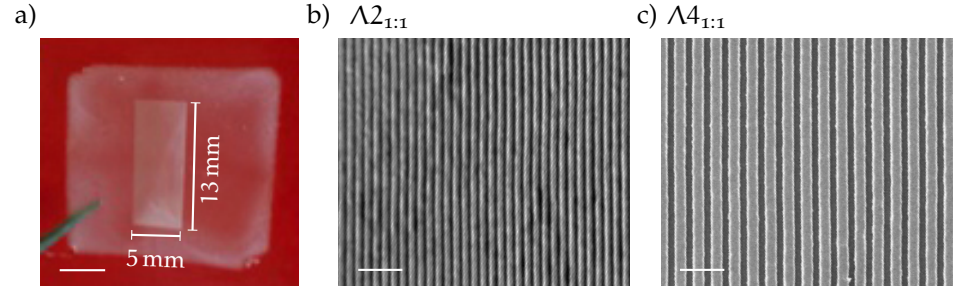

Figure 5.4: Nanogratings on PCL/PLA membranes. (a) Biodegradable PCL/PLA membrane carrying a $\Lambda 2_{1:1}$ grating. The grating is oriented along the longer side of the patterned area. Scalebar 5 mm. (b) SEM image of a $\Lambda 2_{1:1}$ grating on PCL/PLA. Scalebar 10 µm. (c) SEM image of a $\Lambda 2_{1:1}$ grating on PCL/PLA. Scalebar 10 µm

description of the interaction between regrowing nerves and microstructured membranes, and achieving a deeper insight into their possible use for clinical application.

5.3.2 Biodegradable, micropatterned scaffolds

As previously discussed, PDMS has several properties making it a suitable material for the optimization of engineered scaffolds—e. g. optical transparency, non-toxicity and compatibility with soft lithography[221,222,225]. However, the physical stability of PDMS prevents biodegradation, and can thus represent a limitation for the clinical practice, since a second surgery would be needed to remove the scaffold after the injury is healed[208]. For this reason, I worked in collaboration with the the group of Prof. Terenghi, from the School of Medicine of the University of Manchester (United Kingdom), to transfer the nanogratings onto a polymer blend based on PCL and PLA. Both these polymers are individually approved by FDA and widely used as scaffolds for tissue engineering[208,220]. The PCL/PLA blend have been optimized and tested by Terenghi et al., showing high compatibility with cell culturing and promising physical and chemical properties for the use in regenerative medicine[208,220].

Here, I will show preliminary results on transferring gratings with $\Lambda n_{1:1}$ geometry (see TABLE 3.2 on page 52) to PCL/PLA foils. Three molds with increasing periodicity and AR of 1 were fabricated as described in SECTION 3.2 (details on the process are reported in APPENDIX A.4.2). The scaffolds were produced by solvent casting: the molds were covered by a film of liquid PCL/PLA, which was left to dry until the solvent had evaporated and then was mechanically separated from the master. FIGURE 5.4 shows the results obtained using this process for the $\Lambda 2_{1:1}$ and $\Lambda 4_{1:1}$. The

Topography	Ridge-width (μm)	Groove-width (μm)	Depth (μm)
$\Lambda 2_{1:1}$	0.58 ± 0.10	0.32 ± 0.20	1.01 ± 0.10
$\Lambda 4_{1:1}$	2.41 ± 0.30	0.96 ± 0.26	2.41 ± 0.30

Table 5.2: PCL/PLA microgratings. Analysis of the gratings patterned on biodegradable PCL/PLA foils by solvent casting.

gratings were transferred onto the replica maintaining a well defined geometry over macroscopic areas (i. e. $5 \times 13\,mm^2$).

Interestingly, a reduction in the original periodicity was observed (see TABLE 5.2). This effect may be attributed to the difficulty in controlling the solvent evaporation, which could have led to a mold-replica detachment when the foils were not completely dry. This could have resulted in a residual contraction after release. Grating depth (d) was not affected by this reduction. On the contrary, a 21% increase in d was observed for the $\Lambda 4_{1:1}$ topography. $\Lambda 1_{1:1}$ grating was also tested, but the pattern on the replica presented several imperfections probably caused by an inefficient filling of the narrow grooves of the mold. Further tests will be carried out using hot embossing to imprint the micro- and nanopatterns. This protocol, exploiting the thermoplastic behavior of the PCL/PLA foils ($T_g \approx -68\,°C$), should overcome issues related to solvent evaporation and groove filling.

5.4 CONCLUSIONS

In this chapter I showed my efforts in transferring the microstructured topographies presented in CHAPTER 3 to a clinical problem, i. e. peripheral nerve regeneration. First I conducted an *in vitro* study of SC interaction with PDMS microgratings. Single cell migration patterns were monitored by time lapse microscopy, reveling that $\Lambda 20_p$ gratings were more efficient than $\Lambda 4_p$ in polarizing SC migration along the direction of the grating. Then I optimized the fabrication of double-sided PDMS micropatterned membranes for the surgical implant and tested them on a rat model of median nerve transection. Preliminary experiments suggest that such membranes could be a suitable support to guide nerve regrowth, but further experiments are needed to obtain quantitative results on their performance. Finally, in collaboration with University of Manchester, I worked on the improvement of the materials used for scaffold fabrication. The optimization of the nanograting-transfer onto an FDA approved, biodegradable polymer blend was started, resulting in the production of nanopatterned PCL/PLA foils, ready to be tested *in vitro* and *in vivo*.

6 CONCLUSIONS

In this thesis I presented results on the design and use of engineered devices for biomedical applications. My work was focused on two different aspects of artificial bio-systems: microfluidics *and* surface nano-patterning. *This chapter contains a summary of my results, my conclusions and future perspectives.*

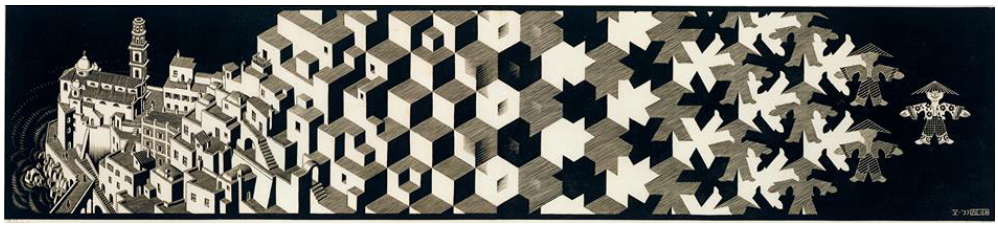

The first topic I focused on was the creation of microfluidic networks, detailed in CHAPTER 2. I developed several devices for the detection of nanoparticles and individual micrometer-sized objects, and for cell-culturing in physio-chemically controlled environments. Particular effort was dedicated to the design of a bioreactor capable of performing complex tasks while maintaining considerable ease-of-use. I believe that the progress of microfluidics has to deal with the simplification of the protocols required for chip operation. Here, I demonstrated a device that achieved automated cell loading—with the possibility to create cell co-cultures with constrained initial spatial organization—and allowed monitoring of cell behavior in chemically anisotropic environments. Importantly, device operation only required equipment already available in standard tissue culture laboratories, making it usable outside physics laboratories by researchers without specific training in microfluidics.

The second topic I presented was the use of anisotropic nanotopographies for the study of cell-contact guidance. In CHAPTER 3 I detailed the fabrication of transparent and biocompatible PET and COC scaffolds patterned with surface nanogratings. Such devices, known in literature for polarizing cell bodies and migration, were applied to the fields of orthopedics and endothelial tissue engineering. I believe that the results obtained could lead to interesting applications. In particular, human mesenchimal stromal cells (hMSCs) cultured on PET-micrograting acquired a morphology correlated with a more efficient osteogenic differentiation. Since PET is a

FDA approved material which is already used in orthopedics for the creation of artificial ligaments, we can speculate that the use of surface patterning could improve the efficiency of state-of-art prostheses through better integration with the regrowing bone. Further experiments are ongoing to understand the effective applicability of this approach.

An insight over the applicability of directional topographies *in vivo* is contained in CHAPTER 4, where I introduced an original geometry whose directional signal can be modulated by the addition of randomly distributed topographical noise. The study of cellular contact guidance on partially ordered structures allowed the collection of data that could be useful while designing implantable scaffolds, which experience a gradual deterioration owing to the accumulation of biological debris and degradation of the scaffold itself. The ability of two cell types to read partially hidden topographical stimuli was evaluated on the whole spectrum extending from a nanograting (maximum directionality) to a flat surface (isotropic environment). The loss of contact guidance induced by topographical noise was shown to be dependent on cell-contractility. A pharmaceutical strategy to modulate this phenomenon was tested on NGF-differentiated PC12 cells. Notably, increasing cell-contractility was effective in improving PC12 contact guidance, preserving neurite alignment also on topographies with low directionality.

Finally, preliminary results on the pre-clinical translation of the above described technology were presented in CHAPTER 5. In particular, I focused on peripheral nerve regeneration, exploiting surface microgratings to improve the regrowth of a severed nerve. I compared the performances of gratings with different periodicity in driving the migration of Schwann cells (SCs), a glial cell type involved in the regulation of axon regrowth during nerve regeneration. SC migration was first studied *in vitro*, then the topography showing the best performance in terms of SC directional migration was used to pattern PDMS membranes. Such membranes were used on a rat model of median nerve transection. Preliminary results suggest that short-term nerve regeneration is more efficient on directional micro-patterns than on isotropic surfaces, but additional experiments are needed to confirm this result.

In conclusion, during my Ph. D. I designed, realized and tested several micro- and nanostructured devices for biomedical applications. I worked in collaboration with researchers with disparate expertise (i. e. physicists, biologists, clinicians), trying to achieve an efficient technology transfer from nanotechnological research towards the clinical use. I do believe that these devices have the potential to achieve clinical translation in a short or medium time, contributing to the improvement of biomedical technologies.

A FABRICATION PROTOCOLS

A.1 MICROFLUIDIC DEVICES

A.1.1 Fluidic layer fabrication

Several PDMS devices were presented in CHAPTER 2 of this thesis. The fluidic layer for each device was fabricated by soft lithography using the following protocol:

- PDMS was prepared by mixing the prepolymer and the curing agent (Sylgard 184 silicone elastomer kit, Dow Corning) in a proportion of 10:1 in weight, followed by degassing by centrifugation (2 min at 1 350 g);
- the mixture was poured onto the microstructured molds and degassed again inside a desiccator until no bubbles could be seen ($\approx$ 15 min);
- the mixture was then baked at 80 °C for 3 h;
- finally, the cured PDMS was removed from the mold with a scalpel, and access-holes were created using Harris Uni-Core punchers.

A.1.2 PDMS bonding protocols

Different techniques were used to seal the fluidic layer depending on the substrate used as a sealing layer.

Glass bonding

PDMS was irreversibly bonded to glass by oxygen plasma activation:

- glass was exposed to oxygen plasma (100 W, $1.4 \cdot 10^{-1}$ mbar) for 1 min;
- PDMS was exposed to oxygen plasma (10 W, $1.4 \cdot 10^{-1}$ mbar) for 25 s;
- the two surfaces were brought in conformal contact, placed at 70 °C for 1 h and then left to rest at room temperature overnight.

COC bonding

A heterogeneous bonding protocol was used to obtain an irreversible bond between COC and PDMS, as reported in reference [226]:

- PDMS and COC foils were exposed to oxygen plasma ($1.4 \cdot 10^{-1}$ mbar, 10 W) for 25 s and 15 s, respectively;
- PDMS and COC were then immersed for 20 min in a 1% (3-aminopropyl)triethoxysilane (APTES) aqueous solution and in water, respectively;
- the substrates were then carefully dried with nitrogen flow and brought into conformal contact at room temperature. An irreversible bond formed after approximately 1 h.

Metal bonding

The bonding technique employed to join the metalized surface with the soft PDMS fluidic layer used an interlayer of UV cured SU8 (MicroChem) as a glue layer between the metal and the PDMS fluidic layer according to the following protocol:

- clean the metalized surface with acetone and isopropanol;
- spin-coat the SU8 adhesion promoter Omnicoat (Microchem) on the surface for 10 s at 500 rpm and 30 s at 3 000 rpm;
- spin-coat SU8 2000.5 (Microchem) for 30 s at 2 000 rpm;
- before solvent evaporation, bond on plasma-treated PDMS fluidic layer;
- wait for 2 second, then soft-bake for 1 min at 65 °C and 2 min at 95 °C;
- UV expose;
- store for 2 min at 95 °C and then wait overnight before pressurization.

Maximum pressure resistance of the bonded device was not tested. During the experiments the maximum operating pressure used was 30 psi.

A.2 MOLDS FOR PDMS SOFT LITHOGRAPHY

The molds were fabricated by standard UV lithography on silicon wafers using the following protocols:

A.2.1 LC nanoresonators detection

The mold for the microfluidic device used in SECTION 2.3.2 was fabricated using the following protocol:

- photoresist AZ9260 (MicroChem) was spin-coated on the silicon wafer for 30 s at 1 500 rpm and softbaked on a hotplate for 80 s at 110 °C;
- a second layer of AZ9260 was deposited over the first layer using the same spincoating parameters and the sample was soft-baked for 180 s at 115 °C, obtaining a single photoresist layer 30 µm thick;
- the channels were patterned by UV lithography with a Suss MJB4 mask aligner (Suss, MicroTec) exposing the AZ9260 for 113 s at a constant light intensity of 15 mW/cm²;
- the sample was developed for 4 min in a 1:3 solution of AZ 400K (MicroChem) in water, using DI-H_2O water to stop the development;
- the mold was then placed on a hotplate for 2 min at 110 °C;
- finally, the mold was exposed to vapours of chlorotrimethylsilane (Sigma Aldrich) for 15 min, in order to facilitate the master-replica detachment.

A.2.2 Photoacoustic phantom

The mold for the microfluidic device used in SECTION 2.3.3 was fabricated using the following protocol:

- the photoresist SU8 2075 (MicroChem) was spin-coated with a 2-step protocol, first for 10 s at 500 rpm and then for 1 min at 3 000 rpm;
- the sample was soft-baked on a hotplate with a temperature ramp from 65 °C and 95 °C, followed by 8 min at 95 °C;
- the channels were patterned by UV lithography with a Suss MJB4 mask aligner (Suss, MicroTec), exposing the SU8 for 5 s at 9 mW/cm²;
- the sample was post-baked on a hotplate for 7 min at 95 °C and developed for 3.5 min in SU8 Developer (MicroChem), using isopropanol to stop the development;
- the sample was hard-baked on a hotplate by means of a temperature ramp from 65 °C to 200 °C, followed by 10 min at 200 °C and a ramp down to 95 °C;

- finally, the mold was exposed to vapours of chlorotrimethylsilane (Sigma Aldrich) for 15 min, in order to facilitate the master-replica detachment.

A.2.3 Chip for anisotropic cell culturing

The microfluidic device reported in SECTION 2.4 was fabricated using a bilayered SU8 structure. This mold was obtained by a combination of EBL and UV lithography. First, gold (Au) markers were deposited by lift-off on the silicon wafer, and used for the alignment of the 2 SU8 layers:

- S1818 (Microposit) was spin-coated for 1 min at 6 000 rpm on a silicon wafer, and soft-baked for 1 min at 90 °C;
- the sample was exposed for 3.5 s at 15 mW using a Suss MJB4 mask aligner (Suss, MicroTec) and developed for 30 s with MF 319 (Microposit), using DI-H_2O water to stop the development;
- 100 nm-Au was evaporated on the sample (KJL thermal evaporator), which was subsequently immersed in hot acetone (50 °C) for 2 h to dissolve the S1818;
- the excess of Au was mechanically removed by flushing with acetone from a syringe;
- a first layer of SU8 2002 was spin-coated on the sample for 1 min at 1 000 rpm and soft-baked using a hotplate for 2 min at 95 °C;
- the 2.5 µm-thick channels (FCs) were exposed by EBL (20 keV, 1.25 µC/cm²);
- a second layer of SU8 2025 was spin-coated for 2 min at 3 000 rpm over the EBL-exposed layer;
- the sample was baked on a hotplate for 2 min at 65 °C and for 5 min at 95 °C (a temperature ramp was applied between the two baking-points);
- the 20 µm-thick channels were exposed by UV lithography using a Suss MJB4 mask aligner (10 s at 15 mW/cm²);
- the SU8-bilayer was post-baked for 1 min at 65 °C and 5 min at 95 °C (a temperature ramp was applied between the two baking-points), then temperature was ramped down to 65 °C;
- the sample was developed for 2.5 min in SU8 Developer (All resist, GmbH), using isopropanol to stop the development;

- the mold was hard-baked on a hotplate by means of a temperature ramp from 65 °C to 200 °C, followed by 10 min at 200 °C and a second ramp down to 95 °C;
- finally, the mold was exposed to vapours of chlorotrimethylsilane (Sigma Aldrich) for 15 min, in order to facilitate the master-replica detachment.

A.3 GOLD NANORODS FABRICATION

The gold nanorods (GNRs) presented in SECTION 2.3.3 were produced by the group of Dr. Ratto as described in detail in reference[79]. Briefly:

- the GNRs were fabricated by autocatalytic reduction of chloroauric acid using ascorbic acid in combination with cetrimonium bromide, silver nitrate and gold nuclei;
- the nanoparticles were grafted with poly (ethylene glicol) (PEG) in a 100 mM acetate buffer (pH 5.0) containing 50 μM alpha mercapto omega methoxy PEG strands (molecular weight of 5000 g/mol);
- finally, the particles were transferred into ultrapure water at a nominal concentration of 20 mM Au (116 nM nanoparticles).

A.4 MOLDS FOR HOT EMBOSSING

The silicon molds used for the hot embossing processes were fabricated by a combination of EBL and RIE. Different protocols were used depending on the specific geometry.

A.4.1 Constant-depth molds

- PMMA (AR-P 679.04, Allresist) was spin-coated for 1 min at 3 000 rpm and soft-baked for 15 min at 120 °C on a hotplate;
- the sample was exposed by EBL (30 keV, 320 μC/cm²) and developed for 2.5 min in AR 600 − 56 (Allresist), using isopropanol to stop the development;
- a descum was performed by a 2 min oxygen plasma treatment ($2.5 \cdot 10^{-1}$ mbar, 20 W);

- the nanopatterns were transferred on silicon by means of a RIE process of 80 s at 50 W in a 20:3 atmosphere of SF_6 and Ar ($2.98 \pm 0.06 \cdot 10^{-2}$ mbar, 65 ± 1 V);
- the leftovers of the PMMA mask were removed using hot acetone (50 °C), and oxygen plasma (5 min, 100 W, $2.5 \cdot 10^{-1}$ mbar);
- finally, the molds were immersed for 30 min in Silanization solution I (dimethyldichlorosilane in heptane, Sigma Aldrich) in order to obtain low-energy surfaces, easing the master-replica detachment (followed by a 10 min wash in hexane and 1-octanol).

A.4.2 Constant-AR molds

- first, a 100 nm-thick layer of aluminum (Al) was evaporated on the silicon wafers using a KJL thermal evaporator;
- AR 300.80 (Allresist) was spin-coated for 1 min at 4 000 rpm and soft-baked for 5 min at 120 °C on a hotplate;
- ma-N 2403 (Micro resist technology) was then spin-coated for 1 min at 6 000 rpm and soft-baked for 1 min at 90 °C on a hotplate;
- the nanogratings were exposed by EBL (10 keV, 16.5 μC/cm²);
- the samples were developed for 60 s in ma-D 525 (Micro resist technology), using DI-H_2O to stop the development;
- descum was performed by a 1 min oxygen plasma (50 sccm O_2, 10 W);
- the nanogratings were transferred onto the Al layer by means of an ICP-RIE process using a 5:4:3 atmosphere of Cl_2, BCl_3 and Ar (5 min);
- the remaining ma-N 2403 was removed by an oxygen plasma treatment (5 min, 80 sccm O_2, 50 W);
- the nanogratings were transferred onto the silicon by using an RIE process employing at 220 W in a 5:1 atmosphere of O_2 and SF_6 ($1.01 \pm 0.01 \cdot 10^{-1}$ mbar, 530 ± 9 V);
- the Al mask was removed by ICP-RIE (5:4:3 Cl_2:BCl_3:Ar, 5 min);
- finally, the molds were immersed for 30 min in Silanization solution I (dimethyldichlorosilane in heptane, Sigma Aldrich) in order to obtain low-energy surfaces, easing the master-replica detachment (10 min wash in hexane and 1-octanol).

A.5 HOT EMBOSSING

The hot embossing process was performed with an Obducat Nanoimprint 24 system (Obducat, Sweden) with the following protocols:

A.5.1 PET

- a film of PET was placed on top of the mold and softened by raising the temperature up to 75 °C ($\approx T_g^{PET}$),
- pressure (20 bar) was then applied for 5 min,
- samples were cooled down to 50 °C,
- pressure was released.

A.5.2 COC

- a film of COC was placed on top of the mold and softened by raising the temperature up to 150 °C ($T_g^{COC} \approx$ 134 °C),
- pressure (50 bar) was then applied for 5 min,
- samples were cooled down to 70 °C,
- pressure was released.

After the hot embossing cycle, replicas were detached from the molds with the help of tweezers and a scalpel. The imprinted foils were carefully attached to the bottom of hollowed 35 mm WillCo dishes by using a silicone glue (RS Components RS692 – 524).

A.6 PDMS SCAFFOLD FABRICATION

The PDMS membranes reported in SECTION 5.2.1 were prepared using a 10:1 (in weight) mixture of PDMS:curing agent as described in APPENDIX A.1.1. Then, the following protocol was applied:

- the PDMS mixture was poured onto the microstructured molds and spin-coated for 4 min at 500 rpm;

- the sample was left resting for 10 min in order to reduce the surface inhomogeneity and baked for 10 min at 80 °C;
- the membrane was removed with a scalpel and the mold was cleaned of PDMS residuals.

A.6.1 Double sided membranes

- the first layer was created by spin-coating the mixture over the mold for 4 min at 300 rpm, leaving it to rest for 5 min and baking it for 10 min at 80 °C;
- the membrane was removed with a scalpel and the mold was cleaned of PDMS residuals;
- the second layer was created by spincoating the mixture over the mold for 2 min at 1000 rpm, leaving it rest for 5 min and baking for 10 min at 80 °C;
- both the PDMS membranes were activated by an oxygen plasma treatment of 15 s, 10 W, 1.4×10^{-1} mbar and immediately brought in contact. The alignment was performed free-hand with the help of a mask aligner (Suss MJB4, MicroTec);
- the sample was placed for 1 h at 80 °C to ease the bonding between the PDMS layers, then the membrane was removed from the mold with a scalpel.

B PROTOCOLS AND METHODS

B.1 TERAHERTZ SETUP

The optical setup introduced in SECTION 2.3.1 is described in detail in reference[57]. Briefly, a 2.6-THz QCL source was cooled down to the operating temperature of 30 K with a compact Sterling cryostat (RICOR). It was driven with 800 mA pulses at a duty-cycle of 10%, resulting in a few mW of average output power. The hi-divergence laser radiation was emitted through a polyethylene window and collected and focused using two f/1 Picarin lenses. The smallest spot obtained was approximately 200 μm in diameter. The focal point corresponded to the position where the plasmonic antenna was positioned. From this point the radiation was collected by a gold-plated 50 mm parabolic mirror (NA ≈ 0.447) and then focused onto the detector through another parabolic mirror. The THz sensor employed was a silicon bolometer operating at liquid helium temperature (4 K) connected to a lock-in amplifier. The antenna alignment was carried out by fixing the chip on a sample holder connected to a XYZ motorized stage and maximizing the transmitted signal by moving the stage. The setup also contained a CCD camera (for visible light) with a 10× microscope objective. The center position of the field of view of the CCD was at a calibrated distance from the position of the THz focus. The camera was used as an easy-alignment system and also gave information on particle flow in the channel before the THz measurement.

B.2 STICS MEASUREMENTS

The velocity fields shown in SECTION 2.4 were measured via spatio-temporal image correlation spectroscopy (STICS) using a standard inverted microscope (Nikon Eclipse Ti) equipped with a fast camera (Basler A602-f). The device was filled with a suspension of 500 nm latex beads (Sigma Aldrich L3280 diluted 1:10 in water) and a time series of 300 bright-field images of the entire MC was acquired at 30 fps with an air 10× NA = 0.45 objective and a 1.5× lens (1.07 μm/pixel).

Active pressurization measurements were performed after seeding the fluid with 100 nm particles (Sigma Aldrich L9902). In order to further reduce microchannel

clogging at these high flow rates, the suspension (diluted 1:5 in water) was filtered using a membrane with 0.22 μm pores (Millipore Millex-GP Filter unit) prior to experiments. A 6 000 frame time series was acquired in bright-field microscopy at 400 fps with an air 20× NA = 0.45 objective and a 1.5× lens (0.53 μm per pixel).

Calculations were carried out in the hydrostatic regime on a square grid of points separated by 8 μm using 16 μm wide interrogation areas, while for the active pressurization measurements both the pitch of the grid and the size of the interrogation areas were increased to 30 μm to increase the signal-to-noise ratio.

B.3 SHEAR-STRESS CALCULATION IN MC

The shear-stress experienced by cells in each point of the MC (see SECTION 2.4.2) was calculated from the velocity field measured by STICS, by summing the components of the stress tensor related to the shear forces:

$$\sigma(x,y,z) = \sigma_{xy}(x,y,z) + \sigma_{yz}(x,y,z) + \sigma_{xz}(x,y,z),$$

which, according to EQUATION (2.9), can be written as

$$\begin{aligned}\sigma &= \eta\Big[\big(\partial_y v_x + \partial_x v_y\big) + \big(\partial_z v_y + \partial_y v_z\big) + \big(\partial_z v_x + \partial_x v_z\big)\Big] \\ &= \eta\Big[\big(\partial_y v_x + \partial_x v_y\big) + \partial_z\big(v_y + v_x\big)\Big],\end{aligned} \tag{B.1}$$

where we assumed $v_z = 0$ for the symmetry conditions applicable to microchannels with constant h (see SECTION 2.1.1). EQUATION (B.1) can be further simplified assuming that

- the STICS measures were performed focusing the microscope at $z = 2.5\,\mu m$ from the bottom of the MC,
- the fluid velocity field near the substrate ($0 < z < 2.5\mu m$) varies linearly with z, as shown in simulations, showing that the linear approximation introduces an error lower than 1%[227].

Under this conditions, $\partial_z \boldsymbol{v} = \boldsymbol{v}|_{z=\Delta z}/\Delta z$, where $\boldsymbol{v}$ is the velocity measured by STICS at a distance Δz from the bottom of the MC. EQUATION (B.1) thus becomes

$$\sigma = \eta\Big[\big(\partial_y v_x + \partial_x v_y\big) + \big(v_y + v_x\big)/\Delta z\Big], \tag{B.2}$$

which can be calculated point-to-point to produce a stress-map in the MC. The average shear-stress in the MC can therefore be easily calculated from EQUATION (B.2).

B.4 DIRECTIONALITY CALCULATION

Substrate directionality is calculated using the FT of the virtual images of the nanopatterns. Briefly:

- a matrix with a spatial resolution of 166 nm (corresponding to a spatial sampling frequency of $6\,\mu m^{-1}$) was created;
- each element of the matrix was set to 1 or 0 depending from the noise map associated to the pattern (see FIGURE 4.1 on page 69);
- a random number was added to each point in order to emulate a surface roughness equal to 6% of NG-depth (d). This number was generated by the rand function of Matlab and was a pseudorandom scalar from the standard uniform distribution in the interval $[0, 0.06]\,/d$;
- the Fourier transform (FT) of these matrices was calculated by using the fft2 function of Matlab. The frequency resolution is set to $2.92 \cdot 10^{-3}\,\mu m^{-1}$ by applying a zero-padding to the input geometries;
- nanopattern directionality $\delta(p, A)$ was finally calculated using EQUATION (4.1) on page 71.

Signal bands (B_S) were defined as the FWHM signal peak for the non-noisy NG (see FIGURE 4.2 on page 71). This band was centered in $f_x = 1\,\mu m^{-1}$, $f_y = 0\,\mu m^{-1}$ and its width varied from $0.1\,\mu m^{-1}$ for $A = 6 \times 6\,\mu m^2$ to $0.005\,\mu m^{-1}$ for $A = 160 \times 160\,\mu m^2$. Since the frequency distribution of noise does not change with A, B_N was centered in $f_x = 0\,\mu m^{-1}$, $f_y = 0\,\mu m^{-1}$ and had a radius of $0.8\,\mu m^{-1}$ for every A. Due to the symmetry of the FT, only the $f_x \geqslant 0$ spectrum was used for the calculation of δ.

B.5 MICROCHAMBER FILLING AND AUTOMATED CELL LOADING

The reproducible and reliable filling of the microfluidic network shown in SECTION 2.4 was obtained by degassing the whole chip at $4 \cdot 10^{-2}$ mbar for 10 min, sterilizing by oxygen plasma treatment (60 s, $1.4 \cdot 10^{-1}$ mbar, 10 W) just before LR filling and immediately moving into the incubator (37 °C, 95% humidity, 5% CO_2). The absorption of air into degassed PDMS was used to fill the channels and, at the same time, it prevented bubble formation during the heating of the device. The whole process was achieved in approximately 20 min.

Before cell loading, the chips were filled with DMEM and incubated for 1 h. Cells were harvested and diluted at a concentration of $3 \cdot 10^5$ cells/mL. The volume used for LR-filling depended on the shape of the LR used. In the experiments reported in SECTION 2.4, 450 µL or 200 µL reservoirs were used. The change in volume did not change column height used in the experiments, i. e. both input pressure (150 Pa) did not change.

Symmetric loading

In order to obtain symmetric cell loading, the reservoirs were emptied of DMEM and the LR_C was filled with cell suspension (*symmetric loading*, see TABLE 2.3 on page 34) at the concentration indicated above. After 30 min, the LR_C was emptied and perfusion was restored by adding fresh DMEM into the $LR_{A,B}$.

Asymmetric loading

Asymmetric loading was obtained by the same protocol with the exception of removing the liquid from only one of the two lateral LRs before adding the cell suspension into the LR_C (*asymmetric loading*, see TABLE 2.3 on page 34).

B.6 CELL CULTURING PROTOCOLS

B.6.1 HeLa cell culturing

HeLa cells were obtained from American Type Culture Collection (ATCC, Rockville, Maryland). HeLa cells were grown in a complete culture medium consisting of DMEM supplemented with 2 mM L-glutamine, 100 IU/mL penicillin, 100 µg/mL streptomycin, and 10% heat-inactivated fetal bovine serum (FBS) (Gibco, Invitrogen). Cells were detached by trypsinization, counted in a Thoma's camera and suspended in cell culture medium at a concentration of $3 \cdot 10^5$ cells/mL prior to cell loading in the microfluidic device.

B.6.2 REF culturing

REF52 cells (a rat fibroblast line) stably expressing paxillin-YFP were obtained from Prof. Joachim Spatz (Max-Planck Institute for Metals Research, Stuttgart, Germany). Cells were grown in a complete culture medium consisting of DMEM supplemented

with 2 mM L-glutamine, 100 IU/mL penicillin, 100 µg/mL streptomycin, and 10% heat-inactivated FBS (Gibco, Invitrogen).

Cells were detached by trypsinization, counted in a Thoma's camera and suspended in cell culture medium at a concentration of $3 \cdot 10^5$ cells/mL prior to cell loading in the microfluidic device.

B.6.3 hMSC isolation, culturing and immunostaining

hMSC were isolated as described in ref[228]. Briefly, human bone marrow samples were obtained from patients undergoing hip replacement. Mononuclear cells were then isolated and cultured under standard conditions, using DMEM (Invitrogen, Carlsband CA-USA) supplemented with 10% FBS (Invitrogen), 100 µg/ml gentamicin (Sigma Aldrich), 2 mM L-Glutamine (Invitrogen). The attached cells were then grown at 37 °C in a humidified atmosphere containing 5% CO_2. Cultured hMSCs were detached by trypsin digestion and characterized by incubation with anti-CD105 FITC-conjugated, anti-HLA-DR PE conjugated and anti-CD90 PE-Cy5-conjugated (all antibodies were purchased from BD Bioscience, San Jose, CA), acquired by a flow cytometry analyzer (FACScan, BD Bioscience), and analyzed using CellQuest analysis software (BD Bioscience).

Immunostaining

Cells were fixed in 4% paraformaldehyde and then immunostained with anti-β Tubulin III antibody (3 ng/mL, Sigma Aldrich) and phalloidin-Alexa Fluor 647 (0.17 µM, Invitrogen) in permeabilization buffer (2% gelatin, Triton X-100, NaCl, PBS). Samples were then washed, incubated with Alexa Fluor 488-secondary antibody (0.02 mg/mL, Invitrogen) and mounted with Fluoroshield (Sigma Aldrich) with DAPI for nucleus detection.

B.6.4 hUVEC culturing

Human umbilical-vein endothelial cell (hUVEC) (Invitrogen) were grown in medium 200PRF supplemented with fetal bovine serum 2% v/v, hydrocortisone 1 mg/mL, human epidermal growth factor 10 ng/mL, basic fibroblast growth factor 3 ng/mL and heparin 10 mg/mL (all reagents from Invitrogen) and were maintained at 37 °C and 5% CO_2. All experiments were performed using cells with less than seven passages *in vitro*.

Before cell-seeding, the textured COC substrates were incubated with 1.5% Gelatin (DIFCO 214340) in DI-H_2O for 1h at room temperature. Then, Gelatin was fixed

using 2% glutaraldehyde in DI-H_2O for 15 min at room temperature. After fixation glutaraldehyde was exchanged with 70% ethanol in PBS and incubated for 60 min at room temperature. Next, gelatin-coated substrates were washed 5 times with PBS and stored overnight in a PBS solution containing 2 mM glycine. Finally, the samples were washed in sterile PBS and stored at 4 °C until the seeding of hUVECs.

To generate confluent monolayers, cells were seeded on COC substrates at high density ($6–7 \cdot 10^5$ cells/cm²) as reported by Lampugnani et al.[229] and cultured for two days.

Immunostaining

Mouse anti-vinculin (V4505) and mouse anti-tubulin (T6074) were purchased from Sigma Aldrich. Phalloidin-Alexa 647 (V22886) was purchased from Invitrogen. Secondary goat anti-mouse Alexa 488 was purchased from Sigma Aldrich. Paxillin-EGFP was kindly provided by Juergen Wehland (Helmholtz Centre for Infection Research, Braunschweig, Germany).

B.6.5 PC12 culturing, differentiation and contractility modulation

Cell culturing

PC12 cells (CRL-17210, ATCC) were grown in RPMI medium supplemented with 10% horse serum (HS), 5% FBS, 2 mM glutamine, 10 U/mL penicillin and 10 mg/mL streptomycin and were maintained in standard conditions (37 °C, 95% humidity, 5% CO_2). Cells (within the 16^{th} passage) were cultured until sub-confluence, then harvested for cell tests, pipetted to obtain a single cell suspension (through a 10 mL syringe with G21 needle), and seeded onto the imprinted dishes at a final concentration of 10^4 cells/cm². Before cell culturing, the imprinted dishes were sterilized by treatment with ethanol and then rinsed twice with DI-H_2O.

Neuronal differentiation

Neuronal differentiation was induced by treatment with NGF, 100 ng/mL. PC12 cells were allowed to adhere for $8 – 12$ h before stimulation with NGF.

Contractility modulation

For contractility inhibition experiments during PC12 differentiation, the cells were treated with nocodazole (methyl-[5-(2-thienylcarbonyl)-1H-benzimidazol-2-yl]-carbamate $10 – 25$ nM in DMSO) or blebbistatin (1-phenyl-1,2,3,4-tetrahydro-4-hydroxpyrrolo[2,3-b]-7-methylquinolin-4-one 25 mM in DMSO). DMSO concentration never ex-

ceeded 0.5% v/v and the corresponding solvent concentration was added to the untreated condition. Nocodazole, a microtubule destabilizer, was added after 6 h from NGF treatment, while blebbistatin, an inhibitor of myosin-II, was added 30 min before NGF stimulation (and repeated every 24 h).

B.6.6 WJ-hMSC extraction, culturing and immunostaining

Extraction and culturing

WJ-hMSC were isolated from umbilical cords from full-term deliveries, which were collected at the Gynaecology Unit of the Azienda Ospedaliera Universitaria (Pisa). Wharton's jelly (WJ) was separated from the cord vessels and placed in 6-well dishes containing alpha-minimum essential medium (a-MEM; GIBCO) supplemented with 20% FBS (Euroclone, Italy) and incubated at 37 °C with 5% humidified CO_2. Fresh medium was added twice a week up to 90% confluence. WJ-hMSC were then harvested with 0.25% trypsin and 1 mM EDTA solution (Cambrex, Italy) and re-plated at 8 000 cells/cm². Successive passages were performed in DMEM medium supplemented with 10% FBS, 2 mM L-glutamine, 10 U/mL penicillin and 10 mg/mL streptomycin.

The expanded cells were characterized after the primoculture (P0) by flow cytometric analysis (FACS Canto I, Becton Dickinson CA, USA) of specific surface antigens (CD142, CD342, CD202, CD452, CD731, CD901 and CD1051) according to the mesenchymal immunophenotype. Cells were used within the 8^{th} passage. In order to perform single-cell experiments, WJ-hMSC were seeded at the final concentration of $3 \cdot 10^5$ cells/cm² and kept in humidified atmosphere until experiment time.

Immunostaining

24 h after seeding, cells were fixed by a 15 min treatment with 4% paraformaldehyde and rinsed 3 times with PBS. Cells were permeabilized and stained at 4 °C overnight with 0.165 mM Alexa Fluor 647-phalloidin (Invitrogen) and the primary antibody 2.5 mg/mL, 0.5% Triton, 0.8 M NaCl, 30 mM phosphate buffer. Cells were washed and incubated at room temperature for 45 min in 20 mg/mL secondary antibody Alexa Fluor 488 diluted in GDB solution. Nuclei were labeled with 5 mg/mL of Hoecst (Invitrogen) in PBS.

B.6.7 SC extraction and culturing

Primary SC culture was established from sciatic nerves of adult Wistar rats. Nerves were removed and incubated in culture for 2 weeks: then the tissues were dissociated

and cultured in the presence of glial growth factor (63 ng/mL) and forskolin (10 μM) in DMEM supplemented with 10% FBS, 4 mM L-glutamine, and antibiotics. Cells were routinely immunodepleted by anti-rat Thy1.1 antibody to enrich the culture in SCs and reduce the presence of fibroblasts. SCs were maintained in standard tissue culture plates functionalized by poly-D-lysine (100 mg/mL).

The PDMS membranes required functionalization in order to facilitate cell adhesion. The membranes were exposed to oxygen plasma (15 s, 10 W, 1.4×10^{-1} mbar) to improve protein absorption, and coated with poly-L-lysine and laminin, 0.01% (at room temperature) and 50 μg/mL (at 37 °C) respectively, for 30 min. SCs were seeded on the functionalized PDMS membranes to perform single cell migration experiments at concentrations of $8 \cdot 10^4$ cells/cm².

B.7 CELL VIABILITY ASSESSMENT

Cell viability was evaluated by simultaneous labeling with Calcein AM (5 μM, Invitrogen), PI (8 μg/ml, Sigma Aldrich) and Hoechst (5 μg/ml, Invitrogen) at 24 and/or 72 h after seeding. Viability and necrosis were evaluated as percentage of Calcein AM and PI positive cells, respectively. Apoptosis was quantified as a percentage of cells with pyknotic nuclei.

B.8 EGFP–PAXILLIN TRANSFECTION

PC12 cells were transfected with EGFP-Paxillin construct by electroporation, as previously reported [140]. EGFP-Paxillin was a kind gift from Juergen Wehland (Helmholtz Centre for Infection Research, Braunschweig, Germany). Cells were imaged after 24 h from transfection (and $>$ 12 h from NGF administration).

B.9 MICROSCOPY

B.9.1 Bright-field and epifluorescence microscopy

Living-cell imaging was performed using an inverted Nikon-Ti Eclipse microscope (Nikon, Japan) and a CCD ORCA R2 (Hamamatsu, Japan). The textured substrates were examined while maintained in an incubated chamber coupled to the microscope (Okolab, Italy). Cell images were collected using an air 20× 0.45 NA (Plan-

Fluor, Nikon), an oil immersion 40× 1.30 NA objective (PlanFluor, Nikon) or an oil immersion 60× 1.40 NA objective (PlanFluor, Nikon). In particular:

- HeLa cell loading in the microfluidic chamber and doubling time were analyzed by means of bright-field microscopy (20× objective);
- for REF and HeLa cocultures, epifluorescence microscopy (60× objective) was used. The full area of the microfluidic chamber was acquired by using the stitching option of the Nikon imaging software (NIS Elements);
- for hUVECs morphometric analysis, single-cell images were collected with the 20× objective;
- for PC12 differentiation experiments, at least 15 transmission images (40× objective) were acquired for each specimen;
- for WJ-hMSC and SC migration analysis, 3 independent time-lapse experiments were performed in epifluorescence (20× objective) with a perfect focus systems. Images were acquired for 15 and 17 h, respectively, with sampling time of 15 min.

B.9.2 TIRF microscopy

TIRF imaging was performed using an inverted Leica AF6000 microscope with an oil immersion 100× 1.46 NA TIRF objective. For each region, 2 bright-field (focused on the cell and on the nanostructure), an epifluorescence and a TIRF (100 nm-depth) images were acquired.

B.9.3 Confocal microscopy

Fixed and stained cells were mounted in Vectashield (VectorLaboratories, USA) and imaged using a confocal microscope (TCS SP5 and SP2 AOBS, Leica Confocal Microscopy, Germany) equipped with Ar (emission 488 nm, detection 495–550 nm), He/Ne (emission 633 nm, detection 650–800 nm) and UV (emission 405 nm, detection 410–470 nm) lasers with an oil immersion 40× 1.25 NA objective. The image size was 1 024 × 1 024 pixels.

B.10 MORPHOMETRICAL ANALYSIS

B.10.1 Neurite alignment

Neurites of differentiated PC12 cells were semi-automatically segmented (from the point of origin at the perimeter of the cell body to the tip of the neurite growth cone) using NeuronJ, a plugin of ImageJ (National Institute of Health, USA) designed for neurite tracking. The presence of neurites was evaluated and the alignment quantified by measuring the angle of each neurite with the direction of the NG (or with a randomly chosen direction for cells on FLAT substrate). Only protrusions originating from the cell body and longer than 10 μm (about one average cell body diameter) were counted as neurites. Only neurites which terminated in a free end or with growth cones cleanly abutting neighboring cells were considered.

A file containing the tracks was exported and loaded in Matlab (MathWorks) where a custom script calculated the neurite length ℓ (the distance of the traced neurite path) and alignment α_n (measured by approximating the neurite as a straight line from the initial to end point and taking the angle of this line versus the NG orientation), for each time point.

B.10.2 Cell-body and nuclear alignment to NGs

Cell morphology was evaluated by using the ImageJ software (National Institute of Health, USA), by a free-hand selection of the cell contours. The measured cell parameters were: feret and min feret, which are the maximum and minimum distance between two parallel lines tangential to the region of interest borderline (respectively), cell area, cell alignment (defined as the absolute value of the difference between the NG lines and the feret direction).

Nuclear morphology and position were also measured. Nuclei were segmented using the measure tool (with the elliptic fit option) on the free-hand contour of the nuclei. The following parameters were extracted: feret and min feret, area, alignment, Δx and Δy (which measure the nuclear-centroid position with respect to the cell centroid).

B.10.3 Cytoskeletal alignment

Actin and tubulin fiber alignment to NGs in individual cells was measured using the directionality tool of ImageJ.

This plugin calculated a *directionality histogram* by exploiting image FFT algorithms: an anisotropic filter was applied to the image FFT and rotated between 0

and 180 °, with increments of 2 °, to calculate the amount of signal associated to each direction. Note that isotropic images generate a flat histogram, whereas oriented images give a peaked histogram. Finally, the plugin calculates a Gaussian fit on such histograms and returns 2 parameters: *dispersion* and *directionality* (the SD and the mean of the Gaussian curve, respectively). The first indicates how anisotropic is the image, the second represents the direction in which it is oriented. Cytoskeletal alignment to the NG was calculated as the difference between the direction of the grating and the *directionality* value. Given the symmetry of the NG, cytoskeletal alignment could be defined between 0 and 90 °. Average alignment angles of 0 and 45 ° indicate perfect and random alignment, respectively. Samples were considered aligned if $0° \leqslant \langle \alpha_{\text{fiber}} \rangle \leqslant 15°$. Data were calculated for 5 independent experiments.

B.11 FOCAL ADHESION ANALYSIS

B.11.1 hUVECs FA-lifetime analysis

The analysis of paxillin-transfected hUVECs was processed using a custom Matlab script. For each TIRF time series, image-intensity histograms were created. These histograms usually displayed 2 peaks, corresponding to the background pixels and the pixels of the transfected cells, respectively. The second signal peak was used for thresholding, eliminating all background values. For every pixel above threshold the standard deviation (SD) was calculated and converted to 16 bit. Furthermore, appearance time (AT) over threshold and lifetime (LT) was recorded. Normalized SD and LT were converted into a scatter plot, and analyzed.

B.11.2 PC12 cell manual FA analysis

For PC12 cells, TIRF images (see APPENDIX B.9.2) of FAs were loaded into ImageJ and inverted. FAs were manually drawn using the free-hand selection tool. Then measurements of FA area (in μm^2) and alignment angle versus NG direction were then obtained using the measurement and angle tools of ImageJ, respectively. The angle was measured with respect to the NG direction choosing the cell center as origin; a random reference direction was chosen for the FLAT surfaces. FAs were considered aligned if the angle was between 0 and 15 ° and misaligned if it was between 15 and 90 °. The number of FAs per cell was also registered.

B.11.3 WJ-hMSCs semi-automated analysis

For WJ-hMSC, FAs were modeled as elliptic objects and were semi-automatically processed by image correlation methods[206]. Adhesions were manually divided into groups according to their shape, size and orientation. Each group was manually selected using a free-hand selection tool, and a background threshold was set. These selections were spatially auto-correlated and the resulting correlation function was fitted using a 2D-Gaussian function, characterized by 3 parameters: two perpendicular standard deviations (d_{min} and d_{MAX}) and the angle between the FA-major axis and the pattern direction (φ'_{FA}). FAs were defined as aligned when $0 \leqslant \varphi'_{FA} \leqslant 15\,^{\circ}$. A calibration curve was created to limit the artifacts due to non-punctual microscopy point spread function (PSF): a series of simulated images were produced and analyzed using the correlation method as described above. The calibration curve was validated using images of 1 µm and 4 µm fluorescent beads (Tetraspeck, Invitrogen, Italy). FA-shape was finally described by area (A_{FA}) and elongation (p_{FA}). p_{FA} was calculated as the ratio between the FA long (d_{MAX}) and short (d_{min}) axis. This parameter spans from 0 (fully stretched, or linear, adhesions) to 1 (round adhesions).

B.12 MIGRATION ANALYSIS

Four independent time-lapse experiments were performed in epifluorescence using a 20× air objective (see APPENDIX B.9). Time-series were analyzed with the ImageJ manual tracking plugin to extract the coordinates of single cells as a time function. Data were then analyzed by a custom-made application written in Matlab. The following parameters were measured: *cell displacement* (R) (distance from the origin at the end of the time-lapse), *total path covered during the time-lapse* (S), *migration step* ($\boldsymbol{dS}$) and *average speed* (V) (calculated for intervals of 15 min). Directionality and the speed of each step was measured and classified in the two populations: *parallel* (dS_{par}) and *perpendicular* (dS_{per}) steps. $\boldsymbol{dS}$ was considered parallel if the angle between the step and the pattern was less than 15 °, while it is considered perpendicular if this angle was between 75 and 90 °.

LIST OF PUBLICATIONS

- S. Antonini, M. A. Cappelluti, **S. Meucci**, E. Jacchetti, O. Vittorio, P. Parchi, M. Lisanti, S. Pacini, M. Pietrini, F. Beltram & M. Cecchini · *Current Nanoscience* · Human mesenchymal stem cell enhanced morphological polarization by contact interaction with polyethylene terephthalate (PET) nanogratings (2014) 10:773–778

- V. Clericò, L. Masini, A. Boni, **S. Meucci**, M. Cecchini, F. Recchia, A. Bifone & A. Tredicucci · *PLOS ONE* · Water-dispersible three-dimensional LC-nanoresonators (2014) 9:e105474

- **S. Meucci**, M. Travagliati, O. Vittorio, G. Cirillo, L. Masini, V. Voliani, N. Picci, F. Beltram, A. Tredicucci & M. Cecchini · *RSC Advances* · Tubeless biochip for chemical stimulation of cells in closed-bioreactors: anti-cancer activity of the catechin–dextran conjugate (2014) 4:35017–35026

- L. Masini, **S. Meucci**, J. Xu, R. Degl'Innocenti, F. Castellano, H. E. Beere, D. Ritchie, D. Balduzzi, R. Pugliesi, A. Galli, F. Beltram, M. S. Vitiello, M. Cecchini & A. Tredicucci · *Laser & Photonics Reviews* · Terahertz probe of individual subwavelength objects in a water environment (2014) 1–9

- E. Jacchetti, I. Tonazzini, **S. Meucci**, F. Beltram & M. Cecchini · *Microelectronic Engineering* · Microstructured polydimethylsiloxane membranes for peripheral nerve regeneration (2014) 124:26-29

- **S. Meucci**, O. Vittorio, F. Beltram & M. Cecchini · *Microelectronic Engineering* · Tubeless biochip for tailoring cell co-cultures in closed microchambers (2014) 124:8–12

- E. Jacchetti, C. Di Rienzo, **S. Meucci**, F. Nocchi, F. Beltram & M. Cecchini · *Scientific reports* · Wharton's Jelly human Mesenchymal Stem Cell contact guidance by noisy nanotopographies (2014) 4:3830

- I. Tonazzini, **S. Meucci**, P. Faraci, F. Beltram & M. Cecchini · *Biomaterials* · Neuronal differentiation on anisotropic substrates and the influence of nanotopographical noise on neurite contact guidance (2013) 34:6027–6036

- **S. Meucci**, I. Tonazzini, F. Beltram & M. Cecchini · *Soft Matter* · Biocompatible noisy nanotopographies with specific directionality for controlled anisotropic cell cultures (2012) 8:1109–1119

SUBMITTED

- S. Antonini, **S. Meucci**, E. Jacchetti, M. Klingauf, F. Beltram, D. Poulikakos, M. Cecchini & A. Ferrari · The effect of lateral topographic feature size on endothelial function
- C. Avigo, N. Di Lascio, P. Armanetti, C. Kumsic, L. Cavigli, F. Ratto, **S. Meucci**, M. Cecchini, R. Pini, F. Faita & L. Menichetti · Organosilicon phantom for photoacoustic contrast agent characterization

ACKNOWLEDGEMENTS

During the years spent at NEST laboratory in Pisa I met many important people who behaved as teachers, colleges and friends, and I want to thank them all. Unfortunately, it is not possible to detail a complete list here, but I want you to know that if we spent some time together in clean room, at a microscope, in front of a Petri dish or drinking a coffee, then you *are* in that list—and I thank you.

I also want to write a few personal acknowledgments for the people that helped me most. First of all, I want to thank the director of Scuola Normale Superiore, Prof. Fabio Beltram, for granting me the opportunity to attend this educational path, and my supervisor, Dr. Marco Cecchini, for the examples he gave me during these years. Special and kind thanks are for Gimmi, the person that introduced me to the world of research, teaching me many important lessons about the scientific sphere—and beyond it—always with a personal and deep footprint. I also want to express my gratitude for the members of my research group, in particular Trava, Richie, Ela and Giorgio, as well as for Seba, Brondi and Riki, priceless colleges that supported me during the work (almost on a daily basis) and tremendous friends during the time away from the laboratory.

Kind thanks are also for the colleges and collaborators that helped me during my research activity, in particular the members of the THz group of Prof. Tredicucci at NEST laboratory (especially Luca and Vito), the group of Dr. Ferrari from the Laboratory of thermodynamics in emerging technologies of ETH Zurich, the group of Dr. Menichetti from the Istituto di fisiologia clinica of Pisa, the Gynaecology unit of the Azienda ospedaliera universitaria of Pisa, the 1st orthopaedic department and the Department of clinical and experimental medicine from the Università di Pisa, the group of Prof. Genua from the Università di Torino, and the group of Prof. Terenghi from the School of medicine of the University of Manchester .

Finally, I want to thank my family, especially Elena, for their constant and warm presence, and for their help in overcoming the fatigue that several times pulled me down.

BIBLIOGRAPHY

[1] L. A. Lowery and D. V. Vactor, "The trip of the tip : understanding the growth cone machinery," *Nature Reviews Molecular Cell Biology*, vol. 10, no. 5, pp. 332–343, 2009. (Cited on pages 1, 11, and 74.)

[2] T. M. Keenan and A. Folch, "Biomolecular gradients in cell culture systems.," *Lab on a chip*, vol. 8, pp. 34–57, Jan. 2008. (Cited on pages 2 and 16.)

[3] G. M. Whitesides, "The origins and the future of microfluidics.," *Nature*, vol. 442, pp. 368–73, July 2006. (Cited on pages 2 and 51.)

[4] D. C. Duffy, J. C. McDonald, O. J. Schueller, and G. M. Whitesides, "Rapid Prototyping of Microfluidic Systems in Poly(dimethylsiloxane).," *Analytical chemistry*, vol. 70, pp. 4974–84, Dec. 1998. (Cited on page 2.)

[5] M. A. Unger, H. P. Chou, T. Thorsen, A. Scherer, and S. R. Quake, "Monolithic microfabricated valves and pumps by multilayer soft lithography.," *Science (New York, N.Y.)*, vol. 288, pp. 113–6, Apr. 2000. (Cited on pages 2 and 18.)

[6] W. Liu, L. Li, X. Wang, L. Ren, X. Wang, J. Wang, Q. Tu, X. Huang, and J. Wang, "An integrated microfluidic system for studying cell-microenvironmental interactions versatilely and dynamically.," *Lab on a chip*, pp. 1717–1724, Apr. 2010. (Cited on pages 2 and 38.)

[7] V. Lecault, M. Vaninsberghe, S. Sekulovic, D. J. H. F. Knapp, S. Wohrer, W. Bowden, F. Viel, T. McLaughlin, A. Jarandehei, M. M. Miller, D. Falconnet, A. K. White, D. G. Kent, M. R. Copley, F. Taghipour, C. J. Eaves, R. K. Humphries, J. M. Piret, and C. L. Hansen, "High-throughput analysis of single hematopoietic stem cell proliferation in microfluidic cell culture arrays.," *Nature methods*, vol. 8, pp. 581–586, May 2011. (Cited on page 2.)

[8] J. Wang, H. C. Fan, B. Behr, and S. R. Quake, "Genome-wide single-cell analysis of recombination activity and de novo mutation rates in human sperm.," *Cell*, vol. 150, pp. 402–12, July 2012. (Cited on pages 2 and 14.)

[9] E. K. Sackmann, A. L. Fulton, and D. J. Beebe, "The present and future role of microfluidics in biomedical research," *Nature*, vol. 507, pp. 181–189, Mar. 2014. (Cited on pages 2, 13, and 16.)

[10] H. Bruus, *Theoretical Microfluidics*. Oxford University Press, 2008. (Cited on pages 2, 7, 10, and 11.)

[11] A. J. Muinonen-Martin, D. M. Veltman, G. Kalna, and R. H. Insall, "An improved chamber for direct visualisation of chemotaxis.," *PloS one*, vol. 5, p. e15309, Jan. 2010. (Cited on page 3.)

[12] B. Geiger, J. P. Spatz, and A. D. Bershadsky, "Environmental sensing through focal adhesions.," *Nature reviews. Molecular cell biology*, vol. 10, pp. 21–33, Jan. 2009. (Cited on pages 3, 45, 46, 47, 48, 50, and 88.)

[13] C. C. DuFort, M. J. Paszek, and V. M. Weaver, "Balancing forces: architectural control of mechanotransduction," *Nature Reviews Molecular Cell Biology*, vol. 12, pp. 308–319, May 2011. (Cited on page 3.)

[14] D. Ingber, "Tensegrity I. Cell structure and hierarchical systems biology," *Journal of Cell Science*, vol. 116, pp. 1157–1173, 2003. (Cited on page 3.)

[15] D. Ingber, "Tensegrity II. How structural networks influence cellular information processing networks," *Journal of Cell Science*, vol. 116, pp. 1397–1408, 2003. (Cited on page 3.)

[16] H. Herrmann, H. Bär, L. Kreplak, S. V. Strelkov, and U. Aebi, "Intermediate filaments: from cell architecture to nanomechanics.," *Nature reviews. Molecular cell biology*, vol. 8, pp. 562–73, July 2007. (Cited on page 3.)

[17] M. J. Dalby, "Nanostructured surfaces: cell engineering and cell biology," *Nanomedicine*, vol. 4, no. 3, pp. 247–248, 2009. (Cited on page 4.)

[18] J. Isaacs and T. Browne, "Overcoming short gaps in peripheral nerve repair: conduits and human acellular nerve allograft.," *Hand (New York, N.Y.)*, vol. 9, pp. 131–7, June 2014. (Cited on page 4.)

[19] K. Avila, D. Moxey, A. de Lozar, M. Avila, D. Barkley, and B. Hof, "The onset of turbulence in pipe flow.," *Science (New York, N.Y.)*, vol. 333, pp. 192–6, July 2011. (Cited on page 8.)

[20] H.-D. Kim and S. R. Peyton, "Bio-inspired materials for parsing matrix physicochemical control of cell migration: a review.," *Integrative biology : quantitative biosciences from nano to macro*, vol. 4, pp. 37–52, Jan. 2012. (Cited on page 11.)

[21] G. T. Vladisavljević, N. Khalid, M. a. Neves, T. Kuroiwa, M. Nakajima, K. Uemura, S. Ichikawa, and I. Kobayashi, "Industrial lab-on-a-chip: design, applications and scale-up for drug discovery and delivery.," *Advanced drug delivery reviews*, vol. 65, pp. 1626–63, Nov. 2013. (Cited on page 13.)

[22] Y. Song, Y.-Y. Huang, X. Liu, X. Zhang, M. Ferrari, and L. Qin, "Point-of-care technologies for molecular diagnostics using a drop of blood.," *Trends in biotechnology*, vol. 32, pp. 132–9, Mar. 2014. (Cited on page 13.)

[23] A. M. Streets and Y. Huang, "Chip in a lab: Microfluidics for next generation life science research.," *Biomicrofluidics*, vol. 7, p. 11302, Jan. 2013. (Cited on pages 13, 14, and 17.)

[24] I. A. Araci and S. R. Quake, "Microfluidic very large scale integration (mVLSI) with integrated micromechanical valves," *Lab on a Chip*, no. 12, pp. 2803–2806, 2012. (Cited on page 14.)

[25] R. H. Sedlak and K. R. Jerome, "Viral diagnostics in the era of digital polymerase chain reaction," *Diagnostic Microbiology and Infectious Disease*, vol. 75, no. 1, pp. 1 – 4, 2013. (Cited on page 14.)

[26] Y. Men, Y. Fu, Z. Chen, P. a. Sims, W. J. Greenleaf, and Y. Huang, "Digital polymerase chain reaction in an array of femtoliter polydimethylsiloxane microreactors.," *Analytical chemistry*, vol. 84, pp. 4262–6, May 2012. (Cited on page 14.)

[27] T. W. Phillips, I. G. Lignos, R. M. Maceiczyk, A. J. DeMello, and J. C. DeMello, "Nanocrystal synthesis in microfluidic reactors: where next?," *Lab on a chip*, vol. 14, pp. 3172–3180, June 2014. (Cited on page 14.)

[28] P. R. Makgwane and S. S. Ray, "Synthesis of nanomaterials by continuous-flow microfluidics: a review.," *Journal of nanoscience and nanotechnology*, vol. 14, pp. 1338–63, Feb. 2014. (Cited on page 14.)

[29] A. Kang, J. Park, J. Ju, G. S. Jeong, and S.-H. Lee, "Cell encapsulation via microtechnologies.," *Biomaterials*, vol. 35, pp. 2651–63, Mar. 2014. (Cited on page 14.)

[30] Y. Jun, E. Kang, S. Chae, and S.-H. Lee, "Microfluidic spinning of micro- and nano-scale fibers for tissue engineering.," *Lab on a chip*, vol. 14, Mar. 2014. (Cited on page 14.)

[31] A. L. Butcher, G. S. Offeddu, and M. L. Oyen, "Nanofibrous hydrogel composites as mechanically robust tissue engineering scaffolds," *Trends in Biotechnology*, vol. 32, no. 11, pp. 564 – 570, 2014. (Cited on page 14.)

[32] T. J. Sill and H. A. von Recum, "Electrospinning: Applications in drug delivery and tissue engineering," *Biomaterials*, vol. 29, no. 13, pp. 1989 – 2006, 2008. (Cited on pages 14, 15, and 48.)

[33] E. Carbone, T. Jiang, C. Nelson, N. Henry, and K.-H. Lo, "Small molecule delivery through nanofibrous scaffolds for musculoskeletal regenerative engineering," *Nanomedicine: Nanotechnology, Biology, and Medicine*, vol. 10, no. 8, pp. 1691–1699, 2014. (Cited on page 14.)

[34] L. Liu, M. Yoshioka, M. Nakajima, A. Ogasawara, J. Liu, K. Hasegawa, S. Li, J. Zou, N. Nakatsuji, K.-i. Kamei, and Y. Chen, "Biomaterials Nano fi brous gelatin substrates for long-term expansion of human pluripotent stem cells," *Biomaterials*, vol. 35, pp. 6259–6267, 2014. (Cited on pages 14 and 48.)

[35] K. H. Lee, S. J. Shin, Y. Park, and S.-H. Lee, "Synthesis of cell-laden alginate hollow fibers using microfluidic chips and microvascularized tissue-engineering applications.," *Small*, vol. 5, pp. 1264–8, June 2009. (Cited on page 15.)

[36] B. G. Chung, K.-H. Lee, A. Khademhosseini, and S.-H. Lee, "Microfluidic fabrication of microengineered hydrogels and their application in tissue engineering.," *Lab on a chip*, vol. 12, pp. 45–59, Jan. 2012. (Cited on page 15.)

[37] Y. Jun, A. R. Kang, J. S. Lee, S.-J. Park, D. Y. Lee, S.-H. Moon, and S.-H. Lee, "Microchip-based engineering of super-pancreatic islets supported by adipose-derived stem cells.," *Biomaterials*, vol. 35, pp. 4815–26, June 2014. (Cited on page 15.)

[38] K. B. Neeves, A. A. Onasoga, and A. R. Wufsus, "The use of microfluidics in hemostasis: clinical diagnostics and biomimetic models of vascular injury.," *Current opinion in hematology*, vol. 20, pp. 417–23, Sept. 2013. (Cited on page 15.)

[39] G. Bardan, F. Plouraboué, M. Zagzoule, and O. Balédent, "Simple patient-based transmantle pressure and shear estimate from cine phase-contrast MRI in cerebral aqueduct.," *IEEE transactions on bio-medical engineering*, vol. 59, pp. 2874–83, Oct. 2012. (Cited on page 15.)

[40] D. Franco, F. Milde, M. Klingauf, F. Orsenigo, E. Dejana, D. Poulikakos, M. Cecchini, P. Koumoutsakos, A. Ferrari, and V. Kurtcuoglu, "Accelerated endothelial wound healing on microstructured substrates under flow.," *Biomaterials*, vol. 34, pp. 1488–97, Feb. 2013. (Cited on pages 15, 31, 50, 61, and 62.)

[41] L. Wang, Z.-L. Zhang, J. Wdzieczak-Bakala, D.-W. Pang, J. Liu, and Y. Chen, "Patterning cells and shear flow conditions: convenient observation of endothelial cell remoulding, enhanced production of angiogenesis factors and drug response.," *Lab on a chip*, vol. 11, pp. 4235–40, Dec. 2011. (Cited on page 15.)

[42] Y. Tang, J. Shi, S. Li, L. Wang, Y. E. Cayre, and Y. Chen, "Microfluidic device with integrated microfilter of conical-shaped holes for high efficiency and high purity capture of circulating tumor cells.," *Scientific reports*, vol. 4, p. 6052, Jan. 2014. (Cited on page 15.)

[43] A. Singh, S. Suri, T. Lee, J. M. Chilton, M. T. Cooke, W. Chen, J. Fu, S. L. Stice, H. Lu, T. C. McDevitt, and A. J. García, "Adhesion strength–based, label-free isolation of human pluripotent stem cells," *Nature Methods*, vol. 10, pp. 438–444, Apr. 2013. (Cited on page 15.)

[44] P. Roca-Cusachs, R. Sunyer, and X. Trepat, "Mechanical guidance of cell migration: lessons from chemotaxis.," *Current opinion in cell biology*, vol. 25, pp. 543–9, Oct. 2013. (Cited on page 16.)

[45] L. Lara Rodriguez and I. C. Schneider, "Directed cell migration in multi-cue environments.," *Integrative biology : quantitative biosciences from nano to macro*, vol. 5, pp. 1306–23, Nov. 2013. (Cited on page 16.)

[46] S. Kim, H. J. Kim, and N. L. Jeon, "Biological applications of microfluidic gradient devices.," *Integrative biology : quantitative biosciences from nano to macro*, vol. 2, pp. 584–603, Nov. 2010. (Cited on pages 16 and 31.)

[47] N. Li Jeon, H. Baskaran, S. K. W. Dertinger, G. M. Whitesides, L. Van de Water, and M. Toner, "Neutrophil chemotaxis in linear and complex gradients of interleukin-8 formed in a microfabricated device.," *Nature biotechnology*, vol. 20, pp. 826–30, Aug. 2002. (Cited on page 16.)

[48] D. Irimia, D. a. Geba, and M. Toner, "Universal Microfluidic Gradient Generator," *Analytical chemistry*, vol. 78, no. 10, pp. 3472–3477, 2006. (Cited on page 16.)

[49] T. M. Keenan, C.-H. Hsu, and A. Folch, "Microfluidic "jets" for generating steady-state gradients of soluble molecules on open surfaces," *Applied Physics Letters*, vol. 89, no. 11, p. 114103, 2006. (Cited on pages 16 and 42.)

[50] N. Bhattacharjee, N. Li, T. M. Keenan, and A. Folch, "A neuron-benign microfluidic gradient generator for studying the response of mammalian neurons towards axon guidance factors.," *Integrative biology : quantitative biosciences from nano to macro*, vol. 2, pp. 669–79, Nov. 2010. (Cited on page 16.)

[51] R.-r. Xiao, W.-j. Zeng, Y.-t. Li, W. Zou, L. Wang, X.-f. Pei, M. Xie, and W.-h. Huang, "Simultaneous Generation of Gradients with Gradually Changed Slope in a Micro fl uidic Device for Quantifying Axon Response," *Analytical Chemistry*, vol. 85, pp. 7842–7850, 2013. (Cited on page 16.)

[52] P. Siegel, "Terahertz Technology in Biology and Medicine," *IEEE Transactions on Microwave Theory and Techniques*, vol. 52, pp. 2438–2447, Oct. 2004. (Cited on page 17.)

[53] R. Köhler, A. Tredicucci, F. Beltram, H. E. Beere, E. H. Linfield, A. G. Davies, D. A. Ritchie, R. C. Iotti, and F. Rossi, "Terahertz semiconductor-heterostructure laser.," *Nature*, vol. 417, pp. 156–9, May 2002. (Cited on page 18.)

[54] N. Yu, L. Diehl, E. Cubukcu, C. Pflügl, D. Bour, S. Corzine, J. Zhu, G. Höfler, K. B. Crozier, and F. Capasso, "Near-field imaging of quantum cascade laser transverse modes," *Opt. Express*, vol. 15, pp. 13227–13235, Oct 2007. (Cited on page 18.)

[55] N. Yu, J. Fan, Q. J. Wang, C. Pflügl, L. Diehl, T. Edamura, M. Yamanishi, H. Kan, and F. Capasso, "Small-divergence semiconductor lasers by plasmonic collimation," *Nature Photonics*, vol. 2, pp. 564–570, July 2008. (Cited on page 18.)

[56] D. Austin, N. Mullin, I. Luxmoore, I. C. Sandall, A. G. Cullis, A. Bismuto, J. Faist, J. K. Hobbs, and L. R. Wilson, "X-shaped plasmonic antenna on a quantum cascade laser," *Applied Physics Letters*, vol. 96, no. 15, pp. –, 2010. (Cited on page 18.)

[57] L. Masini, S. Meucci, J. Xu, R. Degl'Innocenti, F. Castellano, H. E. Beere, D. Ritchie, D. Balduzzi, R. Puglisi, A. Galli, F. Beltram, M. S. Vitiello, M. Cecchini, and A. Tredicucci, "Terahertz probe of individual subwavelength objects in a water environment," *Laser & Photonics Reviews*, pp. n/a–n/a, 2014. (Cited on pages 18, 19, and 113.)

[58] P. D. Cunningham, N. N. Valdes, F. A. Vallejo, L. M. Hayden, B. Polishak, X.-H. Zhou, J. Luo, A. K.-Y. Jen, J. C. Williams, and R. J. Twieg, "Broadband terahertz characterization of the refractive index and absorption of some important polymeric and organic electro-optic materials," *Journal of Applied Physics*, vol. 109, no. 4, 2011. (Cited on page 19.)

[59] R. Miles, X. C. Zhang, H. Eisele, and A. Krotkus, *Terahertz Frequency Detection and Identification of Materials and Objects*. Springer, 2007. (Cited on page 19.)

[60] S. Kim, H. Lee, M. Chung, and N. L. Jeon, "Engineering of functional, perfusable 3D microvascular networks on a chip.," *Lab on a chip*, pp. 1489–1500, Feb. 2013. (Cited on pages 19 and 36.)

[61] M. Heyden, E. Bründermann, U. Heugen, G. Niehues, D. M. Leitner, and M. Havenith, "Long-range influence of carbohydrates on the solvation dynamics of water–answers from terahertz absorption measurements and molecular modeling simulations.," *Journal of the American Chemical Society*, vol. 130, pp. 5773–9, Apr. 2008. (Cited on page 23.)

[62] L. C. Glangchai, M. Caldorera-Moore, L. Shi, and K. Roy, "Nanoimprint lithography based fabrication of shape-specific, enzymatically-triggered smart nanoparticles," *Journal of Controlled Release*, vol. 125, no. 3, pp. 263 – 272, 2008. (Cited on page 24.)

[63] J. Lee, W. Hasan, C. L. Stender, and T. W. Odom, "Pyramids: A platform for designing multifunctional plasmonic particles," *Accounts of Chemical Research*, vol. 41, no. 12, pp. 1762–1771, 2008. (Cited on page 24.)

[64] W. Hasan, C. Stender, M. Lee, C. Nehl, J. Lee, and T. Odom, "Tailoring the structure of nanopyramids for optimal heat generation," *Nano Letters*, vol. 9, no. 4, pp. 1555–1558, 2009. (Cited on page 24.)

[65] A. Mark, J. Gibbs, T.-C. Lee, and P. Fischer, "Hybrid nanocolloids with programmed three-dimensional shape and material composition," *Nature Materials*, vol. 12, no. 9, pp. 802–807, 2013. (Cited on page 24.)

[66] J. Pendry, "Metamaterials in the sunshine," *Nature Materials*, vol. 5, no. 8, pp. 599–600, 2006. (Cited on page 24.)

[67] V. Clericò, L. Masini, A. Boni, S. Meucci, M. Cecchini, F. a. Recchia, A. Tredicucci, and A. Bifone, "Water-Dispersible Three-Dimensional LC-Nanoresonators.," *PloS one*, vol. 9, p. e105474, Jan. 2014. (Cited on pages 24 and 27.)

[68] S. Linden, C. Enkrich, M. Wegener, J. Zhou, T. Koschny, and C. Soukoulis, "Magnetic response of metamaterials at 100 terahertz," *Science*, vol. 306, no. 5700, pp. 1351–1353, 2004. (Cited on page 26.)

[69] W. Padilla, M. Aronsson, C. Highstrete, M. Lee, A. Taylor, and R. Averitt, "Electrically resonant terahertz metamaterials: Theoretical and experimental investigations," *Physical Review B - Condensed Matter and Materials Physics*, vol. 75, no. 4, 2007.

[70] D. Güney, T. Koschny, and C. Soukoulis, "Reducing ohmic losses in metamaterials by geometric tailoring," *Physical Review B - Condensed Matter and Materials Physics*, vol. 80, no. 12, 2009. (Cited on page 26.)

[71] D. Chanda, K. Shigeta, S. Gupta, T. Cain, A. Carlson, A. Mihi, A. Baca, G. Bogart, P. Braun, and J. Rogers, "Large-area flexible 3d optical negative index metamaterial formed by nanotransfer printing," *Nature Nanotechnology*, vol. 6, no. 7, pp. 402–407, 2011. (Cited on page 27.)

[72] K. Svoboda and S. Block, "Biological applications of optical forces," *Annual Review of Biophysics and Biomolecular Structure*, vol. 23, pp. 247–285, 1994. (Cited on page 27.)

[73] M. Eghtedari, A. Oraevsky, J. a. Copland, N. a. Kotov, A. Conjusteau, and M. Motamedi, "High sensitivity of in vivo detection of gold nanorods using a laser optoacoustic imaging system.," *Nano letters*, vol. 7, pp. 1914–8, July 2007. (Cited on pages 28 and 29.)

[74] B. Kang, D. Yu, Y. Dai, S. Chang, D. Chen, and Y. Ding, "Cancer-cell targeting and photoacoustic therapy using carbon nanotubes as "bomb" agents," *Small*, vol. 5, no. 11, pp. 1292–1301, 2009. (Cited on page 28.)

[75] P. Beard, "Biomedical photoacoustic imaging.," *Interface focus*, vol. 1, pp. 602–31, Aug. 2011. (Cited on page 28.)

[76] M. a. Hahn, A. K. Singh, P. Sharma, S. C. Brown, and B. M. Moudgil, "Nanoparticles as contrast agents for in-vivo bioimaging: current status and future perspectives.," *Analytical and bioanalytical chemistry*, vol. 399, pp. 3–27, Jan. 2011. (Cited on pages 28 and 29.)

[77] J. Perezjuste, I. Pastorizasantos, L. Lizmarzan, and P. Mulvaney, "Gold nanorods: Synthesis, characterization and applications," *Coordination Chemistry Reviews*, vol. 249, pp. 1870–1901, Sept. 2005. (Cited on page 29.)

[78] L. V. Wang and H.-I. Wu, *Biomedical Optics*. Wiley, 2007. (Cited on page 29.)

[79] F. Ratto, P. Matteini, F. Rossi, and R. Pini, "Size and shape control in the overgrowth of gold nanorods," *Journal of Nanoparticle Research*, vol. 12, no. 6, pp. 2029–2036, 2010. (Cited on pages 29 and 109.)

[80] F. Ayers, A. Grant, D. Kuo, D. J. Cuccia, and A. J. Durkin, "Fabrication and characterization of silicone-based tissue phantoms with tunable optical properties in the visible and near infrared domain," *Proceedings of SPIE*, vol. 6870, pp. 687007–9, 2008. (Cited on page 29.)

[81] J. Park and R. S. Lakes, *Biomaterials: an introduction*. Springer, 2007. (Cited on page 29.)

[82] T. Yamauchi, M. Yanai, S. Takahashi, and N. K. Man, "Blood density monitoring during dialysis.," *Artificial organs*, vol. 20, pp. 981–5, Sept. 1996. (Cited on page 29.)

[83] H. Irving P., *Physics of the Human Body*. Springer, 2008. (Cited on page 29.)

[84] I. J. Oppenheim, A. Jain, and D. W. Greve, "MEMS ultrasonic transducers for the testing of solids.," *IEEE transactions on ultrasonics, ferroelectrics, and frequency control*, vol. 50, pp. 305–11, Mar. 2003. (Cited on page 29.)

[85] F. Sabri, M. E. Sebelik, R. Meacham, J. D. Boughter, M. J. Challis, and N. Leventis, "In vivo ultrasonic detection of polyurea crosslinked silica aerogel implants.," *PloS one*, vol. 8, p. e66348, Jan. 2013. (Cited on pages 29 and 30.)

[86] F. Conti, *Fisiologia Medica*. Mc-Graw Hill, 2010. (Cited on page 30.)

[87] L. Boneschansker, J. Yan, E. Wong, D. M. Briscoe, and D. Irimia, "Microfluidic platform for the quantitative analysis of leukocyte migration signatures.," *Nature communications*, vol. 5, p. 4787, Jan. 2014. (Cited on page 31.)

[88] H. Xu, M. M. Ferreira, and S. C. Heilshorn, "Small-molecule axon-polarization studies enabled by a shear-free microfluidic gradient generator.," *Lab on a chip*, vol. 14, pp. 2047–56, June 2014. (Cited on page 31.)

[89] R. Gómez-Sjöberg, A. a. Leyrat, D. M. Pirone, C. S. Chen, and S. R. Quake, "Versatile, fully automated, microfluidic cell culture system.," *Analytical chemistry*, vol. 79, pp. 8557–63, Nov. 2007. (Cited on pages 31 and 38.)

[90] J.-P. Frimat, M. Becker, Y.-Y. Chiang, U. Marggraf, D. Janasek, J. G. Hengstler, J. Franzke, and J. West, "A microfluidic array with cellular valving for single cell co-culture.," *Lab on a chip*, vol. 11, pp. 231–7, Jan. 2011. (Cited on pages 31 and 38.)

[91] M. Hamon, S. Jambovane, L. Bradley, A. Khademhosseini, and J. W. Hong, "Cell-Based Dose Responses from Open-Well Microchambers.," *Analytical chemistry*, vol. 85, pp. 5249–5254, May 2013. (Cited on page 31.)

[92] M. Travagliati, S. Girardo, D. Pisignano, F. Beltram, and M. Cecchini, "Easy monitoring of velocity fields in microfluidic devices using spatiotemporal image correlation spectroscopy," *Analytical Chemistry*, vol. 85, no. 17, pp. 8080–8084, 2013. (Cited on page 35.)

[93] A. M. Taylor, M. Blurton-jones, S. W. Rhee, D. H. Cribbs, and C. W. Cotman, "A microfluidic culture platform for CNS axonal injury , regeneration and transport," *Nature Met*, vol. 2, no. 8, pp. 599–605, 2005. (Cited on pages 36 and 42.)

[94] P. J. Hung, P. J. Lee, P. Sabounchi, R. Lin, and L. P. Lee, "Continuous perfusion microfluidic cell culture array for high-throughput cell-based assays.," *Biotechnology and bioengineering*, vol. 89, pp. 1–8, Jan. 2005. (Cited on pages 36 and 39.)

[95] A. Hibara, S. Iwayama, S. Matsuoka, M. Ueno, Y. Kikutani, M. Tokeshi, and T. Kitamori, "Surface modification method of microchannels for gas-liquid two-phase flow in microchips.," *Analytical chemistry*, vol. 77, pp. 943–7, Feb. 2005. (Cited on page 37.)

[96] W. Zheng, Z. Wang, W. Zhang, and X. Jiang, "A simple PDMS-based microfluidic channel design that removes bubbles for long-term on-chip culture of mammalian cells.," *Lab on a chip*, vol. 10, pp. 2906–10, Nov. 2010. (Cited on page 37.)

[97] A. M. Skelley and J. Voldman, "An active bubble trap and debubbler for microfluidic systems.," *Lab on a chip*, vol. 8, pp. 1733–7, Oct. 2008. (Cited on page 37.)

[98] C. Lochovsky, S. Yasotharan, and A. Günther, "Bubbles no more: in-plane trapping and removal of bubbles in microfluidic devices.," *Lab on a chip*, vol. 12, pp. 595–601, Feb. 2012. (Cited on page 37.)

[99] L. L. Bischel, E. W. K. Young, B. R. Mader, and D. J. Beebe, "Tubeless microfluidic angiogenesis assay with three-dimensional endothelial-lined microvessels.," *Biomaterials*, vol. 34, pp. 1471–7, Feb. 2013. (Cited on page 38.)

[100] N.-D. Dinh, Y.-Y. Chiang, H. Hardelauf, J. Baumann, E. Jackson, S. Waide, J. Sisnaiske, J.-P. Frimat, C. V. Thriel, D. Janasek, J.-M. Peyrin, and J. West, "Microfluidic construction of minimalistic neuronal co-cultures.," *Lab on a chip*, vol. 13, pp. 1402–12, Mar. 2013. (Cited on page 38.)

[101] A. Kunze, R. Meissner, S. Brando, and P. Renaud, "Co-pathological connected primary neurons in a microfluidic device for Alzheimer studies.," *Biotechnology and bioengineering*, vol. 108, pp. 2241–5, Sept. 2011. (Cited on pages 38 and 42.)

[102] X. Gao, Y. Tanaka, Y. Sugii, K. Mawatari, and T. Kitamori, "Basic Structure and Cell Culture Condition of a Bioartificial Renal Tubule on Chip towards a Cell-based Separation Microdevice.," *Analytical sciences : the international journal of the Japan Society for Analytical Chemistry*, vol. 27, p. 907, Jan. 2011. (Cited on page 38.)

[103] H.-Y. Wang, N. Bao, and C. Lu, "A microfluidic cell array with individually addressable culture chambers.," *Biosensors & bioelectronics*, vol. 24, pp. 613–7, Dec. 2008. (Cited on page 38.)

[104] S. Petronis, M. Stangegaard, C. Bovöge Christensen, and M. Dufva, "Transparent polymeric cell culture chip with integrated temperature control and uniform media perfusion," *BioTechniques*, vol. 40, pp. 368–376, Mar. 2006. (Cited on page 39.)

[105] N. Korin, A. Bransky, U. Dinnar, and S. Levenberg, "A parametric study of human fibroblasts culture in a microchannel bioreactor.," *Lab on a chip*, vol. 7, pp. 611–7, May 2007. (Cited on page 39.)

[106] A. B. Das, P. Loying, and B. Bose, "Human recombinant Cripto-1 increases doubling time and reduces proliferation of HeLa cells independent of pro-proliferation pathways.," *Cancer letters*, vol. 318, pp. 189–98, May 2012. (Cited on page 39.)

[107] R. Zhou, R. Mazurchuk, and R. M. Straubinger, "Antivasculature effects of doxorubicin-containing liposomes in an intracranial rat brain tumor model.," *Cancer research*, vol. 62, pp. 2561–6, May 2002. (Cited on page 41.)

[108] I. Bosma, J. C. Reijneveld, L. Douw, M. J. Vos, T. J. Postma, N. K. Aaronson, M. Muller, W. P. Vandertop, B. J. Slotman, M. J. B. Taphoorn, J. J. Heimans, and M. Klein, "Health-related quality of life of long-term high-grade glioma survivors.," *Neuro-oncology*, vol. 11, pp. 51–8, Feb. 2009. (Cited on page 41.)

[109] O. Vittorio, G. Cirillo, F. Iemma, G. Di Turi, E. Jacchetti, M. Curcio, S. Barbuti, N. Funel, O. I. Parisi, F. Puoci, and N. Picci, "Dextran-catechin conjugate: a potential treatment against the pancreatic ductal adenocarcinoma.," *Pharmaceutical research*, vol. 29, pp. 2601–14, Sept. 2012. (Cited on page 41.)

[110] J.-M. Peyrin, B. Deleglise, L. Saias, M. Vignes, P. Gougis, S. Magnifico, S. Betuing, M. Pietri, J. Caboche, P. Vanhoutte, J.-L. Viovy, and B. Brugg, "Axon diodes for the reconstruction of oriented neuronal networks in microfluidic chambers.," *Lab on a chip*, vol. 11, pp. 3663–3673, Sept. 2011. (Cited on page 42.)

[111] a. E. Kamholz, B. H. Weigl, B. a. Finlayson, and P. Yager, "Quantitative analysis of molecular interaction in a microfluidic channel: the T-sensor.," *Analytical chemistry*, vol. 71, pp. 5340–7, Dec. 1999. (Cited on page 42.)

[112] S. Sugiura, K. Hattori, and T. Kanamori, "Microfluidic serial dilution cell-based assay for analyzing drug dose response over a wide concentration range.," *Analytical chemistry*, vol. 82, pp. 8278–82, Oct. 2010. (Cited on page 44.)

[113] J.-T. Cao, Y.-D. Zhu, R. K. Rana, and J.-J. Zhu, "Microfluidic chip integrated with flexible PDMS-based electrochemical cytosensor for dynamic analysis of drug-induced apoptosis on HeLa cells.," *Biosensors & bioelectronics*, vol. 51, pp. 97–102, Jan. 2014.

[114] W. A. El-Said, C.-H. Yea, J.-W. Choi, and I.-K. Kwon, "Ultrathin polyaniline film coated on an indium–tin oxide cell-based chip for study of anticancer effect," *Thin Solid Films*, vol. 518, pp. 661–667, Nov. 2009.

[115] W. A. El-Said, C.-H. Yea, H. Kim, B.-K. Oh, and J.-W. Choi, "Cell-based chip for the detection of anticancer effect on HeLa cells using cyclic voltammetry.," *Biosensors & bioelectronics*, vol. 24, pp. 1259–65, Jan. 2009. (Cited on page 44.)

[116] M. Vicente-Manzanares, J. Zareno, L. Whitmore, C. Choi, and A. Horwitz, "Regulation of protrusion, adhesion dynamics, and polarity by myosins iia and iib in migrating cells," *Journal of Cell Biology*, vol. 176, no. 5, pp. 573–580, 2007. (Cited on page 47.)

[117] R. Zaidel-Bar, Z. Kam, and B. Geiger, "Polarized downregulation of the paxillin-p130cas-rac1 pathway induced by shear flow," *Journal of Cell Science*, vol. 118, no. 17, pp. 3997–4007, 2005. (Cited on page 47.)

[118] H. M. Moon and A. Wynshaw-Boris, "Cytoskeleton in action: lissencephaly, a neuronal migration disorder.," *Wiley interdisciplinary reviews. Developmental biology*, vol. 2, no. 2, pp. 229–45, 2013. (Cited on pages 47 and 74.)

[119] T. White and C. C. Hilgetag, "Gyrification and neural connectivity in schizophrenia.," *Development and psychopathology*, vol. 23, pp. 339–52, Feb. 2011. (Cited on pages 47 and 74.)

[120] D.-H. Kim, E. a. Lipke, P. Kim, R. Cheong, S. Thompson, M. Delannoy, K.-Y. Suh, L. Tung, and A. Levchenko, "Nanoscale cues regulate the structure and function of macroscopic cardiac tissue constructs.," *Proceedings of the National Academy of Sciences of the United States of America*, vol. 107, pp. 565–70, Jan. 2010. (Cited on pages 47 and 50.)

[121] A. Schriefl, G. Zeindlinger, D. Pierce, P. Regitnig, and G. Holzapfel, "Determination of the layer-specific distributed collagen fibre orientations in human thoracic and abdominal aortas and common iliac arteries," *Journal of the Royal Society Interface*, vol. 9, no. 71, pp. 1275–1286, 2012. (Cited on page 47.)

[122] D. Džaja, A. Hladnik, I. Bičanić, M. Baković, and Z. Petanjek, "Neocortical calretinin neurons in primates: Increase in proportion and microcircuitry structure," *Frontiers in Neuroanatomy*, vol. 8, no. SEP, 2014. (Cited on page 47.)

[123] D. Lewis, T. Hashimoto, and D. Volk, "Cortical inhibitory neurons and schizophrenia," *Nature Reviews Neuroscience*, vol. 6, no. 4, pp. 312–324, 2005. (Cited on page 47.)

[124] Y. Yokota, H. T. Ghashghaei, C. Han, H. Watson, K. J. Campbell, and E. S. Anton, "Radial Glial Dependent and Independent Dynamics of Interneuronal Migration in the Developing Cerebral Cortex," *PLoS ONE*, vol. 2, no. 8, p. e794, 2007. (Cited on page 48.)

[125] A. Hasan, A. Memic, N. Annabi, M. Hossain, A. Paul, M. R. Dokmeci, F. Dehghani, and A. Khademhosseini, "Electrospun scaffolds for tissue engineering of vascular grafts.," *Acta biomaterialia*, vol. 10, pp. 11–25, Jan. 2014. (Cited on page 48.)

[126] P. Wallin, C. Zandén, B. Carlberg, N. Hellström Erkenstam, J. Liu, and J. Gold, "A method to integrate patterned electrospun fibers with microfluidic systems to generate complex microenvironments for cell culture applications.," *Biomicrofluidics*, vol. 6, p. 24131, June 2012. (Cited on page 48.)

[127] J. H. Wendorff, S. Agarwal, and A. Greiner, *Electrospinning: materials, processing and applications*. 2012. (Cited on page 48.)

[128] J. Buber, L. Bergersen, J. Lock, K. Gauvreau, J. Esch, M. Landzberg, A. Valente, T. Sandora, and A. Marshall, "Bloodstream infections occurring in patients with percutaneously implanted bioprosthetic pulmonary valve: A single-center experience," *Circulation: Cardiovascular Interventions*, vol. 6, no. 3, pp. 301–310, 2013. (Cited on page 48.)

[129] D. Wirtz, K.-D. Heller, and F. Niethard, "Biomechanical aspects of the load-bearing capacity after total hip arthroplasty - an evaluation of the present knowledge in literature [biomechanische aspekte der belastungfahigkeit nach totalendoprothetischem ersatz des huftgelenkes]," *Zeitschrift fur Orthopadie und Ihre Grenzgebiete*, vol. 136, no. 4, pp. 310–316, 1998. (Cited on page 48.)

[130] J. Voskuhl, J. Brinkmann, and P. Jonkheijm, "Advances in contact printing technologies of carbohydrate, peptide and protein arrays," *Current Opinion in Chemical Biology*, vol. 18, no. 1, pp. 1–7, 2014. (Cited on page 48.)

[131] C. S. Chen, M. Mrksich, S. Huang, G. M. Whitesides, and D. E. Ingber, "Geometric control of cell life and death.," *Science (New York, N.Y.)*, vol. 276, pp. 1425–8, May 1997. (Cited on page 48.)

[132] M. Théry, A. Pépin, E. Dressaire, Y. Chen, and M. Bornens, "Cell distribution of stress fibres in response to the geometry of the adhesive environment.," *Cell motility and the cytoskeleton*, vol. 63, pp. 341–55, June 2006. (Cited on pages 48 and 56.)

[133] R. McBeath, D. M. Pirone, C. M. Nelson, K. Bhadriraju, and C. S. Chen, "Cell Shape, Cytoskeletal Tension, and RhoA Regulate Stem Cell Lineage Commitment," *Developmental Cell*, vol. 6, pp. 483–495, Apr. 2004. (Cited on pages 48 and 56.)

[134] A. Ferrari, M. Cecchini, A. Dhawan, S. Micera, I. Tonazzini, R. Stabile, D. Pisignano, and F. Beltram, "Nanotopographic control of neuronal polarity.," *Nano letters*, vol. 11, pp. 505–11, Mar. 2011. (Cited on pages 49, 50, 70, and 78.)

[135] F. Badique, D. R. Stamov, P. M. Davidson, M. Veuillet, G. Reiter, J.-N. Freund, C. M. Franz, and K. Anselme, "Directing nuclear deformation on micropillared surfaces by substrate geometry and cytoskeleton organization.," *Biomaterials*, Jan. 2013. (Cited on page 49.)

[136] F. Kantawong, M. Robertson, N. Gadegaard, R. Oreffo, R. Burchmore, and M. Dalby, "Protein expression of stro-1 cells in response to different topographic features," *Journal of Tissue Engineering*, vol. 2, no. 1, pp. 1–10, 2011. (Cited on page 49.)

[137] H. V. Unadkat, M. Hulsman, K. Cornelissen, B. J. Papenburg, R. K. Truckenmüller, G. F. Post, M. Uetz, M. J. T. Reinders, D. Stamatialis, C. a. van Blitterswijk, and J. de Boer, "An algorithm-based topographical biomaterials library to instruct cell fate.," *Proceedings of the National Academy of Sciences of the United States of America*, vol. 108, pp. 16565–16570, Sept. 2011. (Cited on pages 49, 56, and 60.)

[138] D. Franco, M. Klingauf, M. Bednarzik, M. Cecchini, V. Kurtcuoglu, J. Gobrecht, D. Poulikakos, and A. Ferrari, "Control of initial endothelial spreading by topographic activation of focal adhesion kinase," *Soft Matter*, vol. 7, no. 16, p. 7313, 2011. (Cited on pages 50, 61, 62, 70, and 72.)

[139] D. Ingber, "Cellular tensegrity : defining new rules of biological design that govern the cytoskeleton," *Journal of Cell Science*, vol. 627, pp. 613–627, 1993. (Cited on page 50.)

[140] A. Ferrari, M. Cecchini, M. Serresi, P. Faraci, D. Pisignano, and F. Beltram, "Neuronal polarity selection by topography-induced focal adhesion control.," *Biomaterials*, vol. 31, pp. 4682–94, June 2010. (Cited on pages 50, 63, 68, 75, 78, and 120.)

[141] K. Sheets, S. Wunsch, C. Ng, and A. S. Nain, "Shape-dependent cell migration and focal adhesion organization on suspended and aligned nanofiber scaffolds.," *Acta biomaterialia*, vol. 9, pp. 7169–77, July 2013. (Cited on page 50.)

[142] H. Jansen, H. Gardeniers, M. D. Boer, and J. Fluitman, "A survey on the reactive ion etching of silicon in microtechnology," *J. Micromech. Microeng.*, vol. 6, pp. 14–28, 1996. (Cited on page 52.)

[143] A. Grigorescu and C. Hagen, "Zresists for sub-20-nm electron beam lithography with a focus on hsq: State of the art," *Nanotechnology*, vol. 20, no. 29, 2009. (Cited on page 52.)

[144] M. Elsayed and O. M. Merkel, "Nanoimprinting of topographical and 3D cell culture scaffolds Review," *Future Medicine*, vol. 9, pp. 349–366, 2014. (Cited on page 52.)

[145] M. Cecchini, F. Signori, P. Pingue, S. Bronco, F. Ciardelli, and F. Beltram, "High-resolution poly(ethylene terephthalate) (PET) hot embossing at low temperature: thermal, mechanical, and optical analysis of nanopatterned films.," *Langmuir : the ACS journal of surfaces and colloids*, vol. 24, pp. 12581–6, Nov. 2008. (Cited on page 53.)

[146] V. Feron, J. Jetten, N. De Kruijf, and F. Van Den Berg, "Polyethylene terephthalate bottles (prbs): A health and safety assessment," *Food Additives and Contaminants*, vol. 11, no. 5, pp. 571–594, 1994. (Cited on page 53.)

[147] K. E. Herold and A. Rasooly, *Lab on a Chip Technology: Fabrication and microfluidics*. 2009. (Cited on page 53.)

[148] E. Kon, A. Muraglia, A. Corsi, P. Bianco, M. Marcacci, I. Martin, A. Boyde, I. Ruspantini, P. Chistolini, M. Rocca, R. Giardino, R. Cancedda, and R. Quarto, "Autologous bone marrow stromal cells loaded onto porous hydroxyapatite ceramic accelerate bone repair in critical-size defects of sheep long bones," *Journal of Biomedical Materials Research*, vol. 49, no. 3, pp. 328–337, 2000. (Cited on page 56.)

[149] R. LeGeros, "Calcium phosphate-based osteoinductive materials," *Chemical Reviews*, vol. 108, no. 11, pp. 4742–4753, 2008. (Cited on page 56.)

[150] N. Binulal, M. Deepthy, N. Selvamurugan, K. Shalumon, S. Suja, U. Mony, R. Jayakumar, and S. Nair, "Role of nanofibrous poly(caprolactone) scaffolds in human mesenchymal stem cell attachment and spreading for in vitro bone tissue engineering-response to osteogenic regulators," *Tissue Engineering - Part A*, vol. 16, no. 2, pp. 393–404, 2010. (Cited on page 56.)

[151] O. Zouani, C. Chollet, B. Guillotin, and M.-C. Durrieu, "Differentiation of pre-osteoblast cells on poly(ethylene terephthalate) grafted with rgd and/or bmps mimetic peptides," *Biomaterials*, vol. 31, no. 32, pp. 8245–8253, 2010. (Cited on page 56.)

[152] T. Saito, M. Takemoto, A. Fukuda, Y. Kuroda, S. Fujibayashi, M. Neo, D. Honjoh, T. Hiraide, T. Kizuki, T. Kokubo, and T. Nakamura, "Effect of titania-based surface modification of polyethylene terephthalate on bone-implant bonding and peri-implant tissue reaction," *Acta Biomaterialia*, vol. 7, no. 4, pp. 1558–1569, 2011. (Cited on page 56.)

[153] D. Zhang and K. Kilian, "The effect of mesenchymal stem cell shape on the maintenance of multipotency," *Biomaterials*, vol. 34, no. 16, pp. 3962–3969, 2013. (Cited on page 56.)

[154] M. Dalby, S. Childs, M. Riehle, H. Johnstone, S. Affrossman, and A. Curtis, "Fibroblast reaction to island topography: Changes in cytoskeleton and morphology with time," *Biomaterials*, vol. 24, no. 6, pp. 927–935, 2003. (Cited on page 56.)

[155] M. Théry, "Micropatterning as a tool to decipher cell morphogenesis and functions," *Journal of Cell Science*, vol. 123, no. 24, pp. 4201–4213, 2010. (Cited on page 56.)

[156] E. Yim, R. Reano, S. Pang, A. Yee, C. Chen, and K. Leong, "Nanopattern-induced changes in morphology and motility of smooth muscle cells," *Biomaterials*, vol. 26, no. 26, pp. 5405–5413, 2005. (Cited on pages 59 and 90.)

[157] M. Versaevel, T. Grevesse, and S. Gabriele, "Spatial coordination between cell and nuclear shape within micropatterned endothelial cells," *Nature Communications*, vol. 3, 2012.

[158] C. Natale, M. Ventre, and P. Netti, "Tuning the material-cytoskeleton crosstalk via nanoconfinement of focal adhesions," *Biomaterials*, vol. 35, no. 9, pp. 2743–2751, 2014. (Cited on page 59.)

[159] S. Watari, K. Hayashi, J. Wood, P. Russell, P. Nealey, C. Murphy, and D. Genetos, "Modulation of osteogenic differentiation in hmscs cells by submicron topographically-patterned ridges and grooves," *Biomaterials*, vol. 33, no. 1, pp. 128–136, 2012. (Cited on page 60.)

[160] P.-Y. Wang, W.-T. Li, J. Yu, and W.-B. Tsai, "Modulation of osteogenic, adipogenic and myogenic differentiation of mesenchymal stem cells by submicron grooved topography," *Journal of Materials Science: Materials in Medicine*, vol. 23, no. 12, pp. 3015–3028, 2012. (Cited on page 60.)

[161] K. Kilian, B. Bugarija, B. Lahn, and M. Mrksich, "Geometric cues for directing the differentiation of mesenchymal stem cells," *Proceedings of the National Academy of Sciences of the United States of America*, vol. 107, no. 11, pp. 4872–4877, 2010. (Cited on page 60.)

[162] J. Gasiorowski, S. Liliensiek, P. Russell, D. Stephan, P. Nealey, and C. Murphy, "Alterations in gene expression of human vascular endothelial cells associated with nanotopographic cues," *Biomaterials*, vol. 31, no. 34, pp. 8882–8888, 2010. (Cited on page 62.)

[163] S. Liliensiek, J. Wood, J. Yong, R. Auerbach, P. Nealey, and C. Murphy, "Modulation of human vascular endothelial cell behaviors by nanotopographic cues," *Biomaterials*, vol. 31, no. 20, pp. 5418–5426, 2010. (Cited on page 62.)

[164] A. Ferrari, P. Faraci, M. Cecchini, and F. Beltram, "The effect of alternative neuronal differentiation pathways on PC12 cell adhesion and neurite alignment to nanogratings.," *Biomaterials*, vol. 31, pp. 2565–73, Mar. 2010. (Cited on pages 63, 68, 75, and 78.)

[165] J. Kassis, E. Guancial, H. Doong, V. Virador, and E. Kohn, "Cair-1/bag-3 modulates cell adhesion and migration by downregulating activity of focal adhesion proteins," *Experimental Cell Research*, vol. 312, no. 15, pp. 2962–2971, 2006. (Cited on page 63.)

[166] N. Stevenson, C. McFarlane, S. Ong, K. Nahlik, A. Kelvin, M. Addley, A. Long, D. Greaves, C. O'Farrelly, and J. Johnston, "Suppressor of cytokine signalling (socs) 1 and 3 enhance cell adhesion and inhibit migration towards the chemokine eotaxin/ccl11," *FEBS Letters*, vol. 584, no. 21, pp. 4469–4474, 2010. (Cited on page 63.)

[167] G. Kadare, N. Gervasi, K. Brami-Cherrier, H. Blockus, S. El Messari, S. T. Arold, and J.-A. Girault, "Conformational Dynamics of the Focal Adhesion Targeting Domain Control specific functions of focal adhesion kinase in cells.," *The Journal of biological chemistry*, Nov. 2014. (Cited on page 63.)

[168] R. Varga, M. Eriksson, M. Erdos, M. Olive, I. Harten, F. Kolodgie, B. Capell, J. Cheng, D. Faddah, S. Perkins, H. Avallone, H. San, X. Qu, S. Ganesh, L. Gordon, R. Virmani, T. Wight, E. Nabel, and F. Collins, "Progressive vascular smooth muscle cell defects in a mouse model of hutchinson-gilford progeria syndrome," *Proceedings of the National Academy of Sciences of the United States of America*, vol. 103, no. 9, pp. 3250–3255, 2006. (Cited on page 67.)

[169] K. Kessenbrock, V. Plaks, and Z. Werb, "Matrix metalloproteinases: Regulators of the tumor microenvironment," *Cell*, vol. 141, no. 1, pp. 52–67, 2010. (Cited on page 67.)

[170] R. McMurray, N. Gadegaard, P. Tsimbouri, K. Burgess, L. McNamara, R. Tare, K. Murawski, E. Kingham, R. Oreffo, and M. Dalby, "Nanoscale surfaces for the long-term maintenance of mesenchymal stem cell phenotype and multipotency," *Nature Materials*, vol. 10, no. 8, pp. 637–644, 2011. (Cited on pages 67 and 82.)

[171] W. Huang, R. Begum, T. Barber, V. Ibba, N. Tee, M. Hussain, M. Arastoo, Q. Yang, L. Robson, S. Lesage, T. Gheysens, N. J. Skaer, D. Knight, and J. Priestley, "Regenerative potential of silk conduits in repair of peripheral nerve injury in adult rats," *Biomaterials*, vol. 33, no. 1, pp. 59 – 71, 2012. (Cited on page 67.)

[172] H. Tabesh, G. Amoabediny, N. Nik, M. Heydari, M. Yosefifard, S. Siadat, and K. Mottaghy, "The role of biodegradable engineered scaffolds seeded with schwann cells for spinal cord regeneration," *Neurochemistry International*, vol. 54, no. 2, pp. 73–83, 2009. (Cited on page 67.)

[173] J. Huang, S. V. Grater, F. Corbellini, S. Rinck, E. Bock, R. Kemkemer, H. Kessler, J. Ding, and J. P. Spatz, "Impact of order and disorder in RGD nanopatterns on cell adhesion.," *Nano letters*, vol. 9, pp. 1111–6, Mar. 2009. (Cited on page 68.)

[174] M. Dalby, D. McCloy, M. Robertson, H. Agheli, D. Sutherland, S. Affrossman, and R. Oreffo, "Osteoprogenitor response to semi-ordered and random nanotopographies," *Biomaterials*, vol. 27, no. 15, pp. 2980–2987, 2006. (Cited on page 68.)

[175] M. Dalby, N. Gadegaard, R. Tare, A. Andar, M. Riehle, P. Herzyk, C. Wilkinson, and R. Oreffo, "The control of human mesenchymal cell differentiation using nanoscale symmetry and disorder," *Nature Materials*, vol. 6, no. 12, pp. 997–1003, 2007. (Cited on pages 68 and 88.)

[176] A. Ferrari, M. Cecchini, R. Degl Innocenti, and F. Beltram, "Directional PC12 cell migration along plastic nanotracks.," *IEEE transactions on bio-medical engineering*, vol. 56, pp. 2692–6, Nov. 2009. (Cited on pages 68 and 72.)

[177] S. Antonini, M. A. Cappelluti, S. Meucci, E. Jacchetti, O. Vittorio, P. Parchi, M. Lisanti, S. Pacini, M. Petrini, F. Beltram, and M. Cecchini, "Human Mesenchymal Stromal Cell Enhanced Morphological Polarization by Contact Interaction with Polyethylene Terephthalate Nanogratings | BenthamScience," *Current Nanoscience*, vol. 10, no. 6, pp. 773–778, 2014. (Cited on page 72.)

[178] S. Meucci, I. Tonazzini, F. Beltram, and M. Cecchini, "Biocompatible noisy nanotopographies with specific directionality for controlled anisotropic cell cultures," *Soft Matter*, vol. 8, pp. 1109–1119, Nov. 2012. (Cited on pages 73, 75, and 78.)

[179] S. Kennedy, N. Washburn, C. Simon Jr., and E. Amis, "Combinatorial screen of the effect of surface energy on fibronectin-mediated osteoblast adhesion, spreading and proliferation," *Biomaterials*, vol. 27, no. 20, pp. 3817–3824, 2006. (Cited on page 73.)

[180] G. Zhao, A. Raines, M. Wieland, Z. Schwartz, and B. Boyan, "Requirement for both micron- and submicron scale structure for synergistic responses of osteoblasts to substrate surface energy and topography," *Biomaterials*, vol. 28, no. 18, pp. 2821–2829, 2007. (Cited on page 73.)

[181] N. Arimura and K. Kaibuchi, "Neuronal polarity: from extracellular signals to intracellular mechanisms.," *Nature reviews. Neuroscience*, vol. 8, pp. 194–205, Mar. 2007. (Cited on page 74.)

[182] L. Greene and A. Tischler, "Establishment of a noradrenergic clonal line of rat adrenal pheochromocytoma cells which respond to nerve growth factor," *Proceedings of the National Academy of Sciences of the United States of America*, vol. 73, no. 7, pp. 2424–2428, 1976. (Cited on page 74.)

[183] S. Santos, P. Verveer, and P. Bastiaens, "Growth factor-induced mapk network topology shapes erk response determining pc-12 cell fate," *Nature Cell Biology*, vol. 9, no. 3, pp. 324–330, 2007. (Cited on page 74.)

[184] D. Vaudry, P. Stork, P. Lazarovici, and L. Eiden, "Signaling pathways for pc12 cell differentiation: Making the right connections," *Science*, vol. 296, no. 5573, pp. 1648–1649, 2002. (Cited on page 74.)

[185] V. Brunetti, G. Maiorano, L. Rizzello, B. Sorce, S. Sabella, R. Cingolani, and P. P. Pompa, "Neurons sense nanoscale roughness with nanometer sensitivity.," *Proceedings of the National Academy of Sciences of the United States of America*, vol. 107, pp. 6264–9, Apr. 2010. (Cited on page 75.)

[186] F. Intranuovo, P. Favia, E. Sardella, C. Ingrosso, M. Nardulli, R. D'Agostino, and R. Gristina, "Osteoblast-like cell behavior on plasma deposited micro/nanopatterned coatings.," *Biomacromolecules*, vol. 12, pp. 380–7, Feb. 2011. (Cited on page 75.)

[187] M. D. Mark, Y. Liu, S. T. Wong, T. R. Hinds, and D. R. Storm, "Stimulation of neurite outgrowth in PC12 cells by EGF and KCl depolarization: a Ca(2+)-independent phenomenon.," *The Journal of cell biology*, vol. 130, pp. 701–10, Aug. 1995. (Cited on page 75.)

[188] I. Tonazzini, S. Meucci, P. Faraci, F. Beltram, and M. Cecchini, "Neuronal differentiation on anisotropic substrates and the influence of nanotopographical noise on neurite contact guidance," *Biomaterials*, vol. 34, pp. 6027–6036, May 2013. (Cited on page 77.)

[189] Y.-C. Chang, P. Nalbant, J. Birkenfeld, Z.-F. Chang, and G. Bokoch, "3gef-h1 couples nocodazole-induced microtubule disassembly to cell contractility via rhoa," *Molecular Biology of the Cell*, vol. 19, no. 5, pp. 2147–2153, 2008. (Cited on page 78.)

[190] E. Jacchetti, C. Di Rienzo, S. Meucci, F. Nocchi, F. Beltram, and M. Cecchini, "Wharton's Jelly human Mesenchymal Stem Cell contact guidance by noisy nanotopographies.," *Scientific reports*, vol. 4, p. 3830, Jan. 2014. (Cited on pages 82, 83, 86, and 87.)

[191] L. McNamara, R. McMurray, M. Biggs, F. Kantawong, R. Oreffo, and M. Dalby, "Nanotopographical control of stem cell differentiation," *Journal of Tissue Engineering*, vol. 1, no. 1, pp. 1–13, 2010. (Cited on page 82.)

[192] F. Guilak, D. Cohen, B. Estes, J. Gimble, W. Liedtke, and C. Chen, "Control of stem cell fate by physical interactions with the extracellular matrix," *Cell Stem Cell*, vol. 5, no. 1, pp. 17–26, 2009. (Cited on page 82.)

[193] Z. Bulj, S. Duchi, A. Bevilacqua, A. Gherardi, B. Dozza, F. Piccinini, G. Mariani, E. Lucarelli, S. Giannini, D. Donati, and S. Marmiroli, "Protein kinase b/akt isoform 2 drives migration of human mesenchymal stem cells," *International Journal of Oncology*, vol. 42, no. 1, pp. 118–126, 2013. (Cited on page 82.)

[194] A. Ponte, E. Marais, N. Gallay, A. Langonné, B. Delorme, O. Hérault, P. Charbord, and J. Domenech, "The in vitro migration capacity of human bone marrow mesenchymal stem cells: Comparison of chemokine and growth factor chemotactic activities," *Stem Cells*, vol. 25, no. 7, pp. 1737–1745, 2007. (Cited on page 82.)

[195] S. Martino, F. D'Angelo, I. Armentano, J. Kenny, and A. Orlacchio, "Stem cell-biomaterial interactions for regenerative medicine," *Biotechnology Advances*, vol. 30, no. 1, pp. 338–351, 2012. (Cited on page 82.)

[196] J. Buschmann, L. Härter, S. Gao, S. Hemmi, M. Welti, N. Hild, O. Schneider, W. Stark, N. Lindenblatt, C. Werner, G. Wanner, and M. Calcagni, "Tissue engineered bone grafts based on biomimetic nanocomposite plga/amorphous calcium phosphate scaffold and human adipose-derived stem cells," *Injury*, vol. 43, no. 10, pp. 1689–1697, 2012. (Cited on page 82.)

[197] O. Vittorio, E. Jacchetti, S. Pacini, and M. Cecchini, "Endothelial differentiation of mesenchymal stromal cells: When traditional biology meets mechanotransduction," *Integrative Biology (United Kingdom)*, vol. 5, no. 2, pp. 291–299, 2013. (Cited on page 82.)

[198] N. Tsagias, I. Koliakos, V. Karagiannis, M. Eleftheriadou, and G. Koliakos, "Isolation of mesenchymal stem cells using the total length of umbilical cord for transplantation purposes," *Transfusion Medicine*, vol. 21, no. 4, pp. 253–261, 2011. (Cited on page 82.)

[199] H.-S. Wang, S.-C. Hung, S.-T. Peng, C.-C. Huang, H.-M. Wei, Y.-J. Guo, Y.-S. Fu, M.-C. Lai, and C.-C. Chen, "Mesenchymal stem cells in the wharton's jelly of the human umbilical cord," *Stem Cells*, vol. 22, no. 7, pp. 1330–1337, 2004. (Cited on page 82.)

[200] C. Robertson and S. George, "Theory and practical recommendations for autocorrelation-based image correlation spectroscopy," *Journal of Biomedical Optics*, vol. 17, no. 8, 2012. (Cited on page 85.)

[201] V. Vogel and M. Sheetz, "Local force and geometry sensing regulate cell functions," *Nature Reviews Molecular Cell Biology*, vol. 7, no. 4, pp. 265–275, 2006. (Cited on page 88.)

[202] J. Parsons, A. Horwitz, and M. Schwartz, "Cell adhesion: Integrating cytoskeletal dynamics and cellular tension," *Nature Reviews Molecular Cell Biology*, vol. 11, no. 9, pp. 633–643, 2010. (Cited on page 88.)

[203] M. Dalby, S. Yarwood, M. Riehle, H. Johnstone, S. Affrossman, and A. Curtis, "Increasing fibroblast response to materials using nanotopography: Morphological and genetic measurements of cell response to 13-nm-high polymer demixed islands," *Experimental Cell Research*, vol. 276, no. 1, pp. 1–9, 2002. (Cited on page 88.)

[204] P. Rørth, "Whence directionality: Guidance mechanisms in solitary and collective cell migration," *Developmental Cell*, vol. 20, no. 1, pp. 9–18, 2011. (Cited on page 90.)

[205] A. Ridley, M. Schwartz, K. Burridge, R. Firtel, M. Ginsberg, G. Borisy, J. Parsons, and A. Horwitz, "Cell migration: Integrating signals from front to back," *Science*, vol. 302, no. 5651, pp. 1704–1709, 2003. (Cited on page 90.)

[206] J.-P. Kaiser, A. Reinmann, and A. Bruinink, "The effect of topographic characteristics on cell migration velocity," *Biomaterials*, vol. 27, no. 30, pp. 5230–5241, 2006. (Cited on pages 90 and 124.)

[207] D. Hamilton, C. Oates, A. Hasanzadeh, and S. Mittler, "Migration of periodontal ligament fibroblasts on nanometric topographical patterns: Influence of filopodia and focal adhesions on contact guidance," *PLoS ONE*, vol. 5, no. 12, 2010. (Cited on page 90.)

[208] M. Sun, M. McGowan, P. J. Kingham, G. Terenghi, and S. Downes, "Novel thin-walled nerve conduit with microgrooved surface patterns for enhanced peripheral nerve repair.," *Journal of materials science. Materials in medicine*, vol. 21, pp. 2765–74, Oct. 2010. (Cited on pages 93, 94, and 101.)

[209] M. Lietz and B. Schlosshauer, *Nerve Guides*, ch. 169, pp. 1043–1055. (Cited on page 93.)

[210] S. Sunderland, "A classification of peripheral nerve injuries producing loss of function," *Brain*, vol. 74, no. 4, pp. 491–516, 1951. (Cited on page 93.)

[211] B. Schlosshauer, L. Dreesmann, H.-E. Schaller, and N. Sinis, "Synthetic nerve guide implants in humans: A comprehensive survey," *Neurosurgery*, vol. 59, no. 4, pp. 740–747, 2006. (Cited on page 93.)

[212] P.-N. Mohanna, R. Young, M. Wiberg, and G. Terenghi, "A composite polhydroxybutyrate-glial growth factor conduit for long nerve gap repairs," *Journal of Anatomy*, vol. 203, no. 6, pp. 553–565, 2003. (Cited on page 94.)

[213] W. Daly, L. Yao, D. Zeugolis, A. Windebank, and A. Pandit, "A biomaterials approach to peripheral nerve regeneration: Bridging the peripheral nerve gap and enhancing functional recovery," *Journal of the Royal Society Interface*, vol. 9, no. 67, pp. 202–221, 2012. (Cited on page 94.)

[214] S. Mackinnon and A. Lee Dellon, "A study of nerve regeneration across synthetic (maxon) and biologic (collagen) nerve conduits for nerve gaps up to 5 cm in the primate," *Journal of Reconstructive Microsurgery*, vol. 6, no. 2, pp. 117–121, 1990. (Cited on page 94.)

[215] J. Cai, X. Peng, K. Nelson, R. Eberhart, and G. Smith, "Permeable guidance channels containing microfilament scaffolds enhance axon growth and maturation," *Journal of Biomedical Materials Research - Part A*, vol. 75, no. 2, pp. 374–386, 2005. (Cited on page 94.)

[216] F. Johansson, P. Carlberg, N. Danielsen, L. Montelius, and M. Kanje, "Axonal outgrowth on nano-imprinted patterns," *Biomaterials*, vol. 27, no. 8, pp. 1251–1258, 2006. (Cited on page 94.)

[217] E. Jacchetti, I. Tonazzini, S. Meucci, F. Beltram, and M. Cecchini, "Microstructured polydimethylsiloxane membranes for peripheral nerve regeneration," *Microelectronic Engineering*, vol. 124, pp. 26–29, July 2014. (Cited on pages 94 and 96.)

[218] B. RP., "The role of the Schwann cell in trophic support and regeneration.," *Journal of Neurology*, pp. 19–21, Dec. 1994. (Cited on page 94.)

[219] K. R. Jessen and R. Mirsky, "Schwann cells and their precursors emerge as major regulators of nerve development," *Trends in Neurosciences*, vol. 22, pp. 402–410, Sept. 1999. (Cited on page 94.)

[220] S. A. Mobasseri, G. Terenghi, and S. Downes, "Micro-structural geometry of thin films intended for the inner lumen of nerve conduits affects nerve repair.," *Journal of materials science. Materials in medicine*, vol. 24, pp. 1639–47, July 2013. (Cited on pages 94, 95, and 101.)

[221] S. Pinto, P. Alves, C. Matos, A. Santos, L. Rodrigues, J. Teixeira, and M. Gil, "Poly(dimethyl siloxane) surface modification by low pressure plasma to improve its characteristics towards biomedical applications," *Colloids and Surfaces B: Biointerfaces*, vol. 81, no. 1, pp. 20 – 26, 2010. (Cited on pages 95 and 101.)

[222] M. E. Moustafa, V. S. Gadepalli, A. a. Elmak, W. Lee, R. R. Rao, and V. K. Yadavalli, "Large area micropatterning of cells on polydimethylsiloxane surfaces.," *Journal of biological engineering*, vol. 8, p. 24, Jan. 2014. (Cited on pages 95 and 101.)

[223] J. Mitchel and D. Hoffman-Kim, "Cellular scale anisotropic topography guides schwann cell motility," *PLoS ONE*, vol. 6, no. 9, 2011. (Cited on pages 96 and 97.)

[224] A. Mata, A. Fleischman, and S. Roy, "Characterization of polydimethylsiloxane (pdms) properties for biomedical micro/nanosystems.," *Biomedical microdevices*, vol. 7, no. 4, pp. 281–293, 2005. (Cited on page 96.)

[225] G. M. Whitesides and A. D. Stroock, "Flexible methods for microfluidics," *Physics Today*, vol. 54, pp. 42–48, 2001. (Cited on page 101.)

[226] V. Sunkara, D.-K. Park, H. Hwang, R. Chantiwas, S. a. Soper, and Y.-k. Cho, "Simple room temperature bonding of thermoplastics and poly(dimethylsiloxane)," *Lab on a Chip*, vol. 11, pp. 962–965, 2011. (Cited on page 106.)

[227] S. Meucci, O. Vittorio, F. Beltram, and M. Cecchini, "Tubeless biochip for tailoring cell co-cultures in closed microchambers," *Microelectronic Engineering*, vol. 124, pp. 8–12, July 2014. (Cited on page 114.)

[228] L. Trombi, L. Mattii, S. Pacini, D. D'Alessandro, B. Battolla, E. Orciuolo, G. Buda, R. Fazzi, S. Galimberti, and M. Petrini, "Human autologous plasma-derived clot as a biological scaffold for mesenchymal stem cells in treatment of orthopedic healing," *Journal of Orthopaedic Research*, vol. 26, no. 2, pp. 176–183, 2008. (Cited on page 117.)

[229] M. Lampugnani, M. Corada, P. Andriopoulou, S. Esser, W. Risau, and E. Dejana, "Cell confluence regulates tyrosine phosphorylation of adherens junction components in endothelial cells," *Journal of Cell Science*, vol. 110, no. 17, pp. 2065–2077, 1997. (Cited on page 118.)

INDEX

Symbols

D, *see* diffusion coefficient
Pé, *see* Péclet number
Re, *see* Reynolds number
A_{FA}, *see* focal adhesion area
Λ, *see* nanograting periodicity
δ, *see* directionality
η, *see* dynamic viscosity
α_n, *see* neurite alignment
p, *see* nano-modification probability
NM^-, *see* negative nano-modification
NM^+, *see* positive nano-modification
T_g, *see* glass transition temperature

A

acoustic impedance, 30
aspect ratio, 52
autograft, 96

B

blebbistatin, 80
boundaries guidance, 97

C

cellular valving, 38
chemotaxis assay, 2
contact guidance, 97
creeping flow, 8

D

Diffusion coefficient, 12
directionality, 72
dispersion (cytoskeletal), 60
dynamic viscosity, 8

E

electrospinning, 50
equation
    Navier-Stokes, 7
    Stokes, 8

F

Fick's laws of diffusion, 12
FLAT substrate, 58
focal adhesion, 47
    area, 80

G

glass transition temperature, 54

H

hydraulic resistance, 11

I

integrin, 47

L

laminar flow, 8
loading mode, 34

M

mechanotransduction, 3
microfluidics, 2

N

nano-modification probability, 72
nanograting, 51
    periodicity, 53
negative nano-modification, 71
neurite, 76
    alignment, 77
neurofilament, 101
nocodazole, 80

P

Péclet number, 12
paxillin, 49
perfusion mode, 34
phantom, 28
photoacustic imaging, 28
Poiseuille flow, 9
positive nano-modification, 71
propidium iodide, 58

R

resist, 54
Reynolds number, 8

S

Schwann cell, 96
shear-stress, 10

T

topographical sub-unit, 70

V

vinculin, 87